Studies on Property and Structure Modification of Inorganic Glasses with Femtosecond Laser

Xi Wang

2011

Content

General Introduction

The history of glass is as long as that of human civilization. According to records, Egyptians began to use glasses from at least 7000 B.C., and glass is still one of the most common materials used in our everyday environment. The advantages of glass include: transparent, isotropic, thermal resistant, chemical resistant, easy to manufacture, and so on. These advantages enable inorganic glasses to be widely used as optical and photonic materials.

Due to the emergence of the laser and the rapid development of the modern information society, transition element doped glass has become one of the most important laser materials. Also, the interaction of ultra-short laser pulses with glass has attracted a great deal of attention since a series of new phenomenon were produced, which could be applied to fabricate new types of photonic devices.

Because glass is in an amorphous solid state completely lacking in long range and periodic atomic structure, it is meta-stable from the point of view of thermodynamics. Under the exposure of an intensive electromagnetic field, various changes in glass structure and ions valence can be induced inside glass [1-5]. In our study, a femtosecond laser is used as a powerful tool for the micro-structuring inside glass. With a pulse width in the femtosecond (10^{-15}) scale, the energy of photons is compressed in ultra short time, and the strength of the electromagnetic field can become extremely high when the laser beam is focused with an optical lens (~10TW/cm^2). In such circumstances, femtosecond laser has two apparent features. The first is that the thermal effect is eliminated due to an ultra short time for light-matter interaction and energy deposit. The second is that a non-linear process including multi-photon absorption, tunneling ionization, and avalanche ionization is

induced by the high localization of laser photons in time and spatial domains. Therefore, a femtosecond laser can be used to realize 3D space-selective micro- and nano-structuring inside transparent materials with a non-resonant wavelength, which can hardly be achieved when using a CW laser.

In addition, in comparison with a longer pulsed laser (multiple picoseconds to nanoseconds), less energy is required for the femtosecond laser to reach the threshold for breakdown. Furthermore, the non-linear process is different when the material is illuminated by a long pulse [6].Even the total pulse energy is high, the peak intensity is still too low to meet the required value for multi-photon or tunneling ionization with a pico- or nano-second laser. The result is avalanche ionization, which is a main main process starting with a free electron that comes from impurities or other defects in the focal volume. This electron works as the seed, acquiring kinetic energy from the laser pulse through inverse Bremsstrahlung absorption until it ionizes another electron from the valence band, resulting in two excited electrons in the conduction band [7, 8]. These electrons can be in turn accelerated by the electric field, repeat the inverse Bremsstrahlung absorption, and ionize other electrons in the valance band, causing an avalanche effect. However, the problem of this process is that the number of seed electrons is subject to large fluctuations, and the reproducibility of optical processing with a long pulse laser is poorer than that of the femtosecond laser. Besides, the laser wavelength of a longer pulsed laser usually lies in the ultraviolet regions, so the space selectivity of micro structuring is also compromised since the surface of materials would interact with incoming light at that waveband. Finally, a longer pulse time would also cause a thermal effect, which could reduce the accuracy of laser processing [9].

The main process of light-matter interaction during femtosecond laser irradiation includes multi-photon and tunneling ionization. Both of these effects would achieve efficient space-selective modification and syntheses functional devices with glass. In past decades, the femtosecond laser has been widely explored for use with three-dimensional memory [10-12], multicolor images [13], optical waveguides [14, 15], couplers [16, 17] and photonic crystals [18]. Among this research, permanent change in a glass structure without surface damage often draw interest [19-24] and becomes the key to using and understanding femtosecond laser processing.

In this work, we used a femtosecond laser for the micro-structuring inside glass materials and investigated the dependence of property on a glass structure. The purpose and main results are listed as follows.

Chapter 1: The concept and mechanism of femtosecond laser processing is reviewed, and the development of a new type of structuring inside glass is also introduced. Some background on the Raman theory and Raman spectroscopy is also described since our main measurements of the change in glass structure depend on this method.

Chapter 2: It was commonly thought that solid condensed state matter could only be classified into either crystalline or amorphous. The latter has only short-range order and is considered as an isotropic system. In this chapter, we show that, from evidence of Raman spectroscopy, long-range order could be induced inside transparent glass material without crystallization by using femtosecond laser irradiation. In short, a new state of condensed matter was discovered. We analog this long-range-ordered glass phase with liquid crystals and find that its property is different from any matter we know. With both glass and crystal properties, this new

phase has never been expected from existing glass or rheology theory, leading to further consideration about the glass forming process, supercooled liquid behavior, and the exploit micro-structuring method with femtosecond laser irradiation.

Chapter 3: We used a high-repetition-rate near-infrared femtosecond laser to reduce Eu^{3+} into Eu^{2+} inside silicate glass. Although there were already reports on using a femtosecond laser to reduce Eu ions, the photo-reduction process of Eu depended highly on the glass host, so we could achieve only a reduction in fluoride or borate glass. To break through this limitation, we found that we can use a different photo-reduction mechanism that involves laser-induced crystallization for the reduction. In this work, we show that this kind of idea is potentially valuable for the application of Eu-doped glass.

Chapter 4: In this chapter, Bi-doped glass is introduced as a promising candidate for the next generation of materials for fiber amplifiers, and we studied the effects of a glass host and structure on the luminescence property of bismuth ions.

Reference

[1] J. Qiu, J. Shimizugawa, Y. Iwabuchi, K. Hirao, Appl. Phys. Lett. **71** (1997) 43.

[2] J. Qiu, Y. SHimizugawa, Y. Iwabuchi, K. Hirao, Appl. Phys. Lett. **71** (1997) 759.

[3] J. Qiu, K. Hirao, Solid State Comumun. **106** (1998) 795.

[4] N.Jiang, J. Qiu, J. Silcox, Appl. Phys. Lett. **77** (2000) 3956.

[5] N.Jiang, J. Qiu, A. Gaeta, J. Silcox, Appl. Phys. Lett. **80** (2002) 2005.

[6] D. Du, X. Liu, G. Korn, J. Squier, and G. mourou, Appl. Phys. Lett. **64** (1994) 3071.

[7] D. Arnold, E. Cartier, Phys. Rev. B **46** (1992) 15102.

[8] A. Kaiser, B.Rethfeld, M. Vicanek, G. Simon, Phys. Rev. B **61** (2000) 11437.

[9]B. C. Stuart, M. D. Feit, S. Herman, A. M. Rubenchik, B. W. Shore, M. D. Perry, Phys. Rev. Lett. **74** (1995) 2248.

[10] E. N. Glezer, M. Milosavljevic, L. Huang, R. J. Finlay, T. H. Her, J. P. Callan, and E. Mazur, Opt. Lett. **21** (1996) 2023.

[11] J. Qiu, K. Miura, and K. Hirao, Jpn. J. Appl. Phys. **37** (1998) 2263.

[12] K. Miura, J. Qiu, S. Fujiwara, S. Sakaguchi, and K. Hirao, Appl. Phys. Lett. **80** (2002) 2263.

[13] J. Qiu, C. Zhu, T. Nakaya, J. Si, and K. Hirao, Appl. Phys. Lett. **79** (2001) 3567.

[14] K. M. Davis, K.Miura, N. Sugimoto, and K. Hirao, Opt. Lett. **21** (1996) 1729.

[15] K. Miura, J. Qiu, H. Inouye, T. Mitsuyu, and K. Hirao, Appl. Phys. Lett. 71 (1997) 3329.

[16] D.Homoelle, S. Wielandy, A. G. Gaeta, N. F. Borrelli, and C. Smith, Opt. Lett. 24 (1999) 1311

[17] K. Minoshima, A. M. Kowalevicz, I. Hartl, E. P. Ippen, and J. G. Fujimoto, Opt.

Lett. **26** (2001) 1516.

[18] H. Sun, Y. Xu, S. Joudkazis, K.Sun, M. Watanabe, J. Nishii, S. Matsuom, and H. Misawa, Opt. Lett. **26** (2001) 325.

[19] Y. Shimotsuma, P. G. Kazansky, J. R. Qiu and K. Hirao, Phys. Rev. Lett. **91** (2003) 247405.

[20] S. Kanehira, J. H. Si, J. R. Qiu, K. Fujita and Hirao, Nano Lett. **5,** (2005) 1591.

[21] M. Shimizu, K. Miura, M. Sakakura, M. Nishi, Y. Shimotsuma, S. Kanehira, T. Nakaya and K. Hirao, Appl. Phys. A **100** (2010) 1001.

[22] Y. Liu, M. Shimizu, X. Wang, B. Zhu, M. Sakakura, Y. Shimotsuma, J. R. Qiu, K. Miura and K. Hirao, Chem. Phys. Lett. **477** (2009) 122.

[23] M. Sakakura, M. Shimizu, Y. Shimotsuma, K. Miura and K. Hirao, Appl. Phys. Lett. **93** (2008) 231112.

[24] Y. Liu, B. Zhu, L. Wang, J. Qiu, Y. Dai, H. Ma, Appl. Phys. Lett. **92** (2008) 121113.

Chapter 1

3D Micro-Structuring of Glass with Femtosecond Laser

1.1 Fundamentals of Femtosecond Laser Processing

It is difficult to produce an interaction effect between glass and light by a one-photon process when the wavelength of excitation light differs from the resonant absorption band of the glass. However, femtosecond laser is one type of the pulse lasers whose pulse width is of order of femtoseconds. The ultra short duration of the laser pulse (1femtosecond=10^{-15} second) could have the energy of laser compressed so that the instantaneous intensity of the electromagnetic field of laser beam could reach extreme high. So femtosecond laser may induce different microstructures inside glass with non-linear effect. The optical setup of femtosecond laser used in our experiment is shown in Fig. 1.1.

Usually, an optical microscope system is used to focus the laser pulse inside various types of glasses and to observe the condition of the sample before and after laser irradiation. The microscope objective lens to focus the laser beam could be adjusted with changing the magnification or numerical apertures. A beam expander is set in the optical path of laser so that the diameter of the beam could be controlled and ensure the reproducibility of experiments.

A series of novel structuring inside glass could be induced with femtosecond laser. For example, color line due to the formation of color center and valence state change of active ions such as rare-earth and transition metal ions, refractive index changed spot due to local densification and defect formation, micro-void due to re-melting and shocking wave, micro-crack due to destructive breakdown, etc [1]. It is

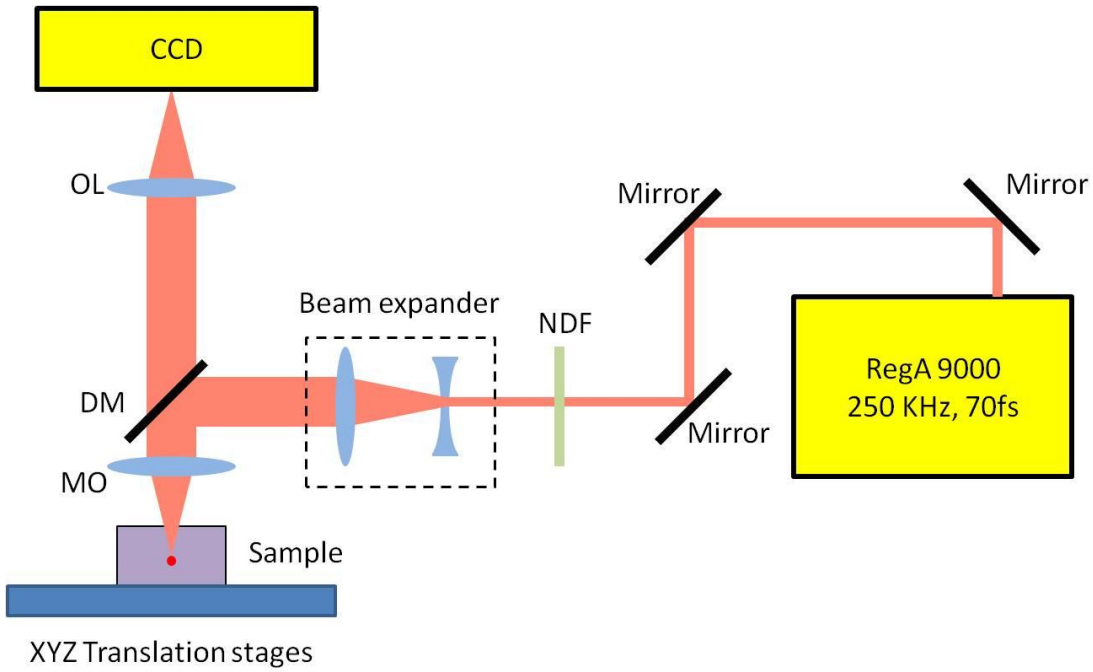

Fig.1.1 Schematic of the femtosecond laser setup. Beam expander is composed of a convex lens and a concave lens. NDF: neutral density filter; MO: microscope objective; DM: dichroic mirror. OL: optical lens.

commonly known that the most of the inorganic glasses have no intrinsic absorption at 800 nm which is the wavelength of femtosecond laser, so the linear absorption could not explain those effects. In order to understand the physical mechanism underlying the femtosecond processing inside inorganic glasses, it is inevitable to first briefly analyze the absorption processes during intense laser pulse pass through transparent dielectric materials.

Even though the energy gap E_g of transparent materials is much greater than the photon energy, absorption of light could take place at high intensity through nonlinear phenomena, such as multi-photon tunneling and avalanche ionization [2], Fig. 1.2 (a) illustrates the modification glass with a focused femtosond laser. Multi-photon ionization is based on simultaneous absorption of multiple photons for a single electron. Once the number of photons *m* fulfills the condition that $mhv>E_g$, electron transition from valence to conduction band is realized (see fig. 1.2 b). It is a highly intensity-dependent process, with the rate $P(I)=\sigma_m I^m$, where the σ_m is the multiphoton absorption coefficient for m-photon absorption.

The tunneling ionization is also induced when femtosecond laser interacts with materials. In a highly intense electric field, the coulomb potential energy barrier is distorted dramatically, which lowers the energy barrier and reduce the length of barrier. In such circumstance, electron is able to tunnel from the valence to conduction band, as is shown in Fig. 1.2 c.

Both multi-photon absorption and tunneling ionization could occur and compete with each other during femtosecond laser irradiation [3]. the competition could be evaluated by Keldysh parameter shown in the following:

$$\gamma = \omega(2m * E_g)^{1/2}/e\mathcal{E} \quad (1.1)$$

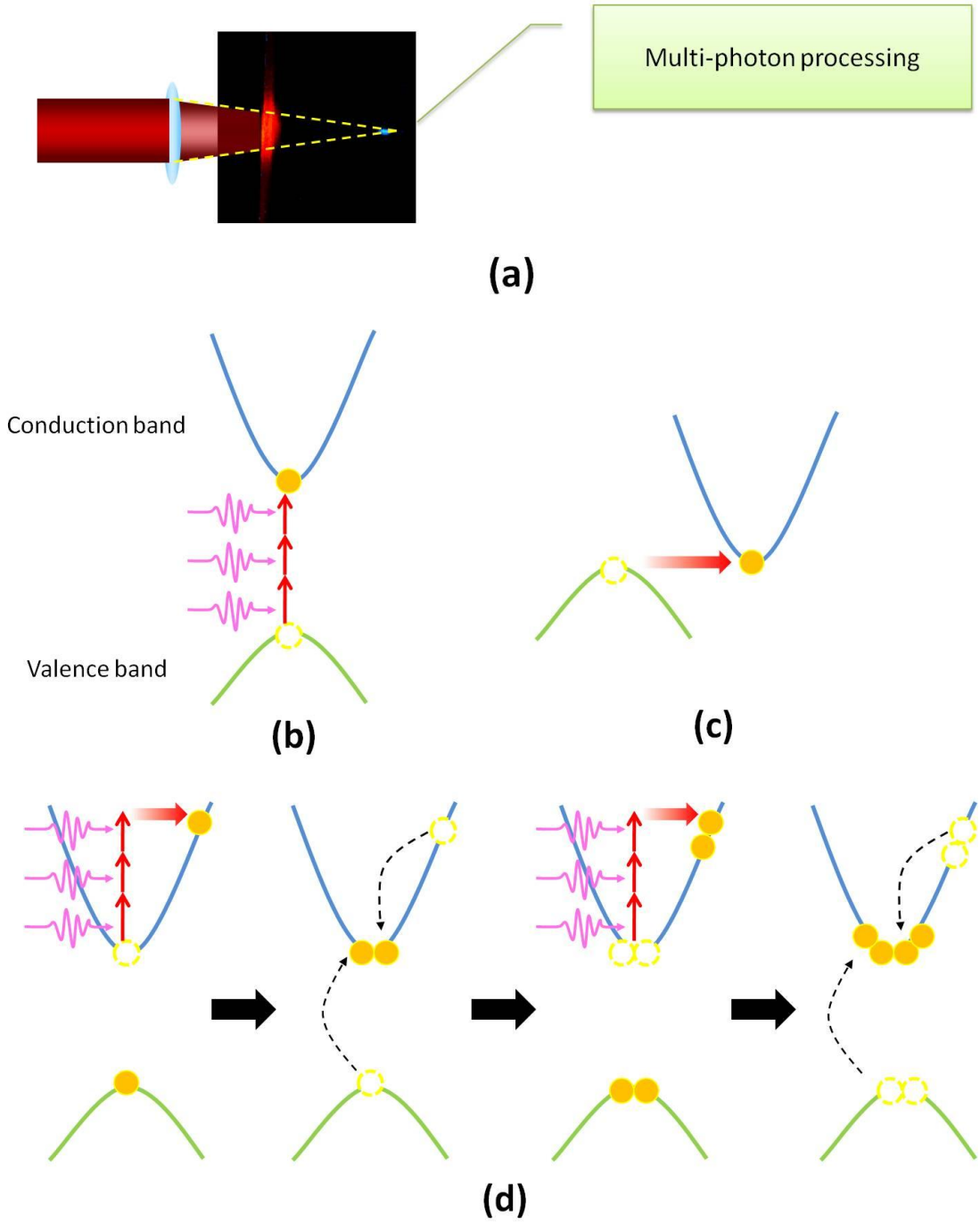

Fig. 1.2 Schematics of the non-linear optical processes induced by femtoscond laser. (a) demonstration of femtosecond laser processing with a objective lens inside transparent materials, (b) the multi-photon absorption, (c) tuneling ionization and (c) avalanche ionization

where the m and the e are the effective mass and charge of the electron and ε is the amplitude of the electric field oscillating at the frequency of ω. If γ is much smaller than 1.5, tunneling ionization dominates the process; on the other hand, multi-photon process will dominate when Keldysh parameter is much greater than 1.5. Compare with high frequency femtosecond laser (250 KHz, for instance), the low repetition rate (1 KHz) laser would acquire a much higher electric field (250 times stronger). So tunneling ionization process is the main process when use low frequency laser. Usually we adjust laser power so that γ~1 so that non-linear ionization is combination of both process when using high-repetition rate femtosecond laser.

After the laser intensity exceeds the threshold, some free electrons will be generated at the focal volume by the multi-photon or tunneling ionization process. These electrons act as seed for the avalanche ionization process [4]. The avalanche ionization process is demonstrated in Fig. 1.2 d. At the first, a free electron is at the bottom of the conduction band, when it is exposed to an intense laser light, it is accelerated and acquires kinetic energy, moving to a higher energy state in the conduction band. This process is called inverse Bremsstrahlung absorption. After the sequential absorption of photons, the total energy of the free electron exceeds the conduction band minimum by more than the band gap energy and it could ionize another electron from the valence band via direct collision, known as impact ionization. As the result, there are two free electrons in the conduction band. These electrons can be in turn absorb the photon energy and repeat the impact ionization to achieve an exponential growth of the free electron.

The avalanche ionization process increases the concentration of free electrons inside the dielectric materials and consequently dense plasma is formed at the focal

spot of femtosecond laser. The frequency of plasma approaches the vibration rate of electric field of light, at which point the materials becomes highly absorptive. Such process facilitates the transfer of energy of femtosecond laser to the glass. Rayner et al. [5] reported that at intensity of $8\times10^{14}W/cm^2$ near 90% of the energy of a 50-fs 800 nm laser pulse is absorbed by a pyrex substrate. Due to the nonlinear interaction between laser and glass, many phenomena could occur during femtoscond laser irradiation.

If the glass material is illuminated by a long pulse, the peak intensity is too low to allow multi-photon or tunneling ionization, even if the total pulse energy is very high. The initial seed of free electron for the avalanche process can only come from the impurities or dislocations within the focal volume. So the absorption process is erratic and poorly reproducible because the seed electron is subjected to randomness of local defects.

In addition, with short excitation pulses, the free electron plasma is formed on a time scale much shorter than that necessary for energy transfer to the lattice (Fig. 1.3). It is natural to conclude that only the high intensity femtoscond laser pulse could realize controllable and reproducible energy deposition in a small volume inside the bulk of a transparent material.

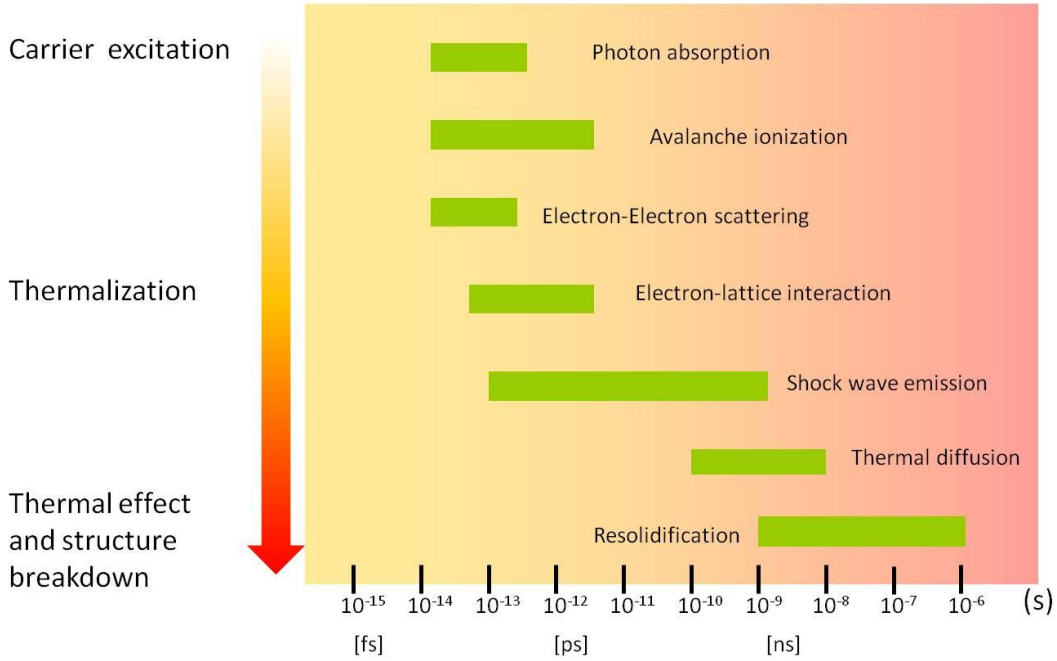

Fig. 1.3 Time scale of the physical phenomena related to the interaction between femtosecond laser and dielectric materials

1.2 Micro-Structural Changes Induced by Femtosecond Laser inside Glass

1.2.1 Valence State Manipulation of Active Ions

Materials with 3-dimensionally modulated microstructures have potential applications in optical field. Up to now, there have been a lot of investigations on the 3-dimensional micro-fabrication. Braun and Wizius have successfully fabricated 3-dimensional structures of semiconductors by template-directed electrochemical deposition [6]. Cumpston et al. have succeeded in the fabrication of micro-optical elements with two-photon photo-polymerization [7]. Holographic lithography has been used to fabricate 3-dimensional photonic crystals, which have periodical dielectric structures and can manipulate light in much the same way that a superconductor manipulates electrons [8]. Space-selective valence state change of active ions could be realized with femtosecond laser irradiation and has potential application in three-dimensional optical memory with ultrahigh storage density.

In 2001, Qiu [9] demonstrated that persistent photo oxidation of Mn^{2+} to Mn^{3+} in a silicate glass by a focused infrared femtosecond laser at room temperature. The mechanism is elucidated as the following: after the free electrons was generated by the electric field of femtosecond laser at the focal volume, Mn^{2+} was suggested to act as hole trapping centers and was oxidized to Mn^{3+} while Fe^{3+}, as well as active sites in glass matrix, acts as an electron trapping center. The similar mechanism could also be applied to rare-earth ions doped glass [10, 11] and realize controlling the valence state of active ions. Optical memory using a valence-state change of ions in a spot may allow one to read data with the generation of luminescence, thus providing the

advantage of a high signal-to-noise ratio, therefore, this technique will be useful in the fabrication of three dimensional optical memory devices with high storage density.

1.2.2 Precipitation of Nanoparticles

Nanoparticles have a wide range of electrical and optical properties due to the quantum size effect, surface effect and conjoint effect of the nanostructures. Materials doped with nanoparticles exhibit large third-order nonlinear susceptibility and ultrafast nonlinear response. They are expecte to be promising materials for ultrafast all-optical switched in the THz region. For the applications in integrated optoelectronics, a well-defined assembly and spatial distribution of nanoparticles in materials are essential. Many studies have been carried out on fabrications of nanoparticale-doped matierials, but there are no effective methods to control the spatial distribution of nanoparticles in materials.

Space-selective precipitation and controlling of silver and gold nanoparticles in glass could be realized by using femtosecond laser irradiation [12-14]. An electron was driven out from the 2p orbital of a nonbridging atom near the Ag^+ or Au^+ ions after femtosecond laser irradiation, while Ag^+ or Au^+ captured the electron to form Ag or Au atoms. Then these photo-reduced Ag or Au atoms aggregated to form nanoparticles during the heat treatment.

Other types of nanoparticles could also be controled inside glass with the irradiation of femtosecond laser. It is recently reported that Si nanocrystals are space-selectively deposited in silicate glass via a thermite reaction triggered by femtosecond laser pulses [15]. Glass whose starting material contains metallic Al has O-deficient centers (≡Si–Si≡) and Al-rich structures in which O ions are not

sufficiently filled. The local structural change from SiO_2, including O-deficiency centers, to Si rich structures (≡Si–Si–Si≡, Si cluster), due to the breaking of Si–O bonds and the oxidation of Al, i.e., the thermite reaction, is caused by femtosecond laser irradiation. A network modifier such as Ca ions can simultaneously be diffused around the focal spot by thermal diffusion. Furthermore, interstitial oxygen (atoms or molecules) in the focal spot during the femtosecond laser irradiation may be consumed in the thermite reaction with aluminum and then diffuse around the focal spot. During these process Si-rich structures such as Si clusters are transformed into larger Si nanoparticles by laser irradiation. Silicon as a photonic medium offers unique advantages in the fabrication of photonic integrated circuits. It is transparent in the range of optical telecommunications wavelengths (1.3 and 1.55 μm) and has a high index of refraction, which enables the fabrication of high-index-contrast sub-micrometer structures in photonic crystal devices.

1.2.3 Precipitation of Functional Crystals

When we irradiate the interior of the glass with ultrafast laser, the energy of laser pulse is accumulated at the minute area for a very short time, resulting in a dramatic rise in the temperature and internal pressure in the region of focus. In taking advantage of this phenomenon, we could form spherical melting regions at arbitrary sites within a bulk glass by using a femtosecond laser with high repetition rate. The second-harmonic-generation β-BaB2O4 (BBO) crystal growing inside glass with single-crystal-like structure is induced using non-resonant femtosecond laser [16]. The growth of BBO crystal is expected to be applied to waveguide-type frequency conversion devices, especially in the ultraviolet region. Other types of functional

crystal could also be precipitated with the irradiation of femtosecond laser, depending on the composition of glass host [17, 18].

1.2.3 Formation of Polarization-Dependent Nanograting

Polarization-dependent nanograting was observed inside commercially available synthetic silica glass which was irradiated with femtosecond laser [19]. The permanent polarization-dependent microstructure in glass is responsible for the memorized polarization-dependent light scattering [20, 21]. After laser irradiation, a micro spot with diameter of about 2 μm is formed at the focal point. Then a periodic structure of stripe-like dark regions with low density of material and of ~ 20 nm width which are aligned perpendicular to the writing laser polarization direction was found in the laser-modified region. Also it is reported that the grating period distance is decreased as the exposure time increases.

Once a high free electron density is produced by multi-photon and alalanche ionization, the glass material has the properties of plasma and will absorb the laser energy via one-photon absorption mechanism of inverse Bremsstrahlung (Joule) heating. The light absorption in the electron plasma will excite bulk electron plasma density waves. These are longitudinal waves with the electric field component parallel to the direction of propagation. Such electron plasma wave could couple with the incident light wave only if it propagates in the plane of light polarization. Initial coupling is produced by inhomogeneities induced by electrons moving in the plane of light polarization. The coupling is increased by a periodic structure created via a pattern of interference between the incident light field and the electric field of the bulk electron plasma wave, resulting in the periodic structures modulation of the electron

plasma concentration and the structural changes in glass.

1.2.4 Element Migration and Network Modification

Femtosecond laser irradiation at a high repetition rate tends to produce not only shock waves but also causes a heat accumulation effect around the focal point [22]. If heat transfer, also known as thermomigration, occurs inside the glass due to laser irradiation, the constituent elements of the glass will either disperse or agglomerate in a specific area because of the formation of a thermal gradient in a small area, known as Soret effect. In 2008, Kanehira et al. [23] demonstrated the ion exchange effect in glass after femtosecond laser irradiation. The observed ion exchange involved two groups of ions, namely, network formers and network modifiers. The single-bond strength of the network former is much higher than that of the net work modifier, therefore, the bonds of the network modifier will be easily broken when femtosecond laser irradiates and melts the region of focal spot. Each ion will diffuse under the temperature gradient and forms ring-shaped pattern of composition variation [24].

Liu et al. reported femtosecond laser pulses can change coordination of B in the sodium borate glasses with the ion migration effect [25]. During femtosecond laser irradiation, sodium ions are weakly bonded and have low activation enthalpy, so Na would easily diffuse to the lower temperature part of the laser modified zone several micrometers away from the center, resulting in the redistribution of elements. The concentrations of sodium ions and interstitial oxygen ions become minima at the focal point due to strong diffusion effect. They increase with the distance from the center and reach maxima at a certain location. The concentration of sodium ions and interstitial oxygen ions then decreases again with further increasing distance from the

center and reaches the value of unirradiated glass. The formation of BO_4 is accompanied by composition change at the focal region. Thus, the coordination of boron ions changes from three-fold to four-fold up to some distance from the laser focus point inside the laser modified zone. Temperature field plays the main role in the coordination state change of boron and element migration since pressure has little effect on diffusion coefficient than temperature. The ion migration and glass network modification is very promising in fabricate waveguide for integrated optics.

1.3 Fundametals on Confocal Raman Spectroscopy

1.3.1 Raman Scattering

If the substance being studied (as a gas, liquid, or solid) is strongly illuminated by monochromatic light and the scattered light is observed through a spectrometer, a spectra could be obtained which consists of a strong line of the same frequency as the incident illumination together with weaker lines on either side shifted from the strong line by frequencies ranging from a few to about 3500 wave numbers (cm^{-1}). The pattern of lines is symmetrical about the exciting line except with regard to intensities. The lines of frequency less than the exciting line are called Stokes lines, and the other is anti-Stokes lines. These lines differing in frequency from the exciting line are Raman lines originate from Raman scattering. Combining such lines we can get Raman spectra.

Classical picture of interaction between an oscillating electromagnetic field and a molecular system is used to demonstrate mechanism of Raman scattering (Fig. 1.4 a). The incident electric field will disturb the electronic charge distribution in the molecular and thereby induce dipole moments even in the case of an unpolar molecular system. The sum of the induced dipole moments will act as a macroscopic polarization, which represents the source for a secondary electric field. The induced dipole could be represented as below:

$$\mu(t) = \alpha_0 E_0 \cos(\omega_0 t) + \frac{1}{2}\left(\frac{\partial \alpha}{\partial q}\right)_{q_0} q_0 E_0 \cos\left[(\omega_0 - \omega_q)t\right] + \frac{1}{2}\left(\frac{\partial \alpha}{\partial q}\right)_{q_0} q_0 E_0 \cos[(\omega_0 + \omega_q)t] \quad (1.2)$$

, where α is the polarizability, q_0 is the balance position of vibration displacement q, the molecular vibration has the frequency of ω_q, α_0 is polarizability at q_0, E_0

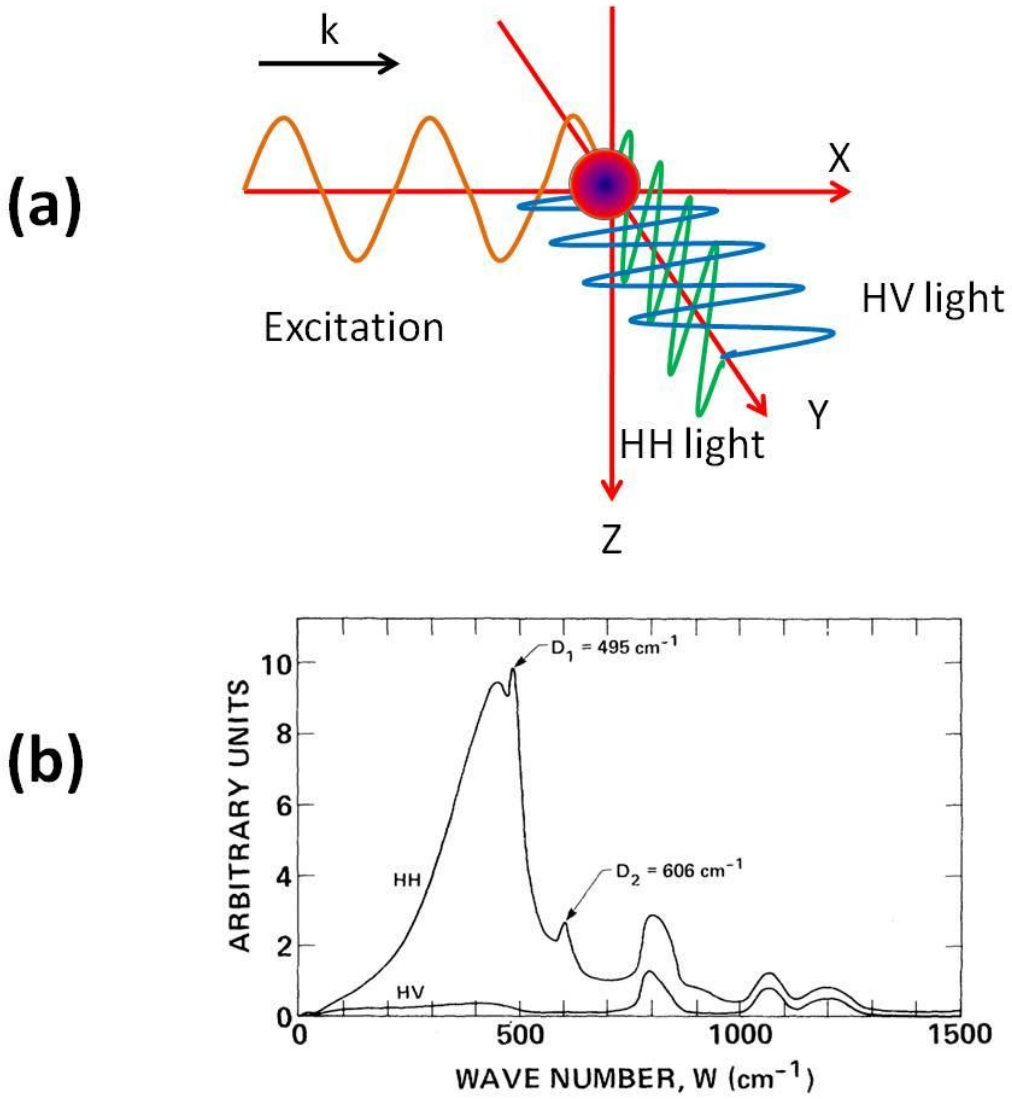

Fig 1.4 (a) Schematic representation of Raman scattering with a particle and (b) the polarized Raman spectra of silicate glass.

represents the strength of electric field oscillate at frequency of ω_0. The formula is composed of three terms and the first one represents the Rayleigh scattering and does not contain any information of the molecular vibration. However, the second term is the Storks line and contains information about the molecular system. Finally, the third term represents the anti-Storks scattering and contains the identical information with Stokes lines.

The intensity I, or time-averaged power per unit solid angle, radiated by an oscillating electric dipole induced in a molecule by the electric field of the incident radiation, along a direction making an angle θ with the axis of the dipole is given by

$$I = \frac{{\omega_s}^4}{32\pi^2\varepsilon_0 c^3}{\mu_0}^2 \sin^2\theta \tag{1.3}$$

, where ω_s is the frequency of dipole vibration and μ_0 is the amplitude of induce dipole. For the observation geometry shown in Fig. 1.4 a, θ is $\pi/2$. If we set the $\frac{1}{2}\left(\frac{\partial\alpha}{\partial q}\right)_{q_0} q_0$ as the Raman polarizability, α', we could have the expression for the Raman scattering:

$$I = \frac{(\omega_0-\omega_q)^4}{32\pi^2\varepsilon_0 c^3}(\alpha' E_0)^2 \tag{1.4}$$

, where E_0 is the electric field amplitude of incident light. In general, however, μ_0 must be replaced by the more complex expression:

$$\boldsymbol{\mu}_0 = \begin{bmatrix} \alpha'_{xx} & \alpha'_{xy} & \alpha'_{xz} \\ \alpha'_{yx} & \alpha'_{yy} & \alpha'_{yz} \\ \alpha'_{zx} & \alpha'_{zy} & \alpha'_{zz} \end{bmatrix} \mathbf{E}_0 \tag{1.5}$$

, where the subscript denotes the corresponding component on the Cartesian coordinates. The polarizability matrix could be diagonalized by choosing suitable coordination axes which is called principal axes and be simplified as:

$$\boldsymbol{\alpha}' = \begin{bmatrix} \alpha'_1 & 0 & 0 \\ 0 & \alpha'_2 & 0 \\ 0 & 0 & \alpha'_3 \end{bmatrix} \tag{1.6}$$

If the molecular at free oriented, the Raman signal expressed in Eq. 1.4 must be averaged over all orientations. Finally we can have the expression for the case presented in Fig. 1.4 a:

$$I_{HH} = \frac{(\omega_0-\omega_q)^4 I_0}{16\pi^2\varepsilon_0{}^2 c^4} N \frac{45\delta^2+4\gamma^2}{45} \quad (1.7)$$

$$I_{HV} = \frac{(\omega_0-\omega_q)^4 I_0}{16\pi^2\varepsilon_0{}^2 c^4} N \frac{\gamma^2}{15} \quad (1.8)$$

, where δ is spherical part of the polarizability, γ is the anisotropy [26]. They are defined by

$$\delta = \frac{1}{3}(\alpha'_1 + \alpha'_2 + \alpha'_3) \quad (1.9)$$

$$\gamma = \frac{1}{2}[(\alpha'_1 - \alpha'_2)^2 + (\alpha'_2 - \alpha'_3)^2 + (\alpha'_3 - \alpha'_1)^2] \quad (1.10)$$

Above expression indicate that IHH and IHV are deferent even for a isotropic system. In Fig. 1.4 b the polarized Raman spectra of silicate glass is shown and the depolarization is dependent on symmetric property of the molecular vibration. These results also suggest that Raman intensity could change if the orientation of the molecular in the system is no longer free-oriented due to the averaging result of polarizability changes. Such anisotropic averaging is highly useful for the determination of molecular orientation in liquid crystals [27-29].

1.3.1 Confocal Raman System

One of the ultimate goals of any analytical technique is to achieve the best possible differentiation. In terms of microscopy, this means the ability to distinguish between sample details and features of interest as clearly as possible, by somehow differentiating them from the ambient background. Microscopy has a rich history of finding and developing numerous dyes, fluorophores and labels to “stain” target sample features in order to differentiate them from the rest of the sample. However,

the arsenal of staining agents is limited and some properties and structures are difficult to study with conventional analytical techniques due to their inability to chemically differentiate materials with sufficient spatial resolution, without damage or preferential solvent washing. On the other hand, confocal micro-spectroscopy provides a novel approach to solve these problems.

Confocal imaging techniques are based on point-to-point image formation (Fig. 1.5). In confocal microscopy, the light source is focused with a lens or an objective onto a sample. The spatial extension of the focus spot is determined by the wavelength and the quality of the image formation. The image spot is then focused through a second lens onto the aperture (pinhole) in front of a detector. The size of the pinhole is chosen so that only the central part of the focus can pass through the pinhole and reach the detector. In such circumstance, only the signal from a single point on a sample is collected. Therefore, instead of obtaining trivial cumulative information about the spot signal intensity we can obtain a signal spectrum which can be transformed into detailed information of the given spot on a sample. In other words, a principally new dimension is added in the microscopy measurements, giving us an opportunity to differentiate the structures never detectable before.

The spectral information in confocal microscopy can be obtained through different techniques such as Absorption, Reflection, Transmission, Emission, Photoluminescence, Fluorescence or Raman spectroscopy.

Clear advantages of confocal Raman microscopy assured its wide-spread proliferation into multiple areas such as nanotechnology (molecular electronics, nanosensors, nanotubes and nanowires), material science (phase segregated systems) and catalysis (single site catalysts). In this thesis, we used the confocal Raman

spectroscopy to analyze the microscopic glass structure modifications induced by femtosecond laser.

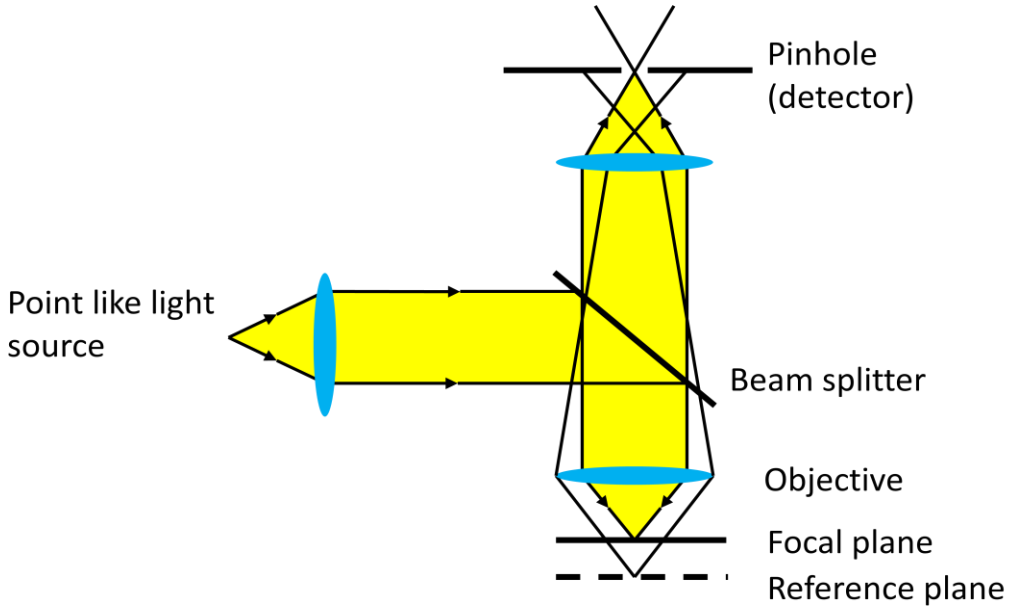

Fig. 1.5 Principal setup of a confocal microscope

1.4 Glass Densification with Femtosecond Laser Irradiation

1.4.1 Experimental

A glass with composition of $15Na_2O–85GeO_2$ (mol%) was prepared for the present study. Reagent grade of Na_2CO_3, and GeO_2 were used as raw materials. A 20g mixing batch was ground finely and melted in a Pt crucible at 1450 ℃ for 1 h in air. The melt was then cast onto a steel plate and quenched quickly with another plate. The sample was cut into 10 mm×10 mm×3 mm dimensions and polished for optical measurements.

A regenerative amplified 800 nm Ti:sapphire laser (RegA 9000, Coherent Inc.) with 80 fs, 250 kHz mode locked pulses was employed as the laser source in the experiment. The laser beam was focused inside the glass sample placed on an XYZ stage via a 40× objective lens (NA = 0.55). The confocal Raman spectra were measured by a Raman spectrometer (Tokyo Instruments, NanoFinder 30) with a 532 nm laser as the excitation source. The glass transition temperature of the sample was determined with differential thermal analysis (Rigaku, Thermal plus DSC 8270) at a heating rate of 10 K/min.

1.4.2 Result and Discussion

Modified structures were induced in the glass by static laser exposure of varied pulse energy (from 1 μJ to 2.2 μJ) with a constant irradiation time of 30 s and a focal depth of 80 μm beneath the surface of the glass. Fig. 1.6 presents the microscopic images of the laser-modified structure inside the glass. The outer structure could result from high temperature elevation [30]. The dark inner structure is due to

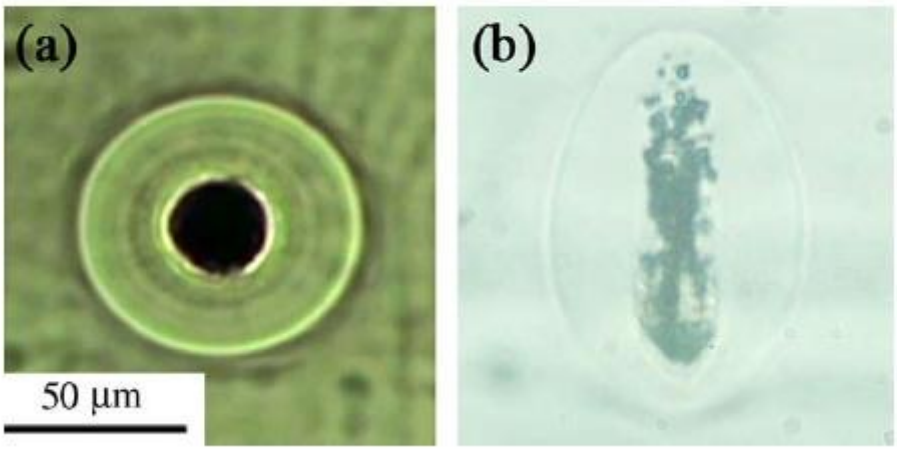

Fig. 1.6 (a) Top view and (b) side view microscope images of the laser-modified structrure (laser power: 350 mW, irradiation time: 30s).

discontinuous scattering centers. The scattering centers may stem from laser induced composition and density variation such as bubble formation in the photoexcited region.

Confocal Raman imaging revealed that Raman band intensities increased by 15% in a ring-shaped region in the modified region compared with unirradiated glass, as is shown in Fig.1.7. The band peak at 538cm^{-1} is assigned to symmetric stretching of Ge-O-Ge bonds associated with three-membered ring formation of GeO_4 tetrahedra, and two high frequency bands at 821cm^{-1} and 912cm^{-1} can be assigned to transverse optic/longitudinal optic (TO/LO) splitting of the antisymmetric stretching of Ge-O-Ge bonds within the network [31]. In correspondence with the intensity increase in the ring-shaped region, the peak location of the 538 cm^{-1} and 821 cm^{-1} band were blue-shifted by 7 cm^{-1} and 20 cm^{-1} respectively, while that of the 912 cm^{-1} band were red-shifted by 11 cm^{-1}. In the focal region where is the center of the modified region, the Raman intensity decreased to less than 40% of the value of the unmodified glass. This can mainly be attributed to the formation of a less dense core and scattering centers near the focal region, which is consistent with other studies of high repetition rate femtosecond laser induced damage in other glasses [32]. The tendency of frequency shift of the three peaks near the center of focus is opposite to that in the outer region. With the microscopic image of the modified structure, it is confirmed that the outer skirt of the ring-shaped contrast due to enhanced Raman scattering almost coincides with the outer structure of the modified region.

The Raman spectra are presented in Fig. 1.8, showing Raman intensity changes and frequency shifts in the modified region in regards to unmodified glass. No obvious presence of Raman scattering band near 240 cm^{-1} associated with [GeO_6]

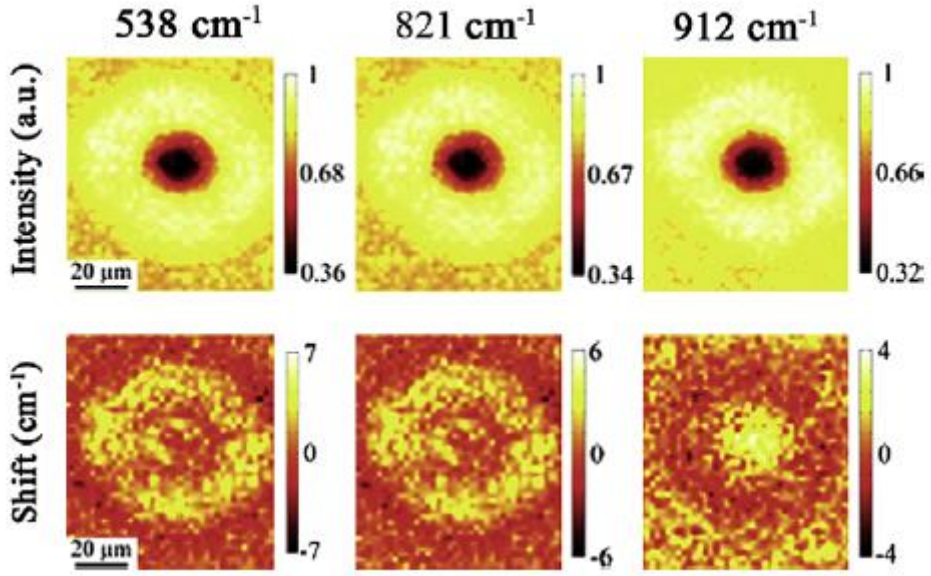

Fig. 1.7 Spatial map of the peak intensity and frequency shift of the 538cm^{-1}, 821cm^{-1}, 912cm^{-1} Raman band in regard to the bulk germinate glass over the laser-modified region(laser pulse energy: 350 μJ, irradiation time: 30s). The peak shift is automatically calculated with the software of the nanofinder.

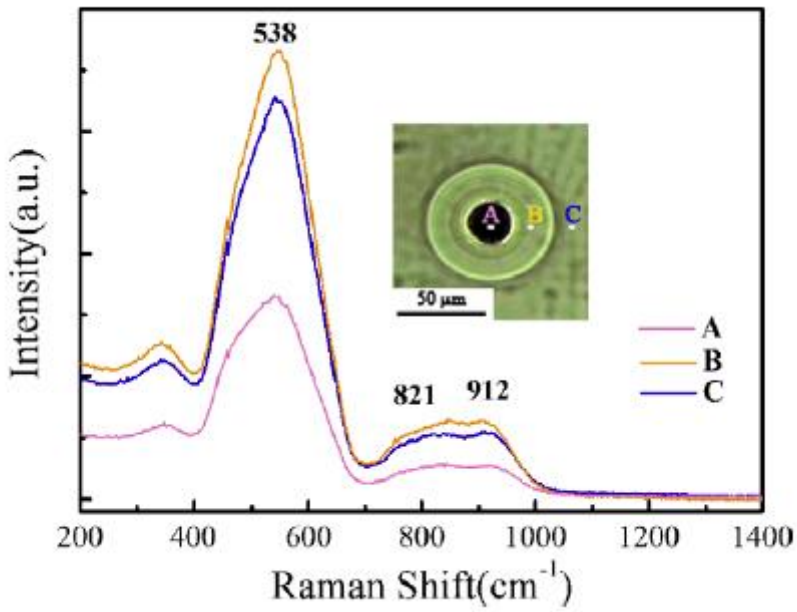

Fig. 1.8 Confocal Raman spectra from the laser focal volume (A), the region with enhanced Raman scattering (B) and unmodified region (C) in the glass.

octahedral vibrations was detected in the spectra either from the unmodified glass or from the modified area. Hence, it can be concluded that only a small amount of [GeO_6] octahedra was present in the network of as-made glass and the plausible four-fold to six-fold coordination change of Ge ions has not been induced in the modified region.

With the 250 kHz femtosecond laser irradiation, heat accumulation occurred near the focal volume and heat diffusion led to an increase of the local temperature up to more than 1000 ℃ in the outer zone surrounding the photo-excited region, which may have a diameter of tens of micrometers around the focal volume [33]. The pressure increase corresponding to the temperature elevation can be calculated by,

$$P = Y\beta\Delta T/3(1-2\sigma) \quad (1.11)$$

, where Y is the Young's modulus, β is the Poisson's ratio, and σ is the thermal expansion coefficient. For the germanate glass, Y = 65 GPa, $\beta = 7.6 \times 10^{-6}$ K^{-1}, and σ= 0.3. Taking the temperature increase ΔT as 1000 K for a rough estimation, a pressure increase of ~400 MPa will be generated in the outer heat-affected zone, which corresponds to the region with enhanced Raman scattering shown in Fig. 1.7. Nevertheless, the pressure remains too low to induce fourfold- to sixfold-coordination change of Ge ion, which can only occur in higher pressure range (above 6 GPa for GeO_2 glass). Near the focal volume, glass melts due to high temperature up to 2000 ℃ produced by heat accumulation. Dramatic thermal expansion of the melts occurred with propagation of pressure waves out of the focal volume, producing a less dense region near the focal volume and a stress on the surrounding glass. As soon as the irradiation was stopped, the glass was rapidly depressurized by ultrafast cooling.

However, the decompression happened so quickly that made it hard for structural relaxation of the glass. Still a considerable amount of compressive stress and strain resulting from the thermal expansion in the previously heated region would remain in

the modified structure. Near the focal volume a less dense core was formed in spite of some recovery of density after the irradiation was stopped.

Fig. 1.9 b shows the transmission image of the laser-modified structure in glass between two crossed polarizers. It is known that birefringence refractive index changes can be induced in the photo-excitation region by femtosecond laser irradiation, because of nanometer-scale structuring of material [19, 34]. While the birefringence pattern around the outer structure of the modified region in this work which is mainly heat-affected, is formed in association with residual stress distribution.

To clarify the mechanism of the enhancement of Raman scattering in the modified region, we annealed the glass sample at 520 ℃ for 1 h, which is near the T_g (535 ℃) of the glass for further investigation. Fig. 1.9 (d) shows the OM transmission image of the laser induced modified structure after heat treatment. The birefringence pattern disappeared because of relaxation of the residual stress due to structural relaxation during heat treatment. Interestingly, it is seen in Fig. 1.9 (c) that the outer structure of the modification disappeared, inferring that the outer structure of the modified region was produced by strains resulting from thermal expansion. Fig. 1.10 shows the intensity maps and frequency shifts of the bands over the laser-modified region after the heat treatment. It is found that the contrast due to enhanced Raman scattering or frequency shifts faded away.

The residual stress is believed to play an important role to lead to the enhancement of Raman intensity, which could be justified by the previous Raman spectroscopic study on pressure induced structural change of the glass [35, 36]. For GeO_2 glass, the origin of the 520 cm^{-1}, 857 cm^{-1}, and 973 cm^{-1} band is the same as

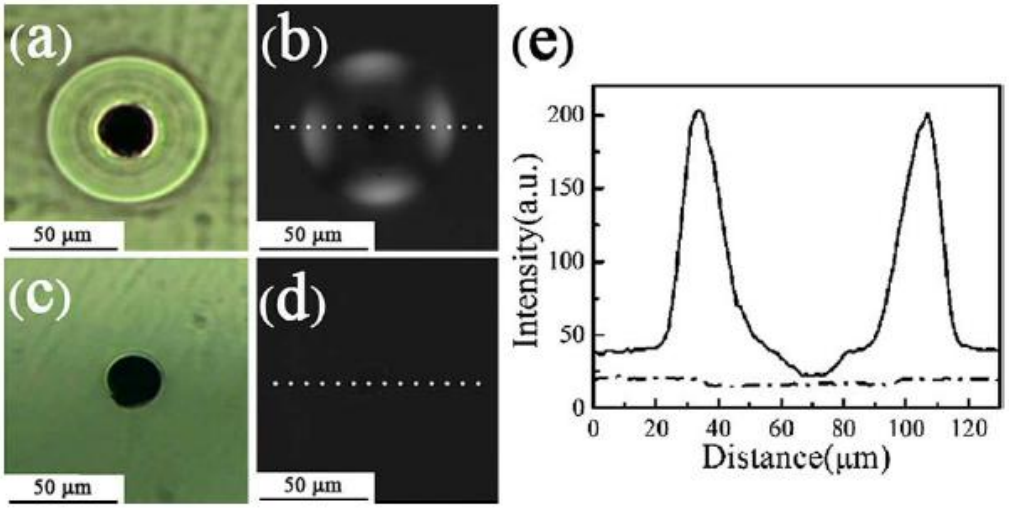

Fig. 1.9 Optical transmission image of the modification in the glass illuminated by natural light, and cross-polarized light, before((a) and (b)) and after heat treatment at 520 ℃ for 1h ((c) and (d)). (e) The transmitted light intensity along the white dotted line shown in (b) (solid curve) and (d) (dash and dot curve)

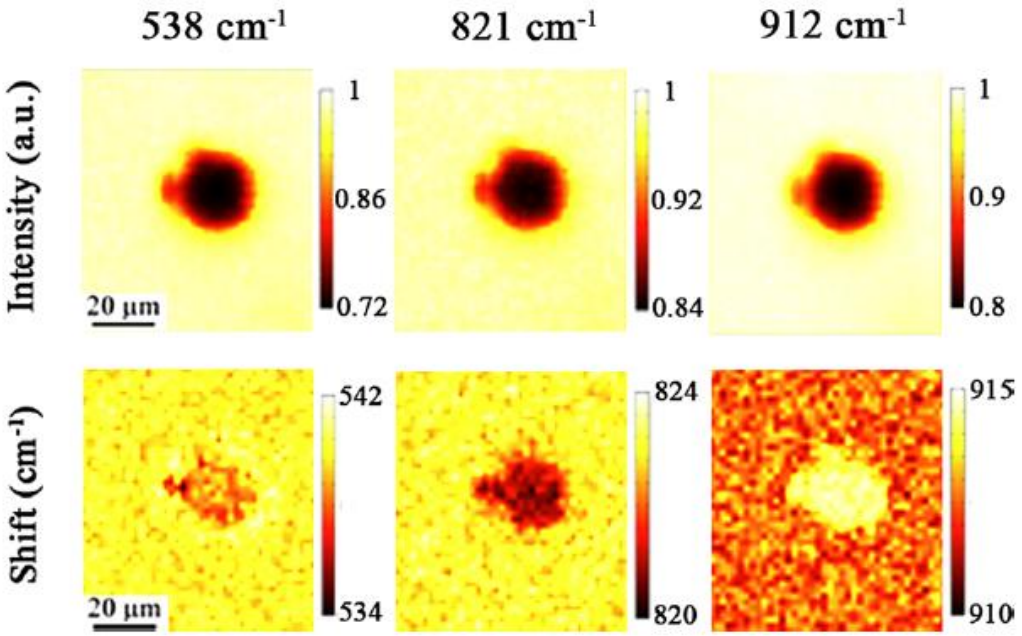

Fig. 1.10 Spatial map of the peak intensity and frequency shift of the 538cm^{-1}, 821cm^{-1}, 912cm^{-1} Raman band in regard to the bulk germinate glass over the modified region after heat treatment (520 ℃, 1h).

that of the 538 cm^{-1}, 821 cm^{-1}, and 912 cm^{-1} band in the sodium germanate glass used for our study. As GeO_2 glass is compressed up, to below 5.6 GPa, the intensity of those three bands increase by several times, and the 857 cm^{-1} and 973 cm^{-1} bands coalesces, an observation which are consistent with the results of the modification reported by confocal Raman imaging.

We present the mechanism of the enhanced Raman scattering in the laser induced modified region as follows. When the glass network in the modification is subjected to stress, tetrahedral distortion increases accompanied by a small decrease of the inter-tetrahedral Ge–O–Ge bond angle. Since this decrease further constrains the magnitude and distribution of the inter-tetrahedral angles, medium range order of the network increases, leading to a population buildup of the three-membered rings. The blue shift of the 538 cm^{-1} band reflects the strain within the network. After heat treatment, the network strain decreased, as demonstrated by the decrease of the band intensity as well as a red shift of the 538 cm^{-1} band to normal value of the glass. The formation of the less dense core of the modified structure could be another factor contributing to the densification of outer structure, because of drastic expansion of the melted material outside the focal region into surrounding material. The slight red shift of the 821 cm^{-1} band as well as the blue shift of the 912 cm^{-1} near the focal volume in the modified region may be caused by the tensile stress due to the formation of the less dense structure. After the heat treatment the contrast due to relatively low intensity still exists near the focal volume in spite of some recovery of intensity (70% of the value of unmodified glass) due to thermal driven bleach of defects, suggesting some damage with good heat stability was induced in the focal volume.

1.5 Conclusion

In this chapter, we demonstrated the advantages of femtosecond laser processing inside glass with various applications. Specifically, we used the confocal Raman system to provide the evidence of glass densification inside a binary sodium germanate glass induced by 250 kHz femtosecond laser irradiation. The femtosecond laser is very promising in fabricating photonic devices and the confocal Raman spectroscopy provides us a convenient method to analyze the structure change in a microscopic scale.

.

1.5 References

[1] J. Qiu, J. Ceram. Soc. Jpn **109** (2001) S25.

[2] R. Osellame, H. Hoekstra, G. Cerullo, and M. Pollnau, Laser Photonics Rev. 5 (2011) 442.

[3] A. P. Jglekar, H. Liu, E. Meyhofer, and G. Mourou, A. J. Hunt, Proc. Natl. Acad. Sci. USA 101 (2004) 5856

[4] B. C. Stuart, M. D. Feit, S. Herman, A. M. Rubenchik, B. W. Shore, M. D. Perry, Phys. Rev. Lett. **74** (1995) 2248.

[5] D. Rayner, A. naumov, and P. Corkum, Opt. Express **13** (2005) 3208.

[6] P. V. Braun, P. Wiltzius, Nature **402** (1999) 603.

[7] B. H. Cumpston, S. P. Ananthavel, S. Barlow, D. L. Dyer, J. E. Ehrlich, L. L. Erskine, A. A. Heikal, S. M. Kuebler, I.-Y. S. Lee, D. McCord-Maughon, J. Qin, H. Röckel, M. Rumi, X. Wu, S. R. Marder, and J. W. Perry, Nature **398** (2000) 51.

[8] M. Cambell, D. N. Sharp, M. T. Harrison, R. G. Denning, and A. J. Turberfield, Nature **404** (2000) 53.

[9] J. Qiu, C. Zhu, T. Nakaya, J. Si, K. Kojima, F. Ogura, and K. Hirao, **79** (2001) 3567.

[10] J. Qiu, K. Kojima, K. Miura, T. Mitsuyu, and K. Hirao, Opt. Lett. **24** (1999) 786.

[11] K. Miura, J. Qiu, S. Fujiwara, S. Sakaguchi, and K. Hirao, Appl. Phys. Lett. **80** (2002) 2263

[12] J.Qiu, M. Shirai, T. Nakaya, J. Si, X. Jiang, C. Zhu, and K. Hirao, Appl. Phys. Lett. **81** (2002) 3040.

[13] J. Qiu, X. Jiang, C. Zhu, H. Inouye, J. Si, and K. Hirao, Opt. Lett. **29** (2004) 370.

[14] J. Qiu, X. Jiang, C. Zhu, M. Shirai, J. Si, N. Jiang, and K. Hirao, Angew. Chem.

Int. Edn. **43** (2004) 2230.

[15] K. Miura, K. Hirao, S. Shimotsuma, M. Sakakura, and S. Kanehira, Appl. Phys. A **93** (2008) 183.

[16] K. Miura, J. Qiu, T. Mitsuyu, and K. Hirao, Opt. Lett. **25** (2000) 408.

[17] A. Stone, M. Sakakura, Y. Shimotsuma, G. Stone, P. Gupta, K. Miura, K. Hirao, V. Dierolf, and H. Jain, J. Non-Cryst. Solids **356** (2010) 3059.

[18] B. Lu, Y. Dai, and H. Ma, J. Inorg. Mater. **24** (2009) 769.

[19] Y. Shimotsuma, P. G. Kazansky, J. R. Qiu and K. Hirao, Phys. Rev. Lett. **91** (2003) 247405.

[20] P. G. Kazansky, H. Inouye, T. Mitsuyu, K. Miura, J. Qiu, and K. Hirao, Phys. Rev. Lett. **82** (1999) 2199.

[21] J. Qiu, P. G. Kazansky, J. Si, K. Miura, T. Mitsuyu, K. Hirao and A. Gaeta, Appl. Phys. Lett. **77** (2000) 1940.

[22] R. R. Gattass L. R. Cerami, and E. Mazur, Opt. Express **14** (2006) 5279.

[23] S. Kanehira, K. Miura, and K. Hirao, Appl. Phys. Lett. **93** (2008) 023112.

[24] M. Shimizu, M. Sakakura, S. Kanehira, M. Nishi, Y. Shimotsuma, K. Hirao, and K. Miura, Opt. Lett. in press.

[25] Y. Liu, B. Zhu, L. Wang, J. Qiu, Y. Dai, and H. Ma, Appl. Phys. Lett. **92** (2008) 121113

[26] E. B. Wilson, Jr., J. C. Decius and P. C. Cross. Molecular vibrations. (1955).

[27] A. Sanchez-Castillo, M. A. Osipov and F. Giesselmann, Phys. Rev. E **81** (2010) 021707.

[28] R. Pérez, S. Banda and Z. Qunaies, J. Appl. Phys. **103** (2008) 074302.

[29] C. D. Southern and H. F. Gleeson, Eur. Phys. J. E **24** (2007) 119.

[30] K. Itoh, W. Watanabe, S. Nolte, and C.B. Schaffer, MRS Bull. **31** (2006) 620.

[31] G. S. Henderson and M. E. Fleet, J. Non-Cryst. Solids **134** (1991) 259.

[32] B. Yu, B. Chen, B. Lu, X. Yan, J. Qiu, C. Zhu, and X. Jiang, Cryst. Growth Des. **7** (2007) 30.

[33] M. Sakakura, M. Shimizu, Y. Shimostuma, K. Miura, and K. Hirao, Appl. Phys. Lett. **93** (2008) 231112.

[34] P.G. Kazansky, W. Yang, E. bricchi, J. Bovatsek, A. Arai, Y. Shimotsuma, K. Miura, and K. Hirao, Appl. Phys. Lett. **90** (2007) 151120.

[35] D.J. Durben, G.H. Wolf, Phys. Rev. B **43** (1991) 2355.

[36] C.H. Polsky, K.H. Smith, G.H. Wolf, J. Non-Cryst. Solids **248** (1999) 159.

Chapter 2

Modification of Long Range Order in Glass by Ultra Fast Laser

2.1 Introduction

In the last decade, ultrafast laser has been widely researched and explored in integrated optics [1-4] and optical data storage [5, 6]. In particular, modification inside glass materials has attracted considerable interest [2-4, 6-10]. Obvious consequences of having high accumulative energy inside a small region by irradiation of femtosecond laser pulse at a high repetition rate are thermal expansion at the irradiation center and heating above glass transition temperature in the surrounding region [10]. The extreme high temperature at the center induces elemental migration and changes glass network. Besides, thermal expansion in the center region induces stress in the surrounding area, which causes densification and form birefringence [9].

Although the unusual property of glass forming liquids is highly interested [11, 12], it is still commonly thought that supercooled liquid would convert into amorphous state with no long-range-ordering by quenching. In the present work, we discovered a novel phenomenon in which a non-ring-shaped area was observed in a Raman image of the region modified by femtosecond laser which should be considered as perfect circular symmetric. The non-ring shape is due to Raman band intensity that varies in different parts of the laser-modified region, indicating the Raman intensity is highly sensitive to the polarization of incidents Raman probe beam and the glass structure is no longer isotropic. Therefore, we propose that the observed non-ring-shaped area in the Raman image was due to the formation of a novel state of matter of long-range-ordered glass.

2.2 Experimentals

In our experiments, glass composed of $15Na_2O$-$85GeO_2$ (mol%) was prepared by using the traditional melt-quench method. Reagent grade of Na_2CO_3, and GeO_2 were used as raw materials, mixed and melted in a Pt crucible at 1450 ℃ for 1 hour in air. Then the melt was casted on a steel plate and quenched. Finally the glass was cut and polished for laser experiment. We used a regenerative amplified 800-nm Ti: sapphire laser (RegA 9000, Coherent Inc.) which emitted 70-fs, 250-KHz mode-lock pulses to irradiate the glass sample. During the experiment the laser pulse was adjusted to 1.4 μJ and laser beam was focused 100 μm below the glass surface for 60 seconds, using a 20×objective lens with a numerical aperture (NA) of 0.45. The Raman spectra and image were measured using a confocal Raman system (Tokyo Instruments; Nanofinder 30) with a 532 nm laser generated by second harmonic from a diode pumped Nd: YAG laser as the excitation source. In addition, the element distribution was measured with an EPMA (JEOL model JSM-8000).

2.3 Results and Discussion

2.3.1 Observation and Raman measurement of modified region

The ellipsoid structure induced at around the focal spot (Fig. 2.1 (a), (b)) results from refractive index changes caused by fs laser irradiation. The center of irradiated spot was in melting state and outer region is still higher than T_g during fs laser irradiation [10]. The Raman mapping result of the laser-irradiated dot is shown in Fig.1(c). The band peak at 538cm^{-1} is assigned to symmetric stretching of Ge-O-Ge bonds associated with three-membered ring formation of GeO_4 tetrahedra, and two high frequency bands at 821cm^{-1} and 912cm^{-1} can be assigned to transverse or longitudinal optic (TO or LO) splitting of the antisymmetric stretching of Ge-O-Ge bonds within the network [13].

The concentric circles in Raman image of the peak shift corresponds to the variation of Ge concentration caused by element migration, which was confirmed with the EMPA (Fig. 2.2). Usually thermal diffusion will be induced with fs laser irradiation; therefore the composition is changed from the center to the surrounding. The migration behavior depends on the physical properties related to the elements. Glass network former tend to concentrate at the center and modifiers diffuse to the lower temperature region during fs laser irradiation. However, in the present study, the non-ring-shaped region of Raman image is irrelevant to the composition changes because the composition variation caused by element migration is circular symmetrical so it is inadequate to explain the Raman mapping results.

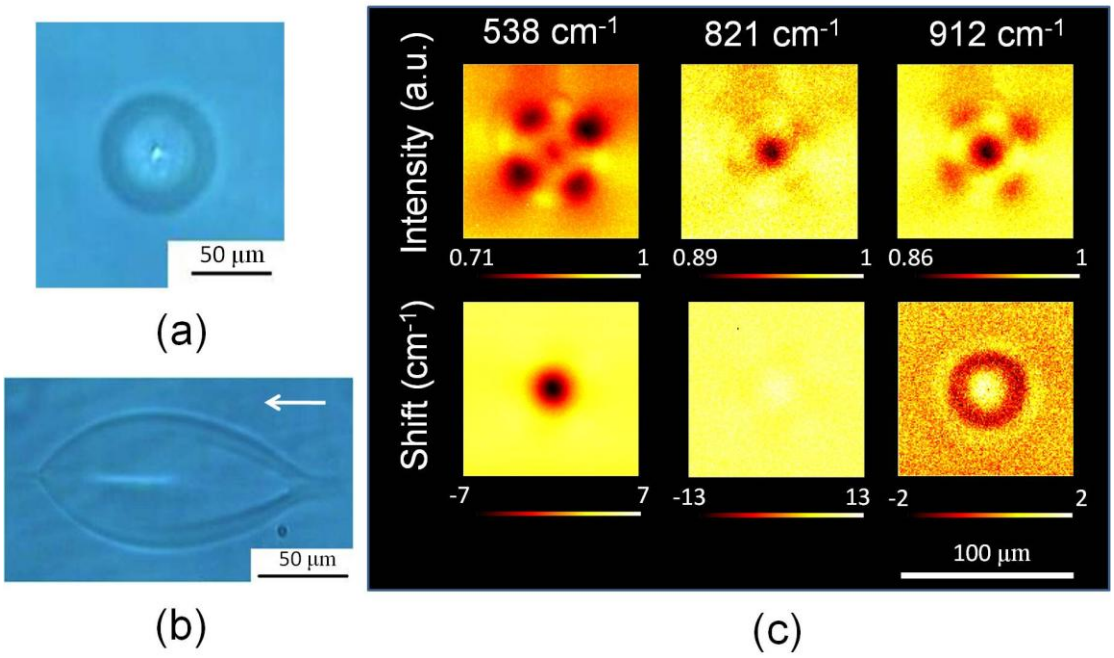

Fig 2.1 Optical microscopic and Raman image of fs laser irradiated region. (a), (b), Top (a) and side (b) view of optical transmission image of irradiated dot, the arrow indicates fs laser irradiation direction, no voids or bubble is produced as the fs laser is less intensified at the focus spot with a lower NA objective lens. (c), spatial mapping result of relative peak intensity and shift of 538cm^{-1}, 821 cm^{-1}, 912 cm^{-1} Raman band, the non-ring-shaped region overlaps with the outer structure of modified region.

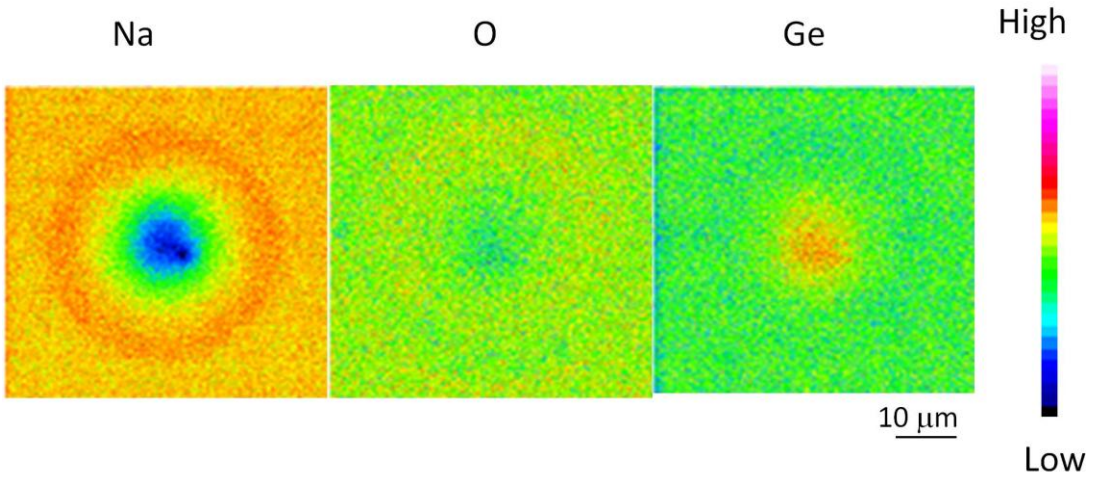

Figure 2.2 Relative concentration variation illustrated from EPMA result of laser irradiated area

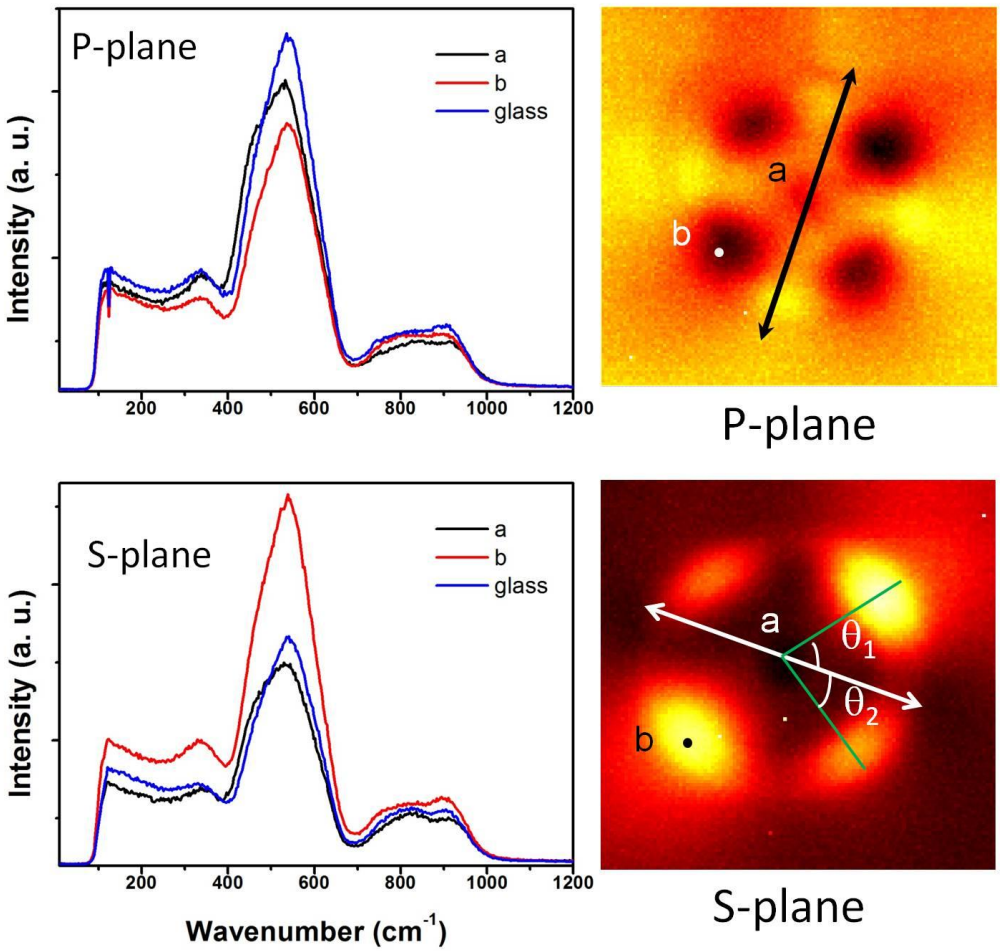

Fig. 2.3 Raman spectra from different spots and the Raman image with Raman probe beam of different polarization. The double arrows indicate the polarize direction of probe beam. The angles θ_1= 54^o θ_2=36^o shows that the non-ring-shaped region neither overlap nor be symmetric about the polarize direction so it could not explained by birefringence. The relative intensity of scattering has been reversed as the incident polarization changed from p-plane to s-plane, the decreasing of Raman intensity in un-irradiated glass is caused by the grating efficiency difference.

The changes in glass composition could also be justified from Raman spectra. Henderson [13] reported that the peak at around 450 cm^{-1} decreases rapidly as the concentration of Na_2O increases among the range from 10 mol% to 20 mol%.

On contrary to the mapping of Raman peak shifts, all three Raman mappings of the peak intensity shows two pairs of dark regions which are centrally symmetric about the irradiated center and form the non-ring-shaped region. Regarding correspond Raman band intensity of un-irradiated glass as unit, the peak at 538 cm^{-1} varies between 105% and 79% in the non-ring-shaped region. Similar phenomenon is also observed at the band of 821 cm^{-1} and 912 cm^{-1}, which changes from 108% to 97% and 104% to 92%, respectively. This unexpected result is completely different from that obtained in previous study [9], suggesting a novel structure modification occurs.

Raman spectra in different spots of the irradiated dot are presented in Fig. 2.3. No peak broadening or sharpening was observed so the Ge-O-Ge bond angle is not affected by the fs laser, furthermore, no peak related to crystalline is ever found. The Raman intensity in the non-ring-shaped region reverses as the polarization direction of the excitation source changes, indicating the Raman intensity is highly depending on the polarization of Raman probe beam when the filter for the detector does not change. Such property is exclusively observed in long-range-ordering states [14-21], suggesting that the modified glass is no-longer isotropic.

The anisotropic property of modified glass has very good thermal stability until 500 ℃ heat treatment (Fig. 2.4 b), The transition temperature is about 530 ℃ as is shown in Fig. 2.4 a. But the peak intensity and shift of 538cm^{-1}, 821 cm^{-1}, 912 cm^{-1} band are all dramatically changed due to relaxation process and non-ring-shaped region vanished after 1 hour heat treatment at 500 ℃, indicating the relaxation is

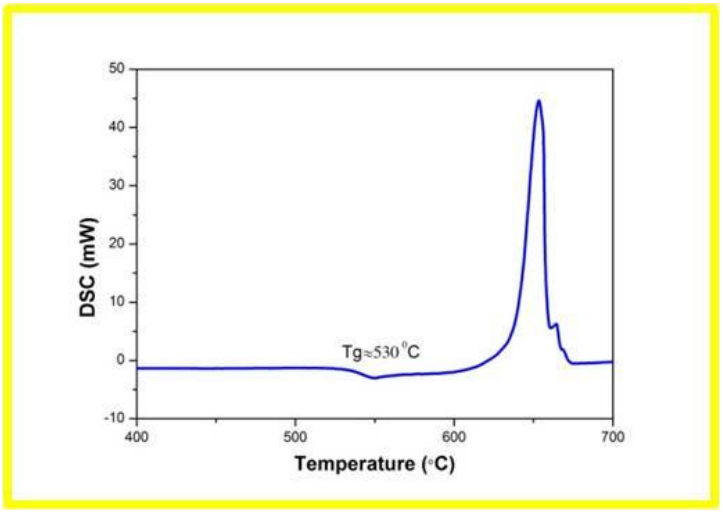

(a)

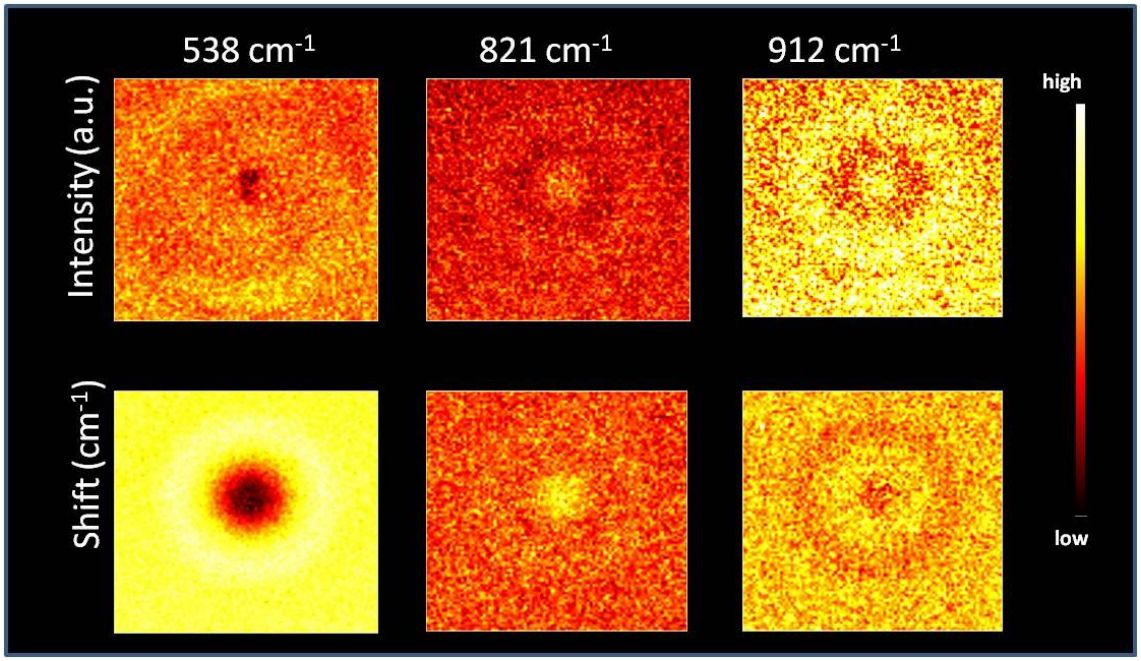

(b)

Figure 2.4 (a) DSC curve of glass of composition $85GeO_2$-$15Na_2O$ and (b) Raman image of fs laser irradiated region after heat treatment at 500 ℃ for 1h

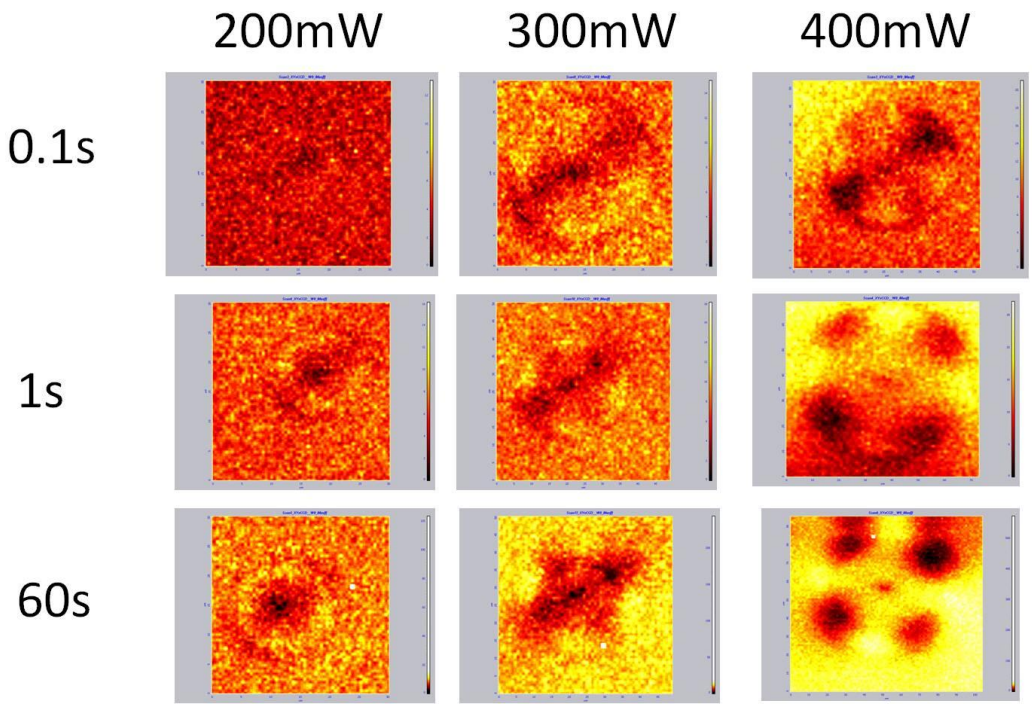

Fig. 2.5 The Raman mapping of the peak intensity of 538cm^{-1} as the laser power and irradiation time changes.

local and the modification of glass is related to quench effect when fs laser irradiation stops. From the heat treatment result we can also conclude that crystallization or phase separation did not occur during femtosond laser irradiation.

Fig. 2.5 shows that the Raman mapping result also depends on the femtosecondl laser irradiation condition. When laser power is 200 mW, the non-ring-shaped region could hardly be observed in the modified area, regardless of the long time of irradiation. However, when the laser power increases to above 300 mW, the non-ring-shaped image could be observed even the irradiation time is very short (0.1 s). In addition, the non-ring-shaped area is enhanced and becomes clearer as the exposure time increases. These results indicate the forming process of novel glass structure which is responsible for the non-ring-shaped area requires certain stress induced by femtosecond laser. Meanwhile, the dependence of time and laser power suggested that such structure is a dynamic process which changes the glass network.

We found the Raman image result is independent of rotation of the sample, which also proves that the intensity of Raman scattering at outer structure is highly sensitive to the polarization direction of probe beam. Birefringence is a possible reason. However, this phenomenon was not observed in our previous work [9], where the stress birefringence of modified area was presented and studied. So the birefringence should not be responsible for the non-ring-shaped region observed in Raman mapping. We also polished the cross section of modified spot to surface (Fig. 2.6), varied the pinhole size of confocal system to improve depth resolution (less than 2 μm) and checked the reproducibility. The non-ring-shaped image is still observed in these circumstances. These result also excluded birefringence as the possible reason of our observation since the birefringence effect is related to the transmission depth of light.

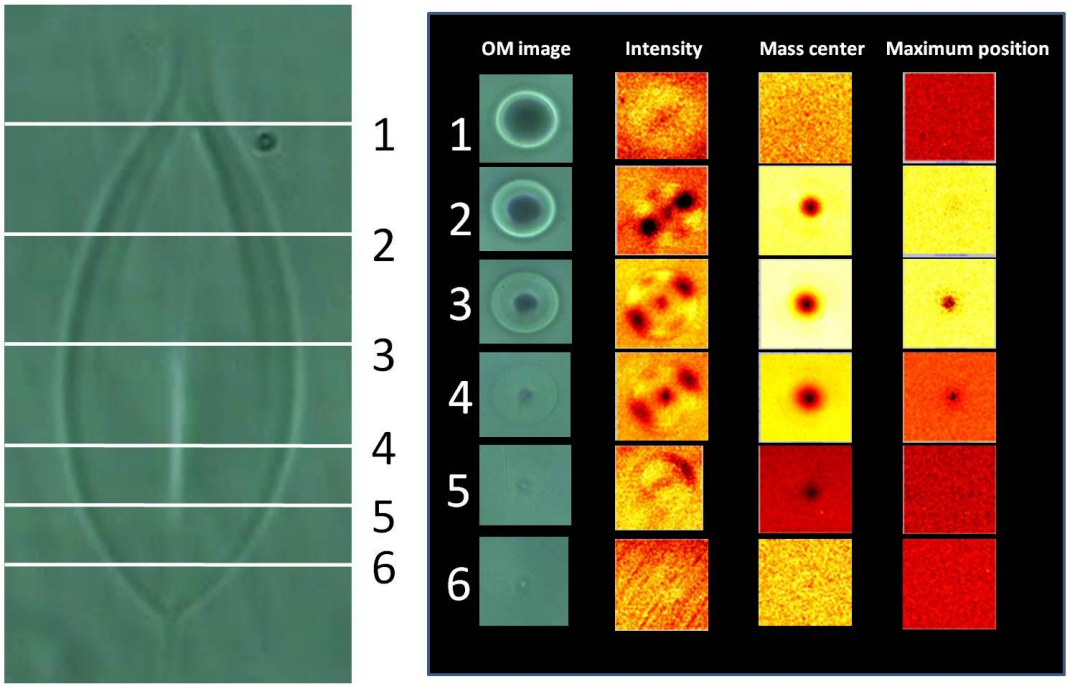

Fig. 2.6 The Raman image of cross sections at different depth of the modified region (mapping of peak intensity of 538cm^{-1})

2.3.2 Discuss and modeling for the novel structure

In this study, the most unusual phenomenon is that a completely qualitative change of experiment result is observed after exchange objective lens for fs laser irradiation with the same sample and other conditions. The contrast in the results of Raman mapping comparing with the previous work [9] is most difficult to explain.

In general, the modified region induced by laser irradiation sustained compression strain, and this pressure might explain some phenomena such as stress birefringence and densification. Additionally, many studies have been done to search for identify the pressure effect on the glass structure, suggesting that distortion of the glass structure due to pressure could change the Raman band intensity and cause peak shift [22-24].

However, the known effects of pressure do not apply to the non-ring-shaped region in the Raman image. First of all, in this study the pressure in the modified region decreased compared to that in Ref. 9 which the laser energy was so intensely focused with an objective lens of a higher NA that micro-bubbles and micro-explosion were induced, leading to a shock wave large enough to cause glass densification in the surrounding. In the previous work, we used an objective lens of higher NA (0.55) for fs laser irradiation. The radius of focal spot could be estimated by the following:

$$r = 0.61\lambda/NA \tag{2.1}$$

Since we use the same laser power at the same wavelength, so femtosecond laser was more intensely focused in the previous work. This is also confirmed with the experimental report that micro explosion and void is observed in previous work.

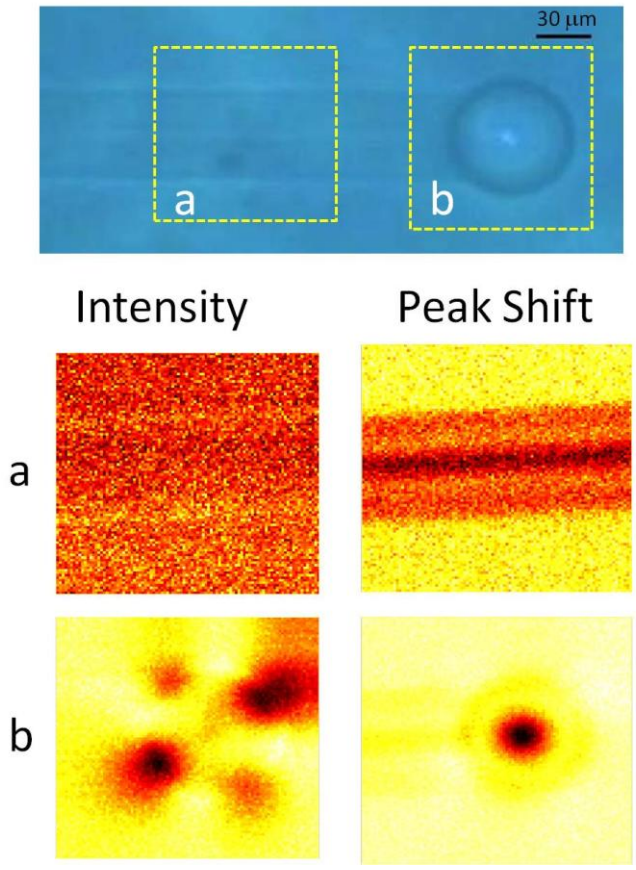

Fig. 2.7 Raman mapping of the area modified by femtosecond line-scan irradiation. (Scan speed: 100 μm/s, Laser power 350 mW)

Because femtosecond laser modification is based on multi-photon-absorption, so the temperature at the focal spot should higher in the previous work and the pressure corresponding to temperature elevation is large enough to cause densification. Besides, the stress birefringence is induced and reported. However, the non-ring-shaped region in Raman mapping was not observed when the glass is compressed and condensed, so it would be very difficult to explain non-ring-shaped region in the Raman mapping with the stress birefringence effect. Finally, stress birefringence effect may rotate the polarization direction of scattered light, but the total energy of photon could not be affected.

We also found the non-ring-shaped image could not be observed when we use fs laser to modify glass in line-scan (Fig. 2.7). From the optical microscope image we can see the boundary of modified region due to the different refractive index between modified region and glass. Such difference is mainly caused by residual stress. However, the variation of intensity of Raman scattering in the line-scan region is not observed. From the result we can conclude that neither residual stress nor stress birefringence could explain the non-ring-shaped Raman image.

Neither bubbles nor glass densification was observed in present work, suggesting the stress is not as strong as that in the previous work when we use a lower NA objective lens for femtosecond irradiation inside germanate glass. Meanwhile, the temperature at the modified region was higher than T_g when irradiated by fs laser [10], few studies have been done on the pressure effect under such high temperature in which scenario the pressure effect was different [22]. Furthermore, centrifugal temperature gradient and shocking wave were also induced with femtosecond laser irradiation, granting the modified region radial directional properties which cannot be

realized in hydraulic method used in previous works [23-24], so the known pressure effect might not be applied.

In fact, the intensity of the Raman scattered light is related to oscillating dipole moment and proportional to the square of the polarizability derivative with respect to the distortion coordinates q, So if the variation of polarizability is caused by strain, e.g. bond angle or length, a peak shift or deformation (broadening or sharpening) must be observed and could be used to evaluate stress [25-27], which is not suitable to describe the results in present work.

Another reason to explain the phenomenon in Raman image is that the glass structure is rearranged into an anisotropic state. There are also some reports about nanostructuring induced by fs laser [3], however, this type of structuring occurred in the central region where the plasma interacted with incoming femtosecond laser and is irrelevant to the outer structure of modified region.

From the discussion above, we present a model of the radial orientation of glass structure as shown in Fig. 2.8 to explain the anisotropic property, assuming Ge-O-Ge (bridging oxygen, BO) as basic vibration unit in analogue with liquid crystal to discuss bond orientation ordering. The probability distribution of BO orientation is described by orientation distribution function (ODF) [28, 29]. From benchmark work done by van Gurp, ODF can be approximated by expressing the function as a Fourier transform in terms of the Wigner rotation matrices [28]:

$$\int f(\Omega)d\Omega = \iiint \quad f(\alpha,\beta,\gamma)sin\beta d\alpha d\beta d\gamma = 1 \tag{2.2}$$

$$f(\alpha,\beta,\gamma) = \sum_{L=0}^{\infty}\sum_{m=-L}^{+L}\sum_{n=-L}^{+L}\frac{2L+1}{8\pi^2}\langle D_{mn}^{L^*}\rangle D_{mn}^{L}(\alpha,\beta,\gamma) \tag{2.3}$$

The indices L, m, and n represent the symmetry conditions under the rotations about α, β, γ, respectively. $\langle D_{mn}^{L^*}\rangle$ express the complex conjugate of statistical

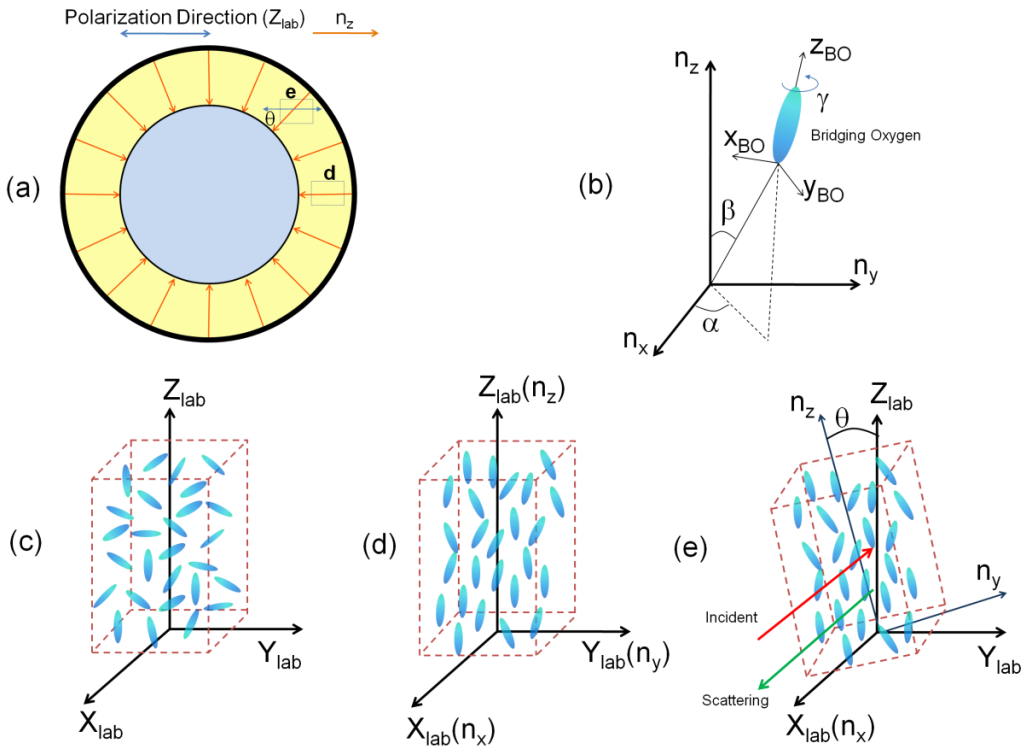

Fig. 2.8 Illustration of the anisotropic model induced inside glass. (a), The schematic demonstration of radial orientation arrangement in fs laser modified region. (b), Rotation of a BO with the reference frame $n_{x,y,z}$. The Euler angles (α, β, γ) which reflect the orientational degrees of freedom is also defined as shown. (c), (d), (e), The alignment of bridging oxygen before and after irradiation with respect to laboratory frame. (c) represents the unmodified glass. (d) and (e) represent corresponding spots indicated in (a). For consideration of simplification, other elements in glass net work such as Na, Ge and Non-bridging oxygen are not represented in the figure.

average of the function $D^{L}_{mn}(\alpha,\beta,\gamma)$ and could be regarded as order parameter. The exact orientation relationship between principal axes of polarizability of BO and the aligned direction (n_z) is unknown, so we can only assume the Placzec vibrational transition polarizability tensor **R** based on BO molecular-fixed Cartesian coordination basis (see Chapter 1). **R** is symmetric, e.g. $\alpha_{xy}=\alpha_{yx}$, because the Placzec approximation applies for transparent systems when study pure vibrational modes [30]. Rotation transformation could be expressed by a matrix T(α, β, γ), where α, β, γ represent the three Euler angles. Based on the contention proved by Jen *et al*. [29] that local field corrections are not needed, the Raman intensity from a rotated single BO in Fig. 2.8 (b) will be given by

$$I_{BO} \propto \left| e_i \cdot \left(T^{-1}(\alpha,\beta,\gamma) \cdot R \cdot T(\alpha,\beta,\gamma) \right) \cdot e_s \right|^2 \tag{2.4}$$

, where e_i, e_s are the polarization vectors of incident and scattered light, respectively. For the illumination-observation geometry of the confocal Raman system illustrated in Fig. 2.8, the intensity is presented as:

$$I_{obs} = \langle I_{BO} \rangle = \int_{\gamma=0}^{\gamma=2\pi} \int_{\beta=0}^{\beta=\pi} \int_{\alpha=0}^{\alpha=2\pi} I_{BO} \cdot f(\alpha,\beta,\gamma) sin\beta d\beta d\alpha d\gamma \tag{2.5}$$

Although the incident laser beam is plane-polarized, the scattering with arbitrary polarized direction could be detected since λ/2 plate is not equipped for the detector of Nanofinder system, so the intensity measured should be:

$$I_{mea} = G_s I_{\perp} + G_p I_{||} \tag{2.6}$$

G_s and G_p are the grating efficiency of s-plane- and p-plane- polarized Raman scattering, respectively.

First we use the liquid crystals model to describe the ordered glass structure. Usually liquid crystals is regarded as uniaxial symmetrical so that ODF is independent of α and γ and could be expressed by Legendre polynomials with only two real

parameter ⟨P2⟩ and ⟨P4⟩ [28]. So the Eq. (2.3) could be simplified:

$$f(\beta) = \frac{1}{8\pi^2}\left[1 + \frac{5}{2}\langle P2\rangle(3cos^2\beta - 1) + \frac{9}{8}\langle P4\rangle(3 - 30cos^2\beta + 30cos^4\beta)\right] \quad (2.7)$$

Substituting Eq. (2.4) and Eq. (2.7) into Eq. (2.5), result in:

$$I_{||} \propto \mathrm{C}_1(\langle P2\rangle, \langle P4\rangle, a_{xx}, \ldots a_{zz}) + \mathrm{C}_2(\langle P2\rangle, \langle P4\rangle, a_{xx}, \ldots a_{zz})\cos 2\theta + \mathrm{C}_3(\langle P2\rangle, \langle P4\rangle, a_{xx}, \ldots a_{zz})\cos 4\theta \quad (2.8)$$

$$I_{\perp} \propto \mathrm{C}_4(\langle P2\rangle, \langle P4\rangle, a_{xx}, \ldots a_{zz}) + \mathrm{C}_5(\langle P2\rangle, \langle P4\rangle, a_{xx}, \ldots a_{zz})\cos 4\theta \quad (2.9)$$

, where θ is the angle between n_z and polarization direction of incidence (Fig. 2.8). C_i could be represented as the function of ⟨P2⟩, ⟨P4⟩ and Raman polarizabilities. The intensity variation with θ is derived after insert Eq. (2.9) and Eq. (2.8) into Eq. (2.6) (in short notation):

$$I_{mea} \propto \left(\mathrm{G_pC_1} + \mathrm{G_sC_4}\right) + \mathrm{G_pC_2}\cos 2\theta + \left(\mathrm{G_pC_3} + \mathrm{G_sC_5}\right)\cos 4\theta \quad (2.10)$$

However, the model to describe liquid crystal is not valid for present work. A phase difference ϕ (~20 degree) is presented in Fig. 2.9. In fact, either uniaxial or mirror symmetry [28] granted liquid crystal a property that $I_{obs}(\theta)=I_{obs}(-\theta)$, so $I_{obs}(0)$ must be at either the maximum or minimum for liquid crystals structures [14-16]. The experiment result demonstrates that the novel structure is quite different from liquid crystals.

On the other hand, Raman scattering of oriented inorganic crystal under planar rotation where the symmetry requirement of liquid crystals is absent exhibit another property, specifically, $I_{obs}(\theta)$ is not necessarily equal to $I_{obs}(-\theta)$ [18-20]. Here we briefly introduce the crystal model in the following:

For a crystal model, the orientation is fixed so that ODF is not needed. So α, β and γ can be set to be zero and the measured Raman scattering is,

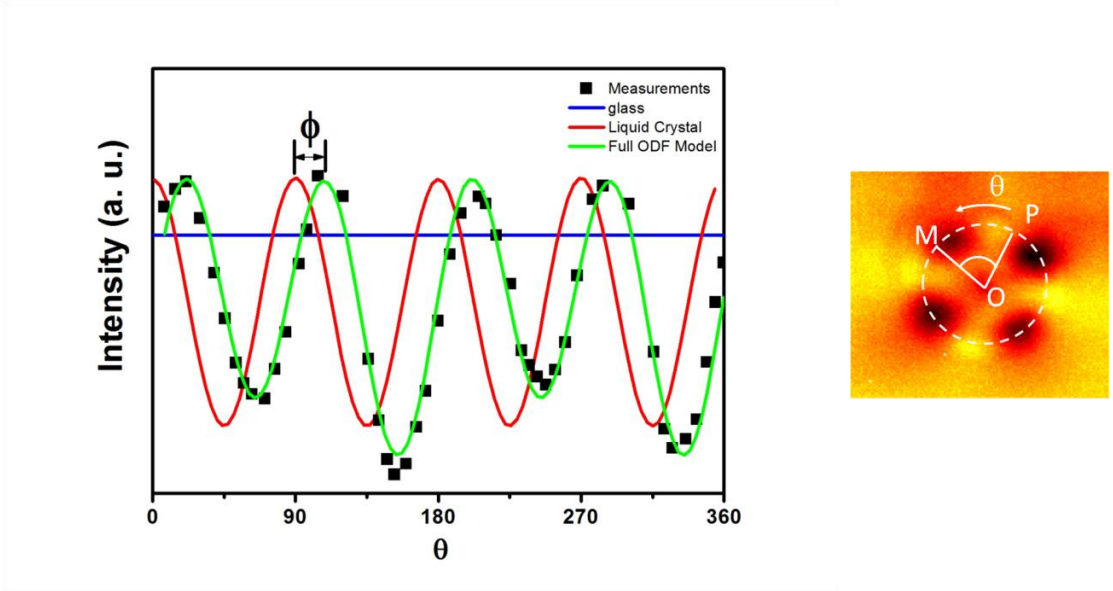

Fig. 2.9 Dependence of Raman intensity on θ and the fitting curves derived from calculations. OP is aligned with the polarization direction of incident (p-polarized). OM is 30μm. The intensity of Raman scattering from un-irradiated glass is also presented for comparison of the intensity variations. ϕ is the phase mismatch which the liquid crystal model differs from experimental results.

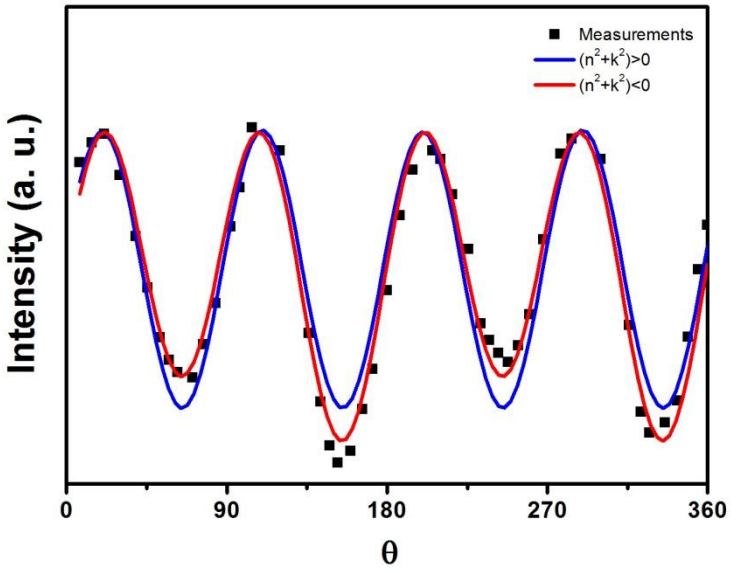

Fig. 2.10 The fitting curve based on the crystalline model

$$I_{obs} \propto m^2 G_p + (n^2 + k^2)\left(\frac{G_s+G_p}{2}\right) - 2G_p m\sqrt{n^2+k^2}\cos(2\theta+\varphi)$$
$$+(n^2+k^2)\left(\frac{G_p-G_s}{2}\right)\cos(4\theta+2\varphi) \quad (2.11)$$

, where $m = \frac{\alpha_{yy}+\alpha_{zz}}{2}$, $n = \frac{\alpha_{yy}-\alpha_{zz}}{2}$, $k = \alpha_{yz}$ and $\varphi = \tan^{-1}\frac{2\alpha_{yz}}{\alpha_{yy}-\alpha_{zz}}$

The variable terms in the above expression are only those containing cos(2θ+φ) or cos(4θ+2φ), with their period π and π/2. The fitting result is plotted in Fig. 2.10. Compared with liquid crystal model, the crystal model fits well in the positions of crest, but much poorer at the trough. The reason is that the term $(n^2 + k^2)$ must be positive. Or the Raman polarizability is complex, which is unrealistic.

So neither liquid crystals model nor crystal model is suitable for describing the ordered phase induced inside glass and a model which combines features of both crystal and liquid crystals must be applied to describe the novel structure. For rigor consideration, the orientation of BO is not symmetric about n_z and the full ODF expression is required. Usually L in the ODF function takes value from 0 to 4, therefore the measured Raman signal is:

$$I'_{mea} \propto (G_p V_1 + G_s V_6) + G_p V_2 \cos 2\theta + G_p V_4 \sin 2\theta$$
$$+(G_p V_3 + G_s V_7)\cos 4\theta + (G_p V_5 + G_s V_8)\sin 4\theta \quad (2.12)$$

The expression of V_i is given in Appendix. With the asymmetric factor sin2θ and sin4θ, the equation above could well explain the Raman intensity variations (Fig. 2.8). Unfortunately, quantitatively description of the ordered glass structure is not available due to the limited information we can get. The present work is dedicated to explain unexpected Raman image with the simplest model and prove a new state of matter was formed. The same explanation could be appled to the non-ring-shaped region observed in mapping of 821 cm^{-1} and 912 cm^{-1} band.

2.3.3 The mechanism of the ordered glass forming

The rearrangement property exists in different glasses, as we also observed a non-ring-shaped region in a Raman image of sodium silicate glass and sodium silicate germanate glasses after fs laser irradiation, as is shown in Fig. 2. 11. The Raman bands from these glasses are all originated from bridging oxygen symmetric vibrations. The same origination may explain some similarities of the non-ring-shaped region pattern in the Raman mapping. These observations suggest the ordered rearrangement with femtosecond laser might be universal property of inorganic oxide glasses. However, attempts to induce such structure inside quarts and germanium dioxide glass (Fig. 2.11) are failed indicates that the non-bridge oxygen defects and the viscosity might be an important factor during the kinetic process of structure orientation rearrangements.

Additionally, the mechanism of how the long-range-order structure is formed without crystallization in glass requires further investigation. It is commonly known that when polyvinyl alcohol is heated and stretched in a given direction, its long hydrocarbon molecules becoming aligned in the process. In our experiment the ordered glass phase could only be induced in the outer structure where the temperature is not as high as the center during fs laser irradiation. So we propose that the chains of [GeO_4] is formed when glass is heated above T_g but not melted at the outer structure, then the chains get aligned under the stress caused by thermal expansion. Furthermore, centrifugal temperature gradient and shocking wave were also induced with fs laser irradiation, granting the modified region radial directional properties which cannot be realized with hydraulic method. The aligned structure is

frozen to form the ordered glass by quenching when fs laser stopped.

However, the similarity between germinate glass and polyvinyl alcohol is never expected in known theory and is under further investigation. We also propose that the ordered structure could not be induced with an objective lens of high numerical aperture [10] because the strain is too high so that the free space between tetrahedras is not enough for the alignment process.

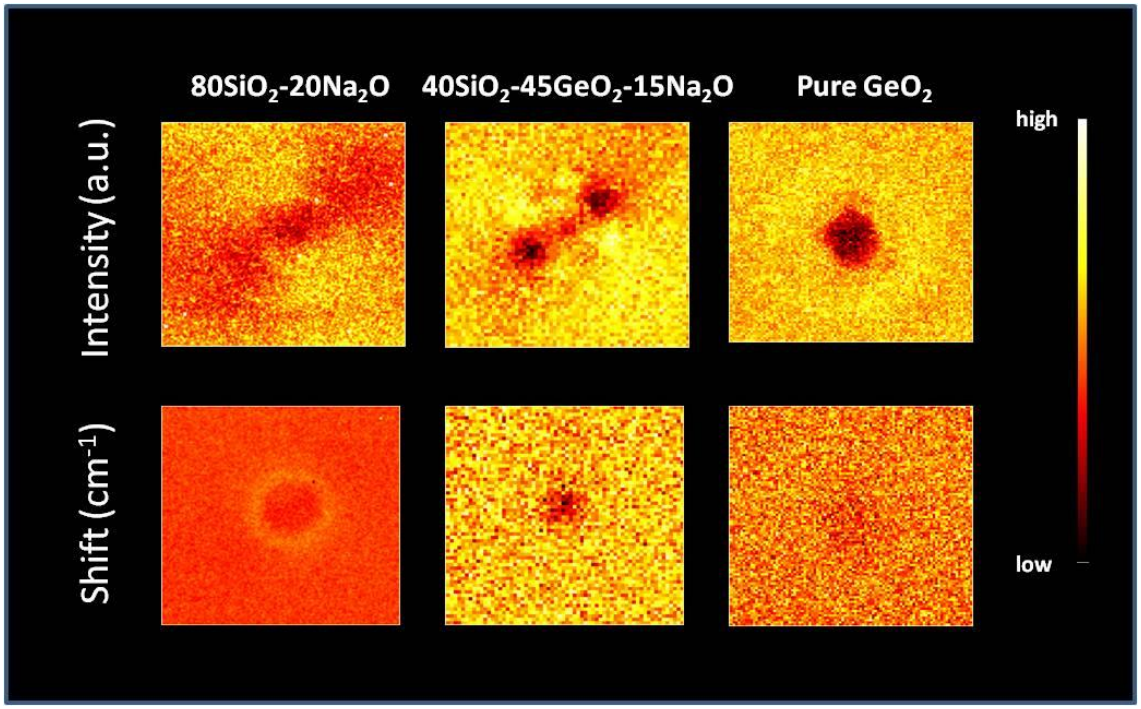

Fig. 2.11 Spatial map of peak intensity and frequency shift of sodium silicate (530 cm^{-1}), sodium silicate germinate (560 cm^{-1}) and germanium dioxide glass (430 cm^{-1}). All these Raman band are related to the symmetric BO vibration in the corresponding glasses

2.4 Conclusion

In summary, we observed a non-ring-shaped region in a Raman image of a modified area after we irradiate glass sample with lower NA objective lens. The Raman mapping indicates a new state of matter is induced. The existent of such state of matter also indicates structure orientation of inorganic oxide glass could be controlled by mechanical process, a phenomenon that had so far never been reported or expected. This kind of structure would provide a novel method to control glass structure and property via processing supercooled liquid as well as new insight into the basic physical behavior of supercooled liquid, rheology physics, and ultra fast laser micro-structuring mechanism.

2.5 References

[1] W. J. Yang, P. G. Kazansky, and Y. P. Svirk, Nat. Photonics **2** (2008) 99.

[2] K. Miura, J. R. Qiu, T. Mitsuyu, and K. Hirao, Opt. Lett. **25** (2000) 408.

[3] Y. Shimotsuma, P. G. Kazansky, J. R. Qiu, and K. Hirao, Phys. Rev. Lett. **91** (2003) 247405.

[4] W. Watanabe, T. Asano, K. Yamada, K. Itoh, and J. Nishii, Opt. Lett. **28** (2003) 2491.

[5] E. N. Glezer, M. Milosavljevic, L. Huang, R. J. Finlay, T.-H. Her, J. P. Callan, and E. Mazur, Opt. Lett. **21** (1996) 2023.

[6] J. R. Qiu, X. W. Jiang, C. S. Zhu, M. Shirai, J. H. Si, N. Jiang, and K. Hirao, Angew. Chem. Int. Edn. **43** (2004) 2230.

[7] S. Kanehira, J. H. Si, J. R. Qiu, K. Fujita, and Hirao, Nano Lett. **5** (2005) 1591

[8] M. Shimizu, K. Miura, M. Sakakura, M. Nishi, Y. Shimotsuma, S. Kanehira, T. Nakaya, and K. Hirao, Appl. Phys. A **100** (2010) 1001.

[9] Y. Liu, M. Shimizu, X. Wang, B. Zhu, M. Sakakura, Y. Shimotsuma, J. R. Qiu, K. Miura, and K. Hirao, Chem. Phys. Lett. **477** (2009) 122.

[10] M. Sakakura, M. Shimizu, Y. Shimotsuma, K. Miura, and K. Hirao, Appl. Phys. Lett. **93** (2008) 231112.

[11] J. D. Steveson, and P. G. Wolynes, Nat. Phys. **6** (2010) 62.

[12] A. Furukawa, and H. Tanaka, Nat. Mater. **8** (2009) 601.

[13] G. S. Henderson, and M. E. Fleet, J. Non-Cryst. Solids **134** (1991) 259.

[14] A. Sanchez-Castillo, M. A. Osipov, and F. Giesselmann, Phys. Rev. E **81** (2010) 021707.

[15] R. Pérez, S. Banda, and Z. Qunaies, J. Appl. Phys. **103** (2008) 074302.

[16] C. D. Southern, and H. F. Gleeson, Eur. Phys. J. E **24** (2007) 119.

[17] J. F. Blach, A. Daoudi, J. M. Buisine, and D. Bormann, Vib. Spectrosc. **39** (2005) 31.

[18] J. B. Hopkins, and L. A. Farrow, J. Appl. Phys. **59** (1986) 1103.

[19] M. Becker, H. Scheel, S. Christiansen, and H. P. Strunk, J. Appl. Phys. **101** (2007) 063531.

[20] K. Mizoguchi, and S. Nakashima, J. Appl. Phys. **65** (1989) 2583.

[21] M. Deluca, M. Higashino, and G. Pezzotti, Appl. Phys. Lett. **91** (2007) 091906.

[22] D. L. Farber, and Q. Williams, Science **256** (1992) 1427.

[23] D. J. Durben, and G. H. Wolf, Phys. Rev. B **43** (1991) 2355.

[24] C. H. Polsky, K. H. Smith, and G. H. Wolf, J. Non-Cryst. Solids **248** (1999) 159.

[25] D. R. Tallant, T. A. Michalske, and W. L. Smith, J. Non-Cryst. Solids. **106** (1988) 380.

[26] X. G. Yang, D. J. Bannister, and R. J. Young, J. Am. Ceram. Soc. **79** (1996) 1868.

[27] E. Anastassakis, A. Pinczuk, and E. Burstein, Solid State Commun. **8** (1970) 133.

[28] M. Gurp, Colloid Polym. Sci. **273** (1995) 607.

[29] S. Jen, N. A. Clark, P. S. Pershan and E. B. Priestle, J. Chem. Phys. **66** (1977) 4635.

[30] D. A. Long, The Raman Effect: A Unified Treatment of the Theory of Raman Scattering by Molecules. (2002)

2.6 Appendix

2.6.1 Expression of C_i

C_i could be represented as the function of ⟨P2⟩, ⟨P4⟩ and Raman polarizabilities.

Shown as follows:

$$
\begin{aligned}
C_1 = {} & \frac{\alpha_{xx}^2}{5} - \frac{\langle P2\rangle\alpha_{xx}^2}{14} + \frac{27\langle P4\rangle\alpha_{xx}^2}{2240} + \frac{4\alpha_{xy}^2}{15} - \frac{2\langle P2\rangle\alpha_{xy}^2}{21} + \frac{9\langle P4\rangle\alpha_{xy}^2}{560} + \frac{4\alpha_{xz}^2}{15} + \frac{\langle P2\rangle\alpha_{xz}^2}{21} \\
& - \frac{9\langle P4\rangle\alpha_{xz}^2}{140} + \frac{2\alpha_{xx}\alpha_{yy}}{15} - \frac{\langle P2\rangle\alpha_{xx}\alpha_{yy}}{21} + \frac{9\langle P4\rangle\alpha_{xx}\alpha_{yy}}{1120} + \frac{\alpha_{yy}^2}{5} \\
& - \frac{\langle P2\rangle\alpha_{yy}^2}{14} + \frac{27\langle P4\rangle\alpha_{yy}^2}{2240} + \frac{4\alpha_{yz}^2}{15} + \frac{\langle P2\rangle\alpha_{yz}^2}{21} - \frac{9\langle P4\rangle\alpha_{yz}^2}{140} + \frac{2\alpha_{xx}\alpha_{zz}}{15} \\
& + \frac{\langle P2\rangle\alpha_{xx}\alpha_{zz}}{42} - \frac{9\langle P4\rangle\alpha_{xx}\alpha_{zz}}{280} + \frac{2\alpha_{yy}\alpha_{zz}}{15} + \frac{\langle P2\rangle\alpha_{yy}\alpha_{zz}}{42} - \frac{9\langle P4\rangle\alpha_{yy}\alpha_{zz}}{280} \\
& + \frac{\alpha_{zz}^2}{5} + \frac{\langle P2\rangle\alpha_{zz}^2}{7} + \frac{9\langle P4\rangle\alpha_{zz}^2}{280}
\end{aligned}
$$

$$
\begin{aligned}
C_2 = {} & -\frac{3}{14}\langle P2\rangle\alpha_{xx}^2 + \frac{3}{112}\langle P4\rangle\alpha_{xx}^2 - \frac{2}{7}\langle P2\rangle\alpha_{xy}^2 + \frac{1}{28}\langle P4\rangle\alpha_{xy}^2 + \frac{1}{7}\langle P2\rangle\alpha_{xz}^2 \\
& - \frac{1}{7}\langle P4\rangle\alpha_{xz}^2 - \frac{1}{7}\langle P2\rangle\alpha_{xx}\alpha_{yy} + \frac{1}{56}\langle P4\rangle\alpha_{xx}\alpha_{yy} - \frac{3}{14}\langle P2\rangle\alpha_{yy}^2 \\
& + \frac{3}{112}\langle P4\rangle\alpha_{yy}^2 + \frac{1}{7}\langle P2\rangle\alpha_{yz}^2 - \frac{1}{7}\langle P4\rangle\alpha_{yz}^2 + \frac{1}{14}\langle P2\rangle\alpha_{xx}\alpha_{zz} \\
& - \frac{1}{14}\langle P4\rangle\alpha_{xx}\alpha_{zz} + \frac{1}{14}\langle P2\rangle\alpha_{yy}\alpha_{zz} - \frac{1}{14}\langle P4\rangle\alpha_{yy}\alpha_{zz} + \frac{3}{7}\langle P2\rangle\alpha_{zz}^2 \\
& + \frac{1}{14}\langle P4\rangle\alpha_{zz}^2
\end{aligned}
$$

$$
\begin{aligned}
C_3 = {} & \langle P4\rangle\left(\frac{3}{64}\alpha_{xx}^2 + \frac{1}{16}\alpha_{xy}^2 - \frac{1}{4}\alpha_{xz}^2 + \frac{1}{32}\alpha_{xx}\alpha_{yy} + \frac{3}{64}\alpha_{yy}^2 - \frac{1}{4}\alpha_{yz}^2 - \frac{1}{8}\alpha_{xx}\alpha_{zz}\right. \\
& \left. - \frac{1}{8}\alpha_{yy}\alpha_{zz} + \frac{1}{8}\alpha_{zz}^2\right)
\end{aligned}
$$

$$
\begin{aligned}
C_4 = {} & \frac{\alpha_{xx}^2}{15} - \frac{\langle P2\rangle\alpha_{xx}^2}{42} + \frac{9\langle P4\rangle\alpha_{xx}^2}{2240} + \frac{\alpha_{xy}^2}{5} - \frac{\langle P2\rangle\alpha_{xy}^2}{7} + \frac{3\langle P4\rangle\alpha_{xy}^2}{560} + \frac{\alpha_{xz}^2}{5} + \frac{\langle P2\rangle\alpha_{xz}^2}{14} \\
& - \frac{3\langle P4\rangle\alpha_{xz}^2}{140} - \frac{\alpha_{xx}\alpha_{yy}}{15} + \frac{2\langle P2\rangle\alpha_{xx}\alpha_{yy}}{21} + \frac{3\langle P4\rangle\alpha_{xx}\alpha_{yy}}{1120} + \frac{\alpha_{yy}^2}{15} \\
& - \frac{\langle P2\rangle\alpha_{yy}^2}{42} + \frac{9\langle P4\rangle\alpha_{yy}^2}{2240} + \frac{\alpha_{yz}^2}{5} + \frac{\langle P2\rangle\alpha_{yz}^2}{14} - \frac{3\langle P4\rangle\alpha_{yz}^2}{140} - \frac{\alpha_{xx}\alpha_{zz}}{15} \\
& - \frac{\langle P2\rangle\alpha_{xx}\alpha_{zz}}{21} - \frac{3\langle P4\rangle\alpha_{xx}\alpha_{zz}}{280} - \frac{\alpha_{yy}\alpha_{zz}}{15} - \frac{\langle P2\rangle\alpha_{yy}\alpha_{zz}}{21} - \frac{3\langle P4\rangle\alpha_{yy}\alpha_{zz}}{280} \\
& + \frac{\alpha_{zz}^2}{15} + \frac{\langle P2\rangle\alpha_{zz}^2}{21} + \frac{3\langle P4\rangle\alpha_{zz}^2}{280}
\end{aligned}
$$

$$C_5 = \langle \mathrm{P4} \rangle \left(-\frac{3}{64}\alpha_{xx}^2 - \frac{1}{16}\alpha_{xy}^2 + \frac{1}{4}\alpha_{xz}^2 - \frac{1}{32}\alpha_{xx}\alpha_{yy} - \frac{3}{64}\alpha_{yy}^2 + \frac{1}{4}\alpha_{yz}^2 + \frac{1}{8}\alpha_{xx}\alpha_{zz} + \frac{1}{8}\alpha_{yy}\alpha_{zz} - \frac{1}{8}\alpha_{zz}^2 \right)$$

2.6.2 Expression of V_i

The full expression of V_i is so prolix that it is only partially given in this supporting material. Notice that only for isotropic system all parameter is zero except $\langle D_{00}^{0^*} \rangle$ ($\langle D_{00}^{0^*} \rangle \equiv 1$), and only V_1 and V_6 contain $\langle D_{00}^{0^*} \rangle$. So any system which Raman scattering intensity is dependent on the polarization direction of incident light is not isotropic and $\langle D_{mn}^{L^*} \rangle$ could be used as order parameters. *f*(α, β, γ) is always real and not small than 0 according to the definition, so Vi (i=1, 2, …7, 8) are all real although complex is included in the expression.

$$\begin{aligned}
V_1 = {} & \frac{1}{5}\pi^4\alpha_{xx}^2\langle D_{00}^{0^*} \rangle + \frac{4}{15}\pi^4\alpha_{xy}^2\langle D_{00}^{0^*} \rangle + \frac{4}{15}\pi^4\alpha_{xz}^2\langle D_{00}^{0^*} \rangle + \frac{2}{15}\pi^4\alpha_{xx}\alpha_{yy}\langle D_{00}^{0^*} \rangle \\
& + \frac{1}{5}\pi^4\alpha_{yy}^2\langle D_{00}^{0^*} \rangle + \frac{4}{15}\pi^4\alpha_{yz}^2\langle D_{00}^{0^*} \rangle + \frac{2}{15}\pi^4\alpha_{xx}\alpha_{zz}\langle D_{00}^{0^*} \rangle \\
& + \frac{2}{15}\pi^4\alpha_{yy}\alpha_{zz}\langle D_{00}^{0^*} \rangle + \frac{1}{5}\pi^4\alpha_{zz}^2\langle D_{00}^{0^*} \rangle - \frac{3}{28}\pi^4\alpha_{xx}^2\langle D_{-2-2}^{2^*} \rangle \\
& - \frac{3}{14}i\pi^4\alpha_{xx}\alpha_{yy}\langle D_{-2-2}^{2^*} \rangle - \frac{1}{14}\pi^4\alpha_{xz}^2\langle D_{-2-2}^{2^*} \rangle - \frac{3}{14}i\pi^4\alpha_{xy}\alpha_{yy}\langle D_{-2-2}^{2^*} \rangle \\
& + \cdots + \frac{9\pi^4\alpha_{yy}\alpha_{yz}\langle D_{32}^{4^*} \rangle}{64\sqrt{14}} - \frac{3i\pi^4\alpha_{xx}\alpha_{xz}\langle D_{34}^{4^*} \rangle}{32\sqrt{2}} - \frac{3\pi^4\alpha_{xy}\alpha_{xz}\langle D_{34}^{4^*} \rangle}{16\sqrt{2}} \\
& + \frac{3i\pi^4\alpha_{xz}\alpha_{yy}\langle D_{34}^{4^*} \rangle}{32\sqrt{2}} - \frac{3\pi^4\alpha_{xx}\alpha_{yz}\langle D_{34}^{4^*} \rangle}{32\sqrt{2}} + \frac{3i\pi^4\alpha_{xy}\alpha_{yz}\langle D_{34}^{4^*} \rangle}{16\sqrt{2}} \\
& + \frac{3\pi^4\alpha_{yy}\alpha_{yz}\langle D_{34}^{4^*} \rangle}{32\sqrt{2}} + \frac{3}{128}\pi^4\alpha_{xx}^2\langle D_{44}^{4^*} \rangle - \frac{3}{32}i\pi^4\alpha_{xx}\alpha_{xy}\langle D_{44}^{4^*} \rangle \\
& - \frac{3}{32}\pi^4\alpha_{xy}^2\langle D_{44}^{4^*} \rangle - \frac{3}{64}\pi^4\alpha_{xx}\alpha_{yy}\langle D_{44}^{4^*} \rangle + \frac{3}{32}i\pi^4\alpha_{xy}\alpha_{yy}\langle D_{44}^{4^*} \rangle \\
& + \frac{3}{128}\pi^4\alpha_{yy}^2\langle D_{44}^{4^*} \rangle
\end{aligned}$$

$$
\begin{aligned}
V_2 = {} & \frac{3}{28}\pi^4\alpha_{xx}^2\langle D_{-2-2}^{2^*}\rangle + \frac{3}{14}i\pi^4\alpha_{xx}\alpha_{xy}\langle D_{-2-2}^{2^*}\rangle + \frac{1}{14}\pi^4\alpha_{xz}^2\langle D_{-2-2}^{2^*}\rangle \\
& + \frac{3}{14}i\pi^4\alpha_{xy}\alpha_{yy}\langle D_{-2-2}^{2^*}\rangle - \frac{3}{28}\pi^4\alpha_{yy}^2\langle D_{-2-2}^{2^*}\rangle + \frac{1}{7}i\pi^4\alpha_{xz}\alpha_{yz}\langle D_{-2-2}^{2^*}\rangle \\
& - \frac{1}{14}\pi^4\alpha_{yz}^2\langle D_{-2-2}^{2^*}\rangle + \frac{1}{28}\pi^4\alpha_{xx}\alpha_{zz}\langle D_{-2-2}^{2^*}\rangle + \frac{1}{14}i\pi^4\alpha_{xy}\alpha_{zz}\langle D_{-2-2}^{2^*}\rangle \\
& - \frac{1}{28}\pi^4\alpha_{yy}\alpha_{zz}\langle D_{-2-2}^{2^*}\rangle - \frac{3}{14}\sqrt{\frac{3}{2}}\pi^4\alpha_{xx}^2\langle D_{-20}^{2^*}\rangle \\
& - \frac{3}{7}i\sqrt{\frac{3}{2}}\pi^4\alpha_{xx}\alpha_{xy}\langle D_{-20}^{2^*}\rangle - \frac{1}{7}\sqrt{\frac{3}{2}}\pi^4\alpha_{xz}^2\langle D_{-20}^{2^*}\rangle \\
& - \frac{3}{7}i\sqrt{\frac{3}{2}}\pi^4\alpha_{xy}\alpha_{yy}\langle D_{-20}^{2^*}\rangle + \quad \ldots + \frac{3\pi^4\alpha_{yy}\alpha_{yz}\langle D_{32}^{4^*}\rangle}{16\sqrt{14}} + \frac{i\pi^4\alpha_{xx}\alpha_{xz}\langle D_{34}^{4^*}\rangle}{8\sqrt{2}} \\
& + \frac{\pi^4\alpha_{xx}\alpha_{xz}\langle D_{34}^{4^*}\rangle}{4\sqrt{2}} - \frac{i\pi^4\alpha_{xz}\alpha_{yy}\langle D_{34}^{4^*}\rangle}{8\sqrt{2}} + \frac{\pi^4\alpha_{xx}\alpha_{yz}\langle D_{34}^{4^*}\rangle}{8\sqrt{2}} \\
& - \frac{i\pi^4\alpha_{xy}\alpha_{yz}\langle D_{34}^{4^*}\rangle}{4\sqrt{2}} - \frac{\pi^4\alpha_{yy}\alpha_{yz}\langle D_{34}^{4^*}\rangle}{8\sqrt{2}} - \frac{1}{32}\pi^4\alpha_{xx}^2\langle D_{44}^{4^*}\rangle \\
& + \frac{1}{8}i\pi^4\alpha_{xx}\alpha_{xy}\langle D_{44}^{4^*}\rangle + \frac{1}{8}\pi^4\alpha_{xy}^2\langle D_{44}^{4^*}\rangle + \frac{1}{16}\pi^4\alpha_{xx}\alpha_{yy}\langle D_{44}^{4^*}\rangle \\
& - \frac{1}{8}i\pi^4\alpha_{xy}\alpha_{yy}\langle D_{44}^{4^*}\rangle - \frac{1}{32}\pi^4\alpha_{yy}^2\langle D_{44}^{4^*}\rangle
\end{aligned}
$$

$$
\begin{aligned}
V_3 = {} & \frac{1}{128}\pi^4\alpha_{xx}^2\langle D_{-4-4}^{4^*}\rangle + \frac{1}{32}i\pi^4\alpha_{xx}\alpha_{xy}\langle D_{-4-4}^{4^*}\rangle - \frac{1}{32}\pi^4\alpha_{xy}^2\langle D_{-4-4}^{4^*}\rangle \\
& - \frac{1}{64}\pi^4\alpha_{xx}\alpha_{yy}\langle D_{-4-4}^{4^*}\rangle - \frac{1}{32}i\pi^4\alpha_{xy}\alpha_{yy}\langle D_{-4-4}^{4^*}\rangle + \frac{1}{128}\pi^4\alpha_{yy}^2\langle D_{-4-4}^{4^*}\rangle \\
& - \frac{1}{64}\sqrt{7}\pi^4\alpha_{xx}^2\langle D_{-4-2}^{4^*}\rangle - \frac{1}{16}i\sqrt{7}\pi^4\alpha_{xx}\alpha_{xy}\langle D_{-4-2}^{4^*}\rangle \\
& + \frac{1}{16}\sqrt{7}\pi^4\alpha_{xy}^2\langle D_{-4-2}^{4^*}\rangle + \frac{1}{32}\sqrt{7}\pi^4\alpha_{xx}\alpha_{yy}\langle D_{-4-2}^{4^*}\rangle \\
& + \frac{1}{16}i\sqrt{7}\pi^4\alpha_{xy}\alpha_{yy}\langle D_{-4-2}^{4^*}\rangle - \frac{1}{64}\sqrt{7}\pi^4\alpha_{yy}^2\langle D_{-4-2}^{4^*}\rangle \\
& + \frac{1}{64}\sqrt{\frac{35}{2}}\pi^4\alpha_{xx}^2\langle D_{-40}^{4^*}\rangle + \cdots + \frac{i\pi^4\alpha_{xz}\alpha_{yy}\langle D_{34}^{4^*}\rangle}{32\sqrt{2}} - \frac{\pi^4\alpha_{xx}\alpha_{yz}\langle D_{34}^{4^*}\rangle}{32\sqrt{2}} \\
& + \frac{i\pi^4\alpha_{xy}\alpha_{yz}\langle D_{34}^{4^*}\rangle}{16\sqrt{2}} + \frac{\pi^4\alpha_{yy}\alpha_{yz}\langle D_{34}^{4^*}\rangle}{32\sqrt{2}} + \frac{1}{128}\pi^4\alpha_{xx}^2\langle D_{44}^{4^*}\rangle \\
& - \frac{1}{32}i\pi^4\alpha_{xx}\alpha_{xy}\langle D_{44}^{4^*}\rangle - \frac{1}{32}\pi^4\alpha_{xy}^2\langle D_{44}^{4^*}\rangle - \frac{1}{64}\pi^4\alpha_{xx}\alpha_{yy}\langle D_{44}^{4^*}\rangle \\
& + \frac{1}{32}i\pi^4\alpha_{xy}\alpha_{yy}\langle D_{44}^{4^*}\rangle + \frac{1}{128}\pi^4\alpha_{yy}^2\langle D_{44}^{4^*}\rangle
\end{aligned}
$$

$$
\begin{aligned}
V_4 = {} & \frac{3}{14}\pi^4\alpha_{xx}^2\langle D_{-2-1}^{2^*}\rangle + \frac{3}{7}i\pi^4\alpha_{xx}\alpha_{xy}\langle D_{-2-1}^{2^*}\rangle + \frac{1}{7}\pi^4\alpha_{xz}^2\langle D_{-2-1}^{2^*}\rangle \\
& + \frac{3}{7}i\pi^4\alpha_{xy}\alpha_{yy}\langle D_{-2-1}^{2^*}\rangle - \frac{3}{14}\pi^4\alpha_{yy}^2\langle D_{-2-1}^{2^*}\rangle + \frac{2}{7}i\pi^4\alpha_{xz}\alpha_{yz}\langle D_{-2-1}^{2^*}\rangle \\
& - \frac{1}{7}\pi^4\alpha_{yz}^2\langle D_{-2-1}^{2^*}\rangle + \frac{1}{14}\pi^4\alpha_{xx}\alpha_{zz}\langle D_{-2-1}^{2^*}\rangle + \frac{1}{7}i\pi^4\alpha_{xy}\alpha_{zz}\langle D_{-2-1}^{2^*}\rangle \\
& - \frac{1}{14}\pi^4\alpha_{yy}\alpha_{zz}\langle D_{-2-1}^{2^*}\rangle - \frac{3}{14}\pi^4\alpha_{xx}^2\langle D_{-21}^{2^*}\rangle - \frac{3}{7}i\pi^4\alpha_{xx}\alpha_{xy}\langle D_{-21}^{2^*}\rangle \\
& - \frac{1}{7}\pi^4\alpha_{xz}^2\langle D_{-21}^{2^*}\rangle - \frac{3}{7}i\pi^4\alpha_{xy}\alpha_{yy}\langle D_{-21}^{2^*}\rangle + \cdots + \frac{i\pi^4\alpha_{xz}\alpha_{yz}\langle D_{23}^{4^*}\rangle}{\sqrt{14}} \\
& + \frac{\pi^4\alpha_{yz}^2\langle D_{23}^{4^*}\rangle}{2\sqrt{14}} - \frac{\pi^4\alpha_{xx}\alpha_{zz}\langle D_{23}^{4^*}\rangle}{4\sqrt{14}} + \frac{i\pi^4\alpha_{xy}\alpha_{zz}\langle D_{23}^{4^*}\rangle}{2\sqrt{14}} + \frac{\pi^4\alpha_{yy}\alpha_{zz}\langle D_{23}^{4^*}\rangle}{4\sqrt{14}} \\
& - \frac{1}{8}i\pi^4\alpha_{xx}\alpha_{xz}\langle D_{33}^{4^*}\rangle - \frac{1}{4}\pi^4\alpha_{xy}\alpha_{xz}\langle D_{33}^{4^*}\rangle + \frac{1}{8}i\pi^4\alpha_{xz}\alpha_{yy}\langle D_{33}^{4^*}\rangle \\
& - \frac{1}{8}\pi^4\alpha_{xx}\alpha_{yz}\langle D_{33}^{4^*}\rangle + \frac{1}{4}i\pi^4\alpha_{xy}\alpha_{yz}\langle D_{33}^{4^*}\rangle + \frac{1}{8}\pi^4\alpha_{yy}\alpha_{yz}\langle D_{33}^{4^*}\rangle
\end{aligned}
$$

$$V_5 = \frac{\pi^4 \alpha_{xx}^2 \langle D_{-4-3}^{4^*} \rangle}{32\sqrt{2}} + \frac{i\pi^4 \alpha_{xx}\alpha_{xy} \langle D_{-4-3}^{4^*} \rangle}{8\sqrt{2}} - \frac{\pi^4 \alpha_{xy}^2 \langle D_{-4-3}^{4^*} \rangle}{8\sqrt{2}} - \frac{\pi^4 \alpha_{xx}\alpha_{yy} \langle D_{-4-3}^{4^*} \rangle}{16\sqrt{2}}$$

$$- \frac{i\pi^4 \alpha_{xy}\alpha_{yy} \langle D_{-4-3}^{4^*} \rangle}{8\sqrt{2}} + \frac{\pi^4 \alpha_{yy}^2 \langle D_{-4-3}^{4^*} \rangle}{32\sqrt{2}} - \frac{1}{32}\sqrt{\frac{7}{2}}\pi^4 \alpha_{xx}^2 \langle D_{-4-1}^{4^*} \rangle$$

$$- \frac{1}{8} i \sqrt{\frac{7}{2}}\pi^4 \alpha_{xx}\alpha_{xy} \langle D_{-4-1}^{4^*} \rangle + \frac{1}{8}\sqrt{\frac{7}{2}}\pi^4 \alpha_{xy}^2 \langle D_{-4-1}^{4^*} \rangle$$

$$+ \frac{1}{16}\sqrt{\frac{7}{2}}\pi^4 \alpha_{xx}\alpha_{yy} \langle D_{-4-1}^{4^*} \rangle + \frac{1}{8} i \sqrt{\frac{7}{2}}\pi^4 \alpha_{xy}\alpha_{yy} \langle D_{-4-1}^{4^*} \rangle$$

$$- \frac{1}{32}\sqrt{\frac{7}{2}}\pi^4 \alpha_{yy}^2 \langle D_{-4-1}^{4^*} \rangle + \frac{1}{32}\sqrt{\frac{7}{2}}\pi^4 \alpha_{xx}^2 \langle D_{-41}^{4^*} \rangle + \quad \ldots$$

$$+ \frac{i\pi^4 \alpha_{xy}\alpha_{yy} \langle D_{23}^{4^*} \rangle}{8\sqrt{14}} + \frac{\pi^4 \alpha_{yy}^2 \langle D_{23}^{4^*} \rangle}{16\sqrt{14}} - \frac{i\pi^4 \alpha_{xz}\alpha_{yz} \langle D_{23}^{4^*} \rangle}{2\sqrt{14}} - \frac{\pi^4 \alpha_{yz}^2 \langle D_{23}^{4^*} \rangle}{4\sqrt{14}}$$

$$+ \frac{\pi^4 \alpha_{xx}\alpha_{zz} \langle D_{23}^{4^*} \rangle}{8\sqrt{14}} - \frac{i\pi^4 \alpha_{xy}\alpha_{zz} \langle D_{23}^{4^*} \rangle}{4\sqrt{14}} - \frac{\pi^4 \alpha_{yy}\alpha_{zz} \langle D_{23}^{4^*} \rangle}{8\sqrt{14}}$$

$$+ \frac{1}{16} i\pi^4 \alpha_{xx}\alpha_{xz} \langle D_{33}^{4^*} \rangle + \frac{1}{8}\pi^4 \alpha_{xy}\alpha_{xz} \langle D_{33}^{4^*} \rangle - \frac{1}{16} i\pi^4 \alpha_{xz}\alpha_{yy} \langle D_{33}^{4^*} \rangle$$

$$+ \frac{1}{16}\pi^4 \alpha_{xx}\alpha_{yz} \langle D_{33}^{4^*} \rangle - \frac{1}{8} i\pi^4 \alpha_{xy}\alpha_{yz} \langle D_{33}^{4^*} \rangle - \frac{1}{16}\pi^4 \alpha_{yy}\alpha_{yz} \langle D_{33}^{4^*} \rangle$$

$$V_6 = \frac{1}{15}\pi^4\alpha_{xx}^2\langle D_{00}^{0^*}\rangle + \frac{1}{5}\pi^4\alpha_{xy}^2\langle D_{00}^{0^*}\rangle + \frac{1}{5}\pi^4\alpha_{xz}^2\langle D_{00}^{0^*}\rangle - \frac{1}{15}\pi^4\alpha_{xx}\alpha_{yy}\langle D_{00}^{0^*}\rangle$$
$$+ \frac{1}{15}\pi^4\alpha_{yy}^2\langle D_{00}^{0^*}\rangle + \frac{1}{5}\pi^4\alpha_{yz}^2\langle D_{00}^{0^*}\rangle - \frac{1}{15}\pi^4\alpha_{xx}\alpha_{zz}\langle D_{00}^{0^*}\rangle$$
$$- \frac{1}{15}\pi^4\alpha_{yy}\alpha_{zz}\langle D_{00}^{0^*}\rangle + \frac{1}{15}\pi^4\alpha_{zz}^2\langle D_{00}^{0^*}\rangle - \frac{1}{28}\pi^4\alpha_{xx}^2\langle D_{-2-2}^{2^*}\rangle$$
$$- \frac{1}{14}i\pi^4\alpha_{xx}\alpha_{xy}\langle D_{-2-2}^{2^*}\rangle - \frac{3}{28}\pi^4\alpha_{xz}^2\langle D_{-2-2}^{2^*}\rangle - \frac{1}{14}i\pi^4\alpha_{xy}\alpha_{yy}\langle D_{-2-2}^{2^*}\rangle$$
$$+ \cdots + \frac{3\pi^4\alpha_{yy}\alpha_{yz}\langle D_{32}^{4^*}\rangle}{64\sqrt{14}} - \frac{i\pi^4\alpha_{xx}\alpha_{xz}\langle D_{34}^{4^*}\rangle}{32\sqrt{2}} - \frac{\pi^4\alpha_{xy}\alpha_{xz}\langle D_{34}^{4^*}\rangle}{16\sqrt{2}}$$
$$+ \frac{i\pi^4\alpha_{xz}\alpha_{yy}\langle D_{34}^{4^*}\rangle}{32\sqrt{2}} - \frac{\pi^4\alpha_{xx}\alpha_{yz}\langle D_{34}^{4^*}\rangle}{32\sqrt{2}} + \frac{i\pi^4\alpha_{xy}\alpha_{yz}\langle D_{34}^{4^*}\rangle}{16\sqrt{2}}$$
$$+ \frac{\pi^4\alpha_{yy}\alpha_{yz}\langle D_{34}^{4^*}\rangle}{32\sqrt{2}} + \frac{1}{128}\pi^4\alpha_{xx}^2\langle D_{44}^{4^*}\rangle - \frac{1}{32}i\pi^4\alpha_{xx}\alpha_{xy}\langle D_{44}^{4^*}\rangle$$
$$- \frac{1}{32}\pi^4\alpha_{xy}^2\langle D_{44}^{4^*}\rangle - \frac{1}{64}\pi^4\alpha_{xx}\alpha_{yy}\langle D_{44}^{4^*}\rangle + \frac{1}{32}i\pi^4\alpha_{xy}\alpha_{yy}\langle D_{44}^{4^*}\rangle$$
$$+ \frac{1}{128}\pi^4\alpha_{yy}^2\langle D_{44}^{4^*}\rangle$$

$$V_7 = -\frac{1}{128}\pi^4\alpha_{xx}^2\langle D_{-4-4}^{4^*}\rangle - \frac{1}{32}i\pi^4\alpha_{xx}\alpha_{xy}\langle D_{-4-4}^{4^*}\rangle + \frac{1}{32}\pi^4\alpha_{xy}^2\langle D_{-4-4}^{4^*}\rangle$$
$$+ \frac{1}{64}\pi^4\alpha_{xx}\alpha_{yy}\langle D_{-4-4}^{4^*}\rangle + \frac{1}{32}i\pi^4\alpha_{xy}\alpha_{yy}\langle D_{-4-4}^{4^*}\rangle - \frac{1}{128}\pi^4\alpha_{yy}^2\langle D_{-4-4}^{4^*}\rangle$$
$$+ \frac{1}{64}\sqrt{7}\pi^4\alpha_{xx}^2\langle D_{-4-2}^{4^*}\rangle + \frac{1}{16}i\sqrt{7}\pi^4\alpha_{xx}\alpha_{xy}\langle D_{-4-2}^{4^*}\rangle$$
$$- \frac{1}{16}\sqrt{7}\pi^4\alpha_{xy}^2\langle D_{-4-2}^{4^*}\rangle - \frac{1}{32}\sqrt{7}\pi^4\alpha_{xx}\alpha_{yy}\langle D_{-4-2}^{4^*}\rangle$$
$$- \frac{1}{16}i\sqrt{7}\pi^4\alpha_{xy}\alpha_{yy}\langle D_{-4-2}^{4^*}\rangle + \cdots + \frac{3}{64}\sqrt{\frac{7}{2}}\pi^4\alpha_{yy}\alpha_{yz}\langle D_{32}^{4^*}\rangle$$
$$+ \frac{i\pi^4\alpha_{xx}\alpha_{xz}\langle D_{34}^{4^*}\rangle}{32\sqrt{2}} + \frac{\pi^4\alpha_{xy}\alpha_{xz}\langle D_{34}^{4^*}\rangle}{16\sqrt{2}} - \frac{i\pi^4\alpha_{xz}\alpha_{yy}\langle D_{34}^{4^*}\rangle}{32\sqrt{2}}$$
$$+ \frac{\pi^4\alpha_{xx}\alpha_{yz}\langle D_{34}^{4^*}\rangle}{32\sqrt{2}} - \frac{i\pi^4\alpha_{xy}\alpha_{yz}\langle D_{34}^{4^*}\rangle}{16\sqrt{2}} - \frac{\pi^4\alpha_{yy}\alpha_{yz}\langle D_{34}^{4^*}\rangle}{32\sqrt{2}}$$
$$- \frac{1}{128}\pi^4\alpha_{xx}^2\langle D_{44}^{4^*}\rangle + \frac{1}{32}i\pi^4\alpha_{xx}\alpha_{xy}\langle D_{44}^{4^*}\rangle + \frac{1}{32}\pi^4\alpha_{xy}^2\langle D_{44}^{4^*}\rangle$$
$$+ \frac{1}{64}\pi^4\alpha_{xx}\alpha_{yy}\langle D_{44}^{4^*}\rangle - \frac{1}{32}i\pi^4\alpha_{xy}\alpha_{yy}\langle D_{44}^{4^*}\rangle - \frac{1}{128}\pi^4\alpha_{yy}^2\langle D_{44}^{4^*}\rangle$$

$$V_8 = -\frac{\pi^4\alpha_{xx}^2\langle D_{-4-3}^{4^*}\rangle}{32\sqrt{2}} - \frac{i\pi^4\alpha_{xx}\alpha_{xy}\langle D_{-4-3}^{4^*}\rangle}{8\sqrt{2}} + \frac{\pi^4\alpha_{xy}^2\langle D_{-4-3}^{4^*}\rangle}{8\sqrt{2}} + \frac{\pi^4\alpha_{xx}\alpha_{yy}\langle D_{-4-3}^{4^*}\rangle}{16\sqrt{2}}$$
$$+ \frac{i\pi^4\alpha_{xy}\alpha_{yy}\langle D_{-4-3}^{4^*}\rangle}{8\sqrt{2}} - \frac{\pi^4\alpha_{yy}^2\langle D_{-4-3}^{4^*}\rangle}{32\sqrt{2}} + \frac{1}{32}\sqrt{\frac{7}{2}}\pi^4\alpha_{xx}^2\langle D_{-4-1}^{4^*}\rangle$$
$$+ \frac{1}{8}i\sqrt{\frac{7}{2}}\pi^4\alpha_{xx}\alpha_{xy}\langle D_{-4-1}^{4^*}\rangle - \frac{1}{8}\sqrt{\frac{7}{2}}\pi^4\alpha_{xy}^2\langle D_{-4-1}^{4^*}\rangle$$
$$- \frac{1}{16}\sqrt{\frac{7}{2}}\pi^4\alpha_{xx}\alpha_{yy}\langle D_{-4-1}^{4^*}\rangle - \frac{1}{8}i\sqrt{\frac{7}{2}}\pi^4\alpha_{xy}\alpha_{yy}\langle D_{-4-1}^{4^*}\rangle + \cdots$$
$$+ \frac{i\pi^4\alpha_{xz}\alpha_{yz}\langle D_{23}^{4^*}\rangle}{2\sqrt{14}} + \frac{\pi^4\alpha_{yz}^2\langle D_{23}^{4^*}\rangle}{4\sqrt{14}} - \frac{\pi^4\alpha_{xx}\alpha_{zz}\langle D_{23}^{4^*}\rangle}{8\sqrt{14}} + \frac{i\pi^4\alpha_{xy}\alpha_{zz}\langle D_{23}^{4^*}\rangle}{4\sqrt{14}}$$
$$+ \frac{\pi^4\alpha_{yy}\alpha_{zz}\langle D_{23}^{4^*}\rangle}{8\sqrt{14}} - \frac{1}{16}i\pi^4\alpha_{xx}\alpha_{xz}\langle D_{33}^{4^*}\rangle - \frac{1}{8}\pi^4\alpha_{xy}\alpha_{xz}\langle D_{33}^{4^*}\rangle$$
$$+ \frac{1}{16}i\pi^4\alpha_{xz}\alpha_{yy}\langle D_{33}^{4^*}\rangle - \frac{1}{16}\pi^4\alpha_{xx}\alpha_{yz}\langle D_{33}^{4^*}\rangle + \frac{1}{8}i\pi^4\alpha_{xy}\alpha_{yz}\langle D_{33}^{4^*}\rangle$$
$$+ \frac{1}{16}\pi^4\alpha_{yy}\alpha_{yz}\langle D_{33}^{4^*}\rangle$$

Chapter 3

Space Selective Reduction of Europium Ions via SrF_2 Crystals Induced by Femtosecond Laser

3.1 Introduction

Direct micro-structuring inside glass materials with near-infrared femtosecond laser has been an attractive research topic recently [1, 2]. The energy is compressed in ultrashort time scale so that the strength of the electric field can reach as much of 100TW/cm^2 depending on focusing condition, which is sufficient to cause non-linear optical process including multiphoton absorption, tunnelling ionization and avalanche ionization inside transparent materials at non-resonant wavelength. Therefore the femtosecond laser was used in manufacturing integrated optics such as waveguide and optical data storages [3, 4].

The reduction of europium ions inside glass by femtosecond laser has been previously reported [5, 6], however, these results are highly depended on the glass composition of glass. To our best knowledge, the photon reduction of Eu^{3+} inside glass are only reported in fluoride and borate glasses with 1KHz femtosecond laser, which limited the selection of glass host. Recently, reduction of Eu^{3+} inside glass ceramic containing SrF_2 was described [7]. In this work, we present the reduction of Eu ions with SrF_2 crystals which is induced by 250 KHz femtosecond laser inside oxyfluoride glass.

3.2 Experiments

The glass samples were prepared by traditional melting-quench method. The composition of glass samples is listed in Table 3.1. Appropriate raw materials (SiO_2, Al_2O_3, NaF, SrF_2, EuF_3, LaF_3) was mixed and put in a covered Al_2O_3 crucible in normal atmosphere, then the crucible is heated up to 1430 °C for 45 min. the melt was poured on a brass mold and then pressed by another brass plate. All of these glass samples were cut and polished for laser experiment. A regenerative amplified 800 nm Ti: sapphire laser (RegA 9000, Coherent Inc.) was used which emitted 70 fs, 250 KHz mode-lock pulses with wavelength of 800 nm to irradiate the glass sample. During the experiment laser beam was focused 100 μm below the glass surface via a 20× objective lens (NA=0.45).

The method to measure the luminescent spectra of modified region was to use a fiber detector under excitation with the abovementioned pulse laser. The X-Ray diffraction (XRD) measurement was performed by using Cu Kα radiation (Rigaku RINT-2500HF diffractometer) to identify the crystalline phase. It is difficult to obtain the XRD pattern for single irradiated spot (tens of micrometer), so laser-modified line arrays were created by translate the glass in the vertical direction of propagation direction of laser, then the sample was polished until the line arrays reached the glass surface. The polished sample was used for XRD measurement.

Glass	SiO_2	Al_2O_3	NaF	EuF_3	SrF_2	LaF_3
ESG	50	22	6	2	20	-
SG	50	22	6	-	20	-
ELG	50	22	6	2	-	20

Table 3.1 composition of glass sample

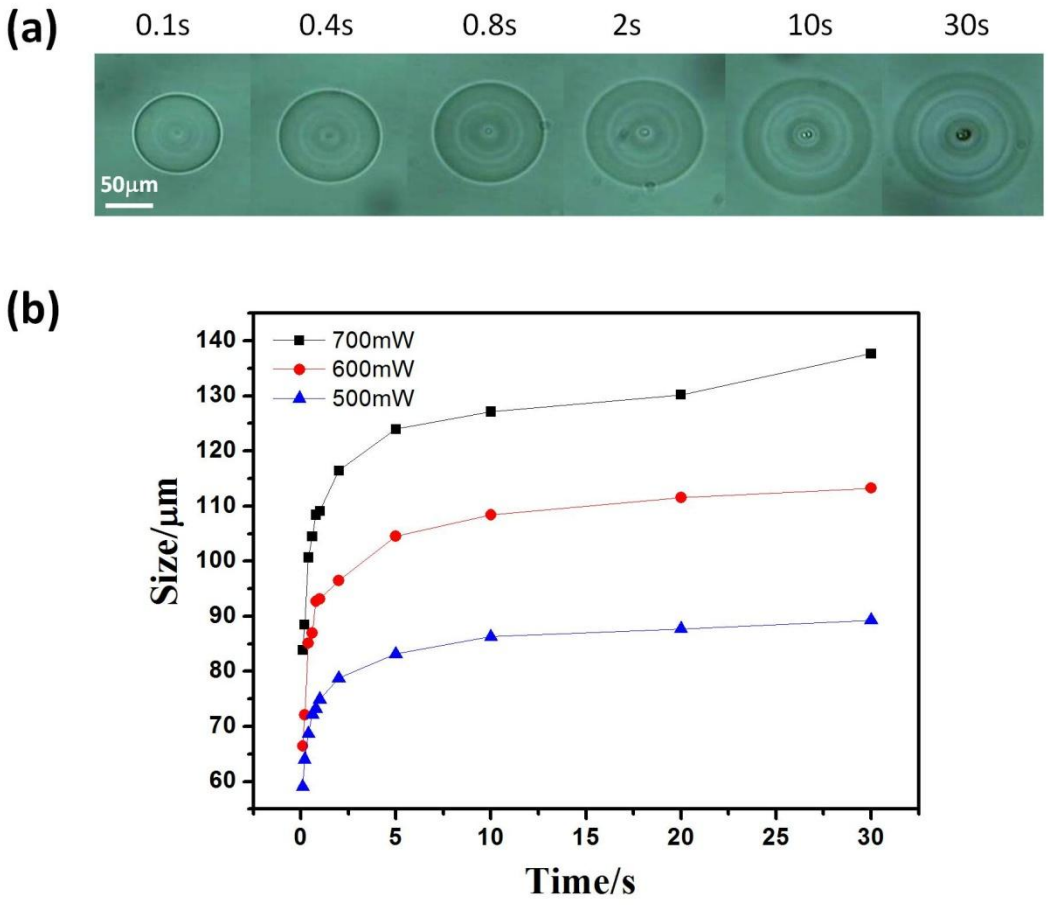

Fig. 3.1 (a) Optical microscopic image of the microstructures induced with static exposure of femtosecond laser pulse with different objective lens for various times. (b)Dependence of the diameter of the laser induced zone on the irradiation time.

3.3 Results and Discussion

The top view of the structure induced by laser is shown in Fig. 3.1(a) and the concentric-ring-shaped structure is observed, which is much larger than the laser focal spot size due to the thermal expansion. The outer structure is due to strain generated by the residue thermal stress after femtosecond laser irradiation [1]. We also found the centre of focal spot becomes black when exposure time exceeds 30s, small bubbles ascribed to the micro explosion should be responsible for this observation [8]. Fig. 3.1(b) shows the time-depend size variation of the structure induced by femtosecond laser with deferent power. The size of modified structure increases dramatically during the first 2s of time, but the speed of growth slows down and approaches saturation because the heat fluctuation reached balance.

Fig. 3.2 presents the X-ray diffraction patterns of ESG glass and laser-modified region. The as-made glass has no diffraction peaks, but two peaks are observed in the pattern for the laser-modified area. For comparison the XRD pattern of ESG glass heat treated at 580℃ for 30min is also presented in Fig. 3.2. According to JCPDS standard card these two peaks belong to SrF_2 crystal, and no second phase of crystalline was found. When irradiated by high repetition rate femtosecond laser, heat accumulation occurred at the focal spot. The thermal effect could cause the nucleation and crystal growth near the laser focal spot [9], SrF_2 could be space-selectively precipitated inside glass with femtosecond laser irradiation.

In Fig. 3.3 the luminescence spectra is presented. Although femtosecond pulse laser is used as the excitation source, the laser beam was attenuated to 0.08 μJ so the multi-phonton absorption process was only enough to excite luminescence of rare earth ions and the structure of modified region is not compromised during the

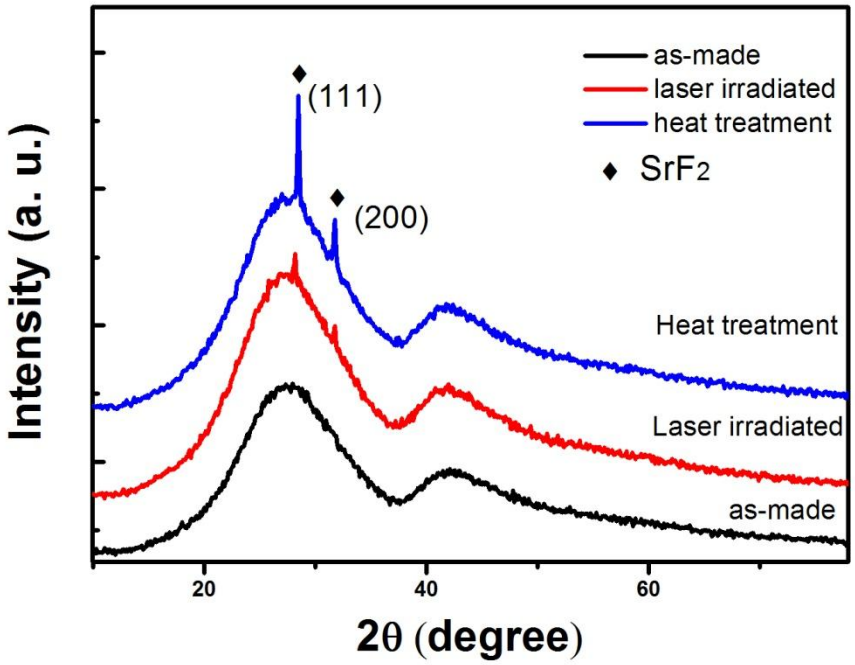

Fig. 3.2 XRD patterns for the glass modified region, glass and glass ceramics.

measurement [2]. The emission peaks from 560 nm to 710 nm could be attributed to the $^5D_0$ energy level to ^7F_J (J=0, 1, 2, 3, 4) levels of Eu^{3+} and the broad band emission peaked at around 470 nm is regarded to the $4f^65d$ to $4f^7$ transition of Eu^{2+}. The luminescence of non-irradiated area shows only the Eu^{3+} emission, indicating that the concentration of Eu^{2+} in as-made glass is negligible. A strong emission of Eu^{2+} is observed at the center of focal spot, suggesting the reduction from Eu^{3+} to Eu^{2+} was realized inside ESG glass under femtosecond laser irradiation. We also investigated the luminescent property in the SG and ELG glass before and after laser irradiation. In SG glass no emission from Eu ions is observed, except a weak emission at 400 nm which is ascribed to the nonlinear effect of femtosecond laser. In SLG glass only the Eu^{3+} emission is observed, suggesting Eu ions are usually unable to be reduced in oxyfluoride glass. The precipitation of SrF_2 crystal is responsible for the reduction process which we observed in the ESG sample.

The mechanism of this photo reduction is not based on the active electron from glass host trapped by Eu^{3+} ions which is proposed in the earlier work [5, 6]. During high repetition rate laser irradiation, heat was accumulated at the focal spot due to multi-photon absorption and plasma with high temperature is induced. The extremely high temperature at the focal spot formed temperature gradient [10] which induced the nucleation and growth of SrF_2 crystal. In such condition, Eu^{3+} from the glass host would be inevitably doped into SrF_2 crystalline. During this “doping” process, two Eu^{3+} would substituted for three Sr^{2+} ions, and a cation vacancy defect with two negative charges would be created. The vacancy acted as a donor of electron and transferred electrons to Eu^{3+} in the crystal host under thermal stimulation, reducing Eu^{3+} to Eu^{2+} [7]. Besides, compare with the size of Eu^{3+} (96.4 pm), the size of Eu^{2+}

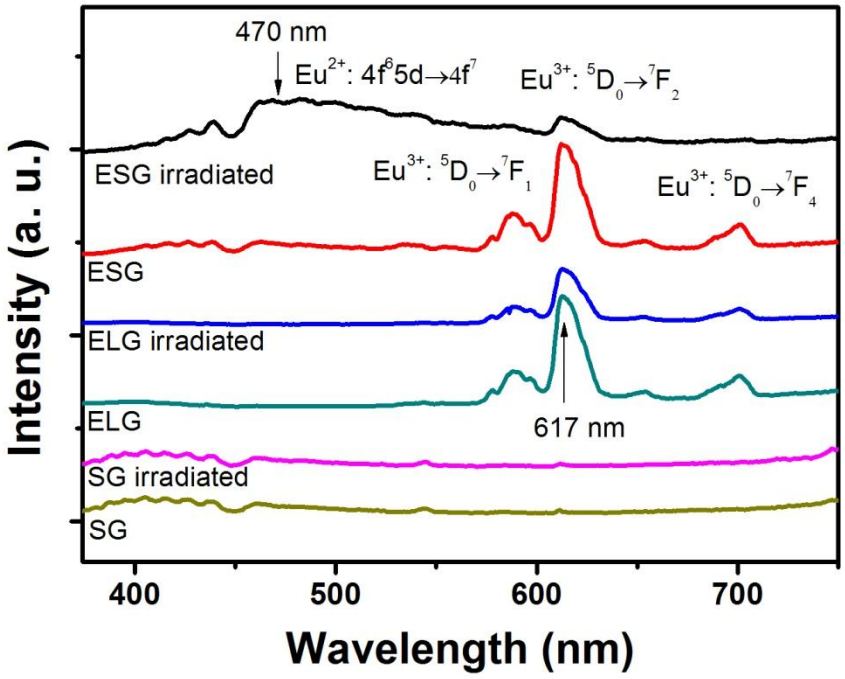

Fig.3.3 Emission spectra before and after laser irradiation for ESG, ELG and SG.

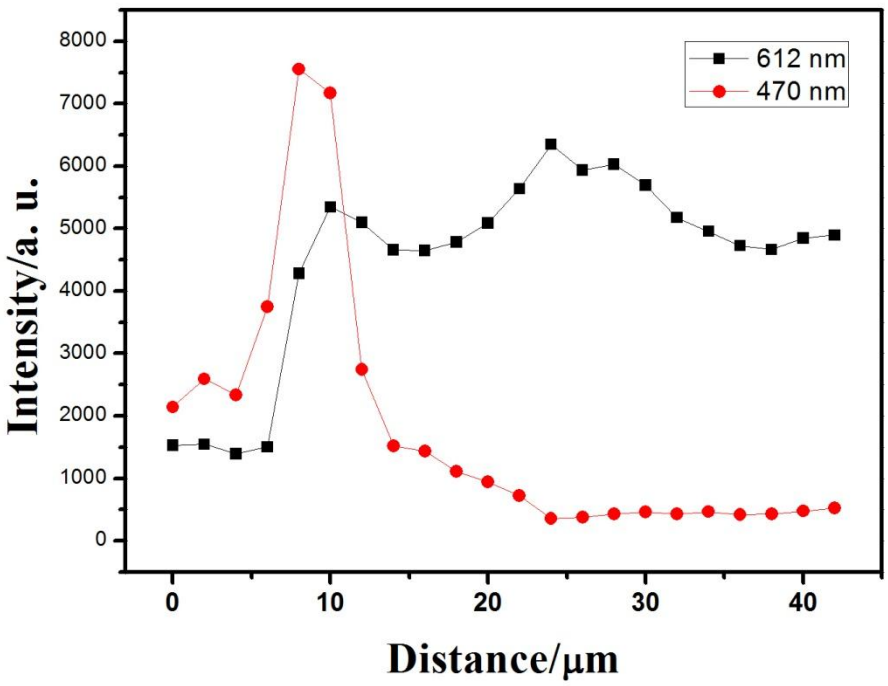

Fig. 3.4 Variation of peak intensity as the function of the distance to the center of laser modified spot, which induced by irradiation of femtosecond laser with 700 mW for 30s. During the luminescence measurement, the excited area was about 2 μm in diameter.

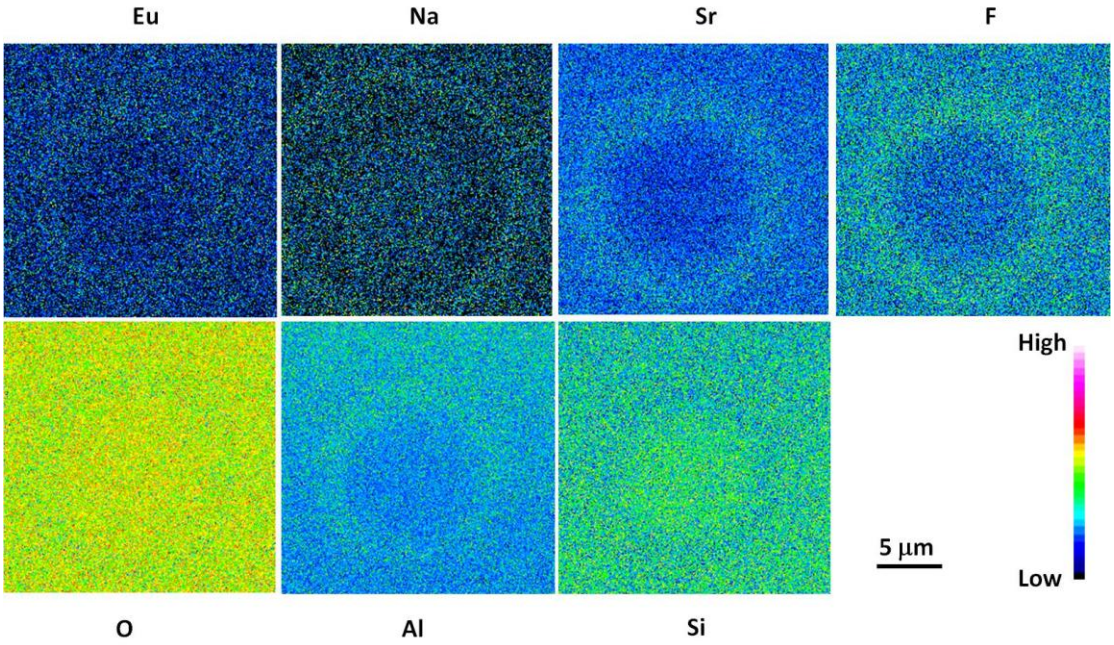

Fig. 3.5 The EPMA mapping showing only the relative concentration changes of the different ions in the glass around the focal point after the femtosecond laser irradiation.

(109 pm) is much closer to the size of Sr^{2+} (113 pm), so the reduction of Eu ions is favored because it could reduce the lattice distortion of doped SrF_2 crystal.

Fig. 3.4 shows the intensities of the emissions associated with Eu^{2+} (470 nm) and Eu^{3+} (612 nm) as the function of the distance from the center of laser modified region. Eu^{2+} emission is weak at around the center but the intensity increases dramatically as the distance increases from 6 μm to 10 μm. The intense luminescence from Eu^{2+} indicates that the SrF_2 is mainly precipitated at this region since reduction could not occur without SrF_2.

Fig. 3.4 also shows that the emission from Eu^{3+} increases at the region where SrF_2 precipitated. This variation is related to the elemental redistribution induced by the laser irradiation. The glass network modifier tends to migrate to the outer region and network former has the tendency to be enriched at the center during high repetition femtosecond laser irradiation [11]. Although the SrF_2 reduced a fraction of Eu^{3+} to Eu^{2+}, the luminescence at 612 nm is still increased due to the total concentration of Eu ions is increased at this region.

The composition variation of ESG due to femtosecond laser irradiation is also measured with EPMA, as is shown in Fig. 3.5. The enrichment of Sr and F at the ring-shaped region is accordant with our above deduction where the SrF_2 is mainly precipitated. In addition, the mapping of Eu shows the concentration increase in the same region.

In Fig. 3.4, when the distance is larger than 10 μm, the emission at 470 nm is keeping decreasing until no luminescence from Eu^{2+} could be observed. There are two reasons for this phenomenon. The first one is the element redistribution region is only in a short distance from the center, the concentration of Eu would be decreased to

reach the initial glass composition as distance is further increased. The other reason is the temperature decreases rapidly along radical direction from the focal spot when femtosecond laser is irradiating [10], so the nucleation and growth of SrF_2 crystal decreased and could not occur at the region where the temperature is too low. Assuming doping concentration is proportional to the volume fraction of SrF_2, the reduction of Eu^{3+} to Eu^{2+} decreased as less SrF_2 was precipitated. The Eu^{2+} emission could be observed until the distance increased to 22 μm. When the distance is further than 22 μm the reduction of Eu ions could not be observed because of the absence of SrF_2 crystallization.

3.4 Conclusions

In summary, we have successfully realized the reduction of Eu^{3+} to Eu^{2+} in a oxyfluoride glass with high repetition rate femtosecond laser. The precipitation of SrF_2 is observed in the laser modified region and works as a new type of photo-reduction mechanism of ultra short pulse laser. These results may extend application of Eu-doped glass in the 3D optical data storages.

3.5 References:

[1] M. Sakakura, M. Shimizu, Y. Shimotsuma, K. Miura, and K. Hirao, Appl. Phys. Lett. **93** (2008) 231112.

[2] S. Zhou, N. Jiang, K. Miura, S. Tanabe, M. Shimizu, M. Sakakura, Y. Shimotsuma, M. Nishi, J. Qiu, and K. Hirao, J. Am. Chem. Soc. **132** (2010) 17945.

[3] L. Canioni, M. Bellec, A. Royon, B. Bousquet, and T. Cardinal, Opt. Lett. **33** (2008) 360.

[4] K. Miura, J. Qiu, H. Inouye, T. Mitsuyu and K. Hirao, Appl. Phys. Lett. **71** (1997) 3329.

[5] J. Qiu, K. Kojima, K. Miura, T. Mitsuyu, and K. Hirao, Opt. Lett. **24** (1999) 786

[6] K. Lim , S. Lee, M. Trinh, S. Kim, M. Lee, D. S. Hamilton, and G. N. Gibson, J. Lumin. **122-123** (2007) 14.

[7] Q. Luo, X. Qiao, X. Fan, S. Liu, and X. Zhang, J. Non-Cryst. Solids **354** (2008) 4691.

[8] E. N. Glezer, and E. Mazur, Appl. Phys. Lett. **71**, 882-884 (1997)

[9] Y. Yonesaki, K. Miura, R. Araki, K. Fujita, and K. Hirao, J. Non-Cryst. Solids **351** (2005) 885.

[10] M. Sakakura, M. Shimizu, Y. Shimotsuma, K. Miura, and K. Hirao, Appl. Phys. Lett. **93** (2008) 231112.

[11] Y. Liu, M. Shimizu, B. Zhu, Y. Dai, B. Qian, J. Qiu, Y. Shimotsuma, K. Miura, and K. Hirao, Opt. Lett. **34** (2009) 136.

Chapter 4

Infrared luminescence and optical amplification of bismuth-doped borate and borosilicate glasses

4.1 Introduction

The rapid development of information society requires the continuous improvement of data transportation capacity of optical communication Internet. It is an attractive way to increase the transferring capacity by increasing the channel number of the system. Since the channel number is determined by the gain bandwidth of fiber amplifier, the wider the gain bandwidth, the more the channel number. Considerable efforts have been devoted to the achievement of broadband amplification by choosing rare-earth (e.g. Pr^{3+}, Tm^{3+} or Er^{3+}) doped fiber amplifiers (REDFA). Unfortunately, the application bandwidths of REDFAs are hardly beyond 100nm because the f-f transitions of rare earth ions are confined in the inner-shell, which are insensitive to local environmental. Fiber Raman amplifiers can overcome these drawbacks and realize the broadband amplification. However, they require multi-wavelength pumping schemes, high-power consumption and more complicated structures. In the current status of Wavelength-division multiplexing (WDM) system, there are some optical telecommunication waveband in the range of 1.2~1.6 μm which optical amplification cannot be realized by REDFAs. If optical amplification can be realized by a single broadband fiber amplifier in all optical telecommunication waveband from 1.2μm to 1.6μm, a new revolution can no doubt be anticipated in the future data transportation system. In order to fabricate the new super-broadband optical amplification devices, it is essential to explore the luminescence materials

especially covering 1.2~1.6μm region.

With some certain excitation, bismuth-doped glasses show ultra-broadband luminescence covering 1000~1700nm wavelength region. The full width at half maximum of this infrared luminescence is over 200nm and the fluorescence lifetime is about hundred microseconds. These properties indicate that bismuth-doped glasses may be a promising optical amplification gain medium. In this chapter, we synthesize a sort of Bi-doped borate and borosilicate glasses and the corresponding infrared luminescence is studied. Upon the excitation of 808nm laser diode, the bismuth activated glass samples can emit the fluorescence peaking at 1300nm with both broadband and long lifetime feature.

4.2 Infrared Broadband Emission of Bismuth-Doped RO-B2O3(R=Ca, Sr, Ba) Glasses

4.2.1 Experiments

All glass samples were first synthesized using a conventional melting-quenching method. Analytic-purity reagents H_3BO_3, Bi_2O_3, $CaCO_3$, $BaCO_3$ and $SrCO_3$ were used as raw materials. The glass composition is listed in Table 4.1. BGSr2 and BGBa2 were prepared in covered carbon crucibles. Samples without Bi doped are also synthesized. The mixtures of raw materials according to the desired compositions were melted at 1300 ℃ for 30 minutes in Pt crucibles in air, and then cast onto a stainless plate, and naturally cooled down to room temperature. For comparison, we prepared 30SrO-70B_2O_3-1Bi_2O_3 (BGSr2), 30BaO-70B_2O_3-1Bi_2O_3 (BGBa2) glasses in covered carbon crucibles and Crystals containing Bi temperature were synthesized at high transparent and confirmed by X-ray diffraction.

Optical absorption spectra of the glass samples were recorded using a JASCO FP6500 spectrophotometer and infrared fluorescence spectra were acquired using a HORIBA TRIX-550 spectrophotometer an 800nm semiconductor laser diode was used as an excitation source. All the measurements were carried out at room temperature.

Glass	B_2O_3	Bi_2O_3	CaO	SrO	BaO
BGCa1	70	1	30	-	-
BGCa2	70	1	35	-	-
BGSr1	70	1	-	30	-
BGBa1	70	1	-	-	30
BGSr2	70	1	-	30	-
BGBa2	70	1	-	-	30

Table 4.1 the composition of glass samples

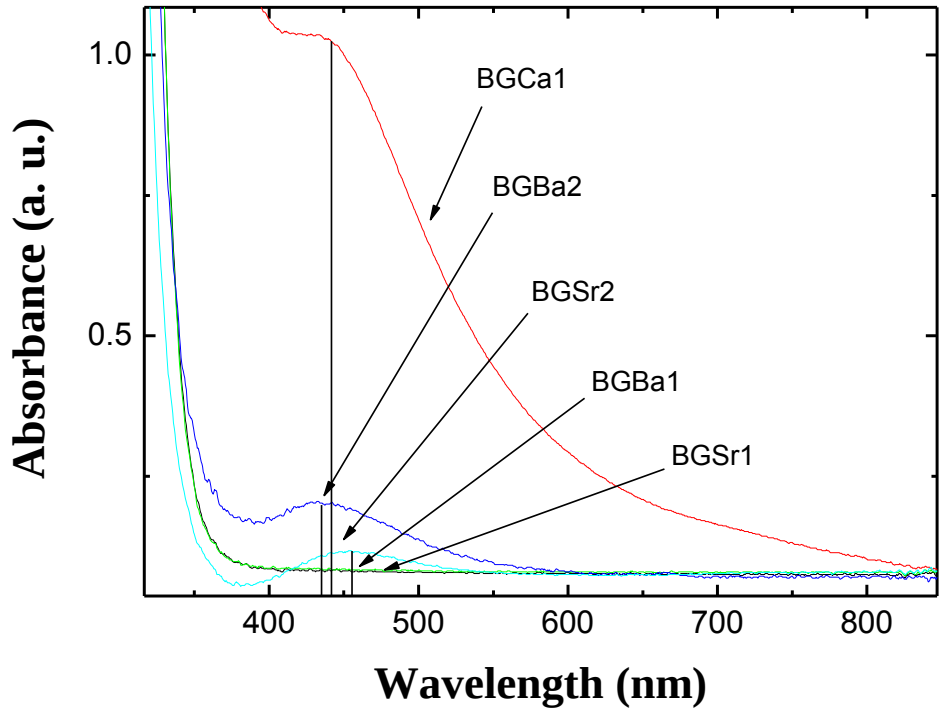

Fig. 4.1 Absorption spectra of Bi-doped 30RO-70B_2O_3 (R=Ca, Sr, Ba) glasses

4.2.2 Results and discussion

Figure 4.1 shows the absorption spectra of glass samples. In the absorption spectra, BGSr1 and BGBa1 does not show any absorption in the range from 400 to 800nm, BGSr2, BGBa2 and BGCa1 glasses show an asymmetry broadband, peaking at ～450 nm. We also noted that these broadband absorptions are similar to the Bi-doped silicate glasses [1]. We confirmed that samples without Bi did not show absorption at 450 nm even melted in carbon crucibles. Therefore, the absorption in BGCa1, BGSr2, BGBa2 glasses is likely related to low-valence Bi.

Figure 4.2 shows absorption spectra of crystals containing Bi with different valance state. No absorption peak at ~450 nm was observed in Bi^{3+}- and Bi^{5+}-containing glasses, while an absorption peak observed at 450 nm in the Bi^{2+}-doped crystals. Therefore absorption peak at 450 nm can be assigned to Bi^{2+}.

Figure 4.3 shows the near infrared emission spectra of BGCa1, BGSr1, BGSr2, BGBa1 and BGBa2 glasses excited by 0.8μm LD. BGSr1, BGBa1 glasses does not show any emissions in the range of 1000-1500 nm. However, near infrared emissions at 1300nm are observed in the BGCa1, BGSr2 and BGBa2 glasses at room temperature even no apparent absorption is detected at 800nm for BGSr2 and BGBa2 glasses. These emissions show broadband characteristics. Apparently glass basicity has an obvious effect on infrared luminescence properties, the intensity of emission decrease as glass basicity increases (Ba>Sr>Ca). Slight variation of absorption peak positions in samples indicates that the luminescent properties of bismuth-doped glasses depend on the glasses composition. Compositional changes may affect the environment around Bi.

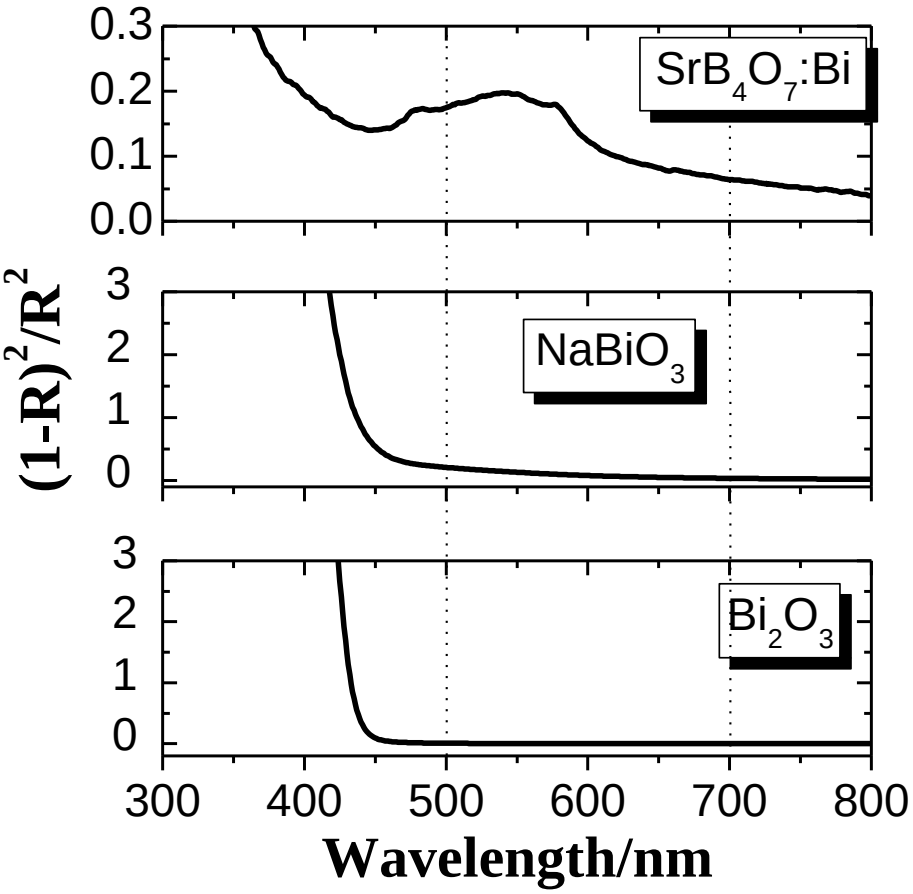

Fig. 4.2 Absorption spectra of various crystals containing Bi

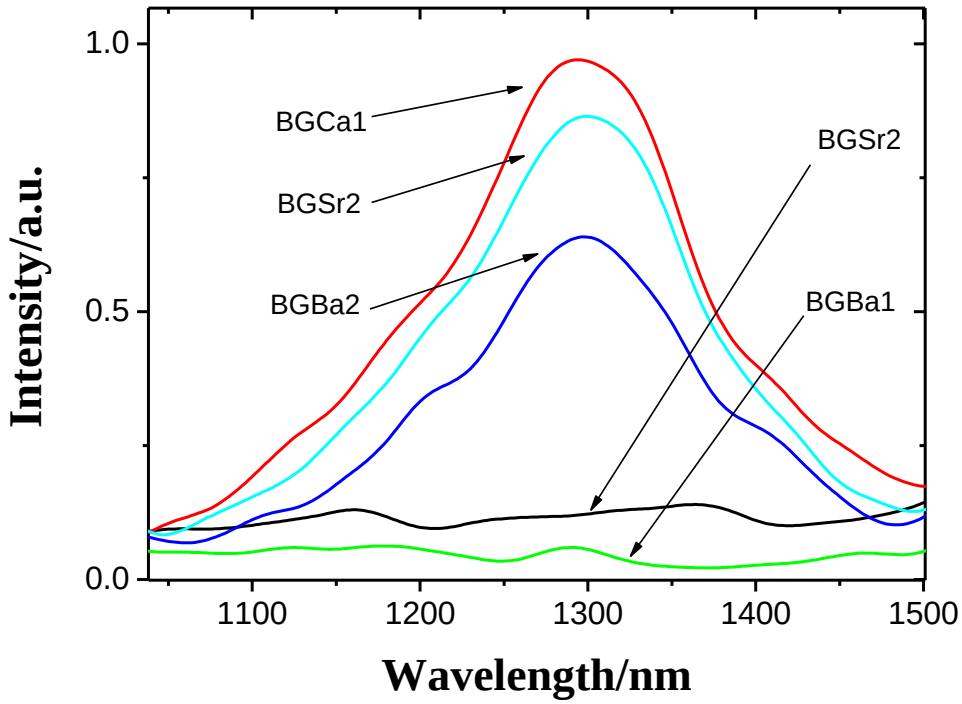

Fig. 4.3 Near-infrared emission spectra of BGCa1, BGSr1, BGSr2, BGBa1 and BGBa2 glasses excited by 800nm LD

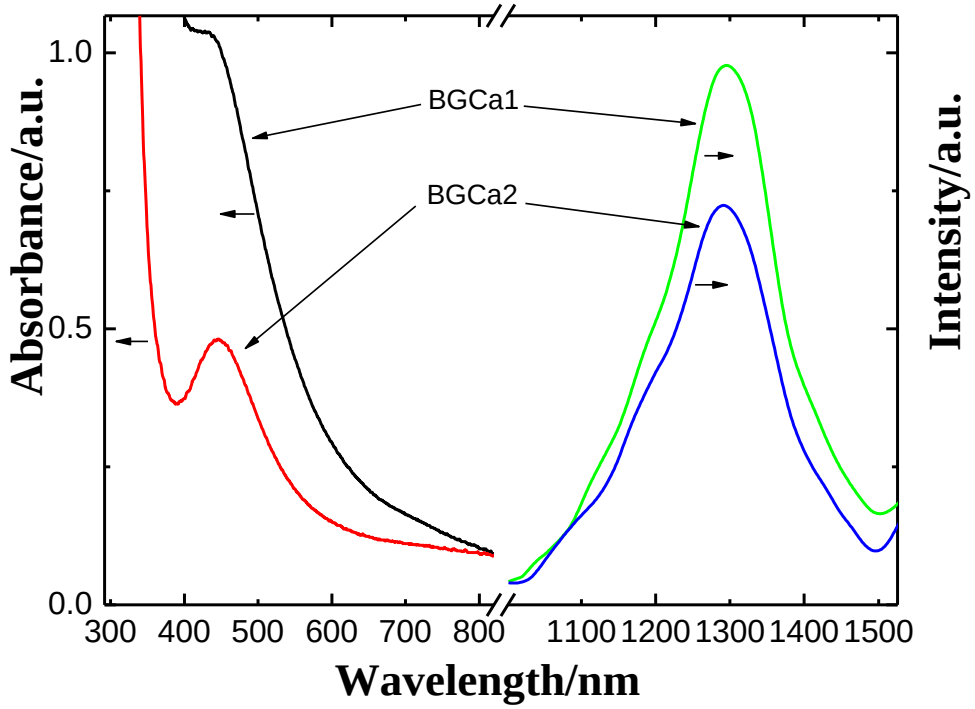

Fig. 4.4 Absorption spectra and the corresponding near-infrared emission spectra of BGCa1 and BGCa2 glasses

Figure 4.4 shows the absorption spectra and near-infrared emission spectra of BGCa1 and BGCa2 glasses. There is a consistence between the absorption at 450 nm and emission at 1300nm.

Fujimoto et al ascribed the infrared emission spectra of Bi and Al ions co-doping silicate glasses to the Bi^{5+} transitions between the ground state of $^1S_0$ and the excited state of $^3D_{3,2,1}$ and $^1D_2$ [1]. However, our works indicate clearly that the near-infrared emission should be initiated from lower-valence bismuth ions rather than higher-valence ions. Based on the glass basicity theory proposed by Ingram and Duffy [2, 3], increasing glass basicity favors the formation of high valence bismuth. In our observation it is accompanied with the decrease the intensity of infrared emission or even result in disappearance of infrared emission. Therefore, we suggest that the infrared emission is originated from low valence bismuth. V. V. Dvoyrin et al. calculated the electronic configurations of Bi^+ and Bi^{5+} ions [4], according to their results, both of the Bi^+ and Bi^{5+} ions may have possibilities for near-infrared emission. According to our results, we suggest that the near infrared luminescence in GBCa1, GBCa2, GBSr2, GBBa2 glasses originated from Bi^+ rather than Bi^{5+}. Lower basicity of glass matrix and reducing atmosphere favor the formation of low valance state Bi ions, e.g. Bi^{2+}, Bi^+. So the near infrared luminescence should originate from at least one of them.

4.3 Abnormal Luminescence Behavior in Bi-Doped Borosilicate Glasses

4.3.1 Experiments

The glass samples were prepared by the conventional melting and quenching method. Analytical reagents Na_2CO_3, H_3BO_3, SiO_2 and Bi_2O_3 were used as raw materials. Approximately 25g batches corresponding to the glass compositions (in mol%) of xB_2O_3-(30-x)Na_2O-69SiO_2-Bi_2O_3(x=5, 10, 13, 15, 16.5, 20, 23, 25 named as Gn (n=1 to 8) respectively, were mixed homogenously in an agate mortar, melted in a corundum crucible. Melting was carried out at 1520 ℃ for 45 minutes under abmient atmosphere. The melt was then cast into a slab on a heated iron plate. The samples were cut into the size of 10×10×1.6 mm^3 and polished for optical measurements.

The luminescence spectra and the fluorescence decay curves in both visible and NIR regions were recorded using an FLS920 fluorescence spectrophotometer (Edinburgh Instrument Ltd., U.K.). All of the measurements were carried out at room temperature.

Sample	B_2O_3 mol%	Λ	N_4^*	$[BO_4]$mol%
G1	5	0.5918	1.000	10.00
G2	10	0.5730	0.897	17.94
G3	13	0.5609	0.813	21.14
G4	15	0.5533	0.778	23.34
G5	16.5	0.5479	0.759	25.04
G6	20	0.5261	0.500	20.00
G7	23	0.5069	0.304	13.98
G8	25	0.4946	0.200	10.00

N_4^* are calculated by Bray model.

Table 4.1 Value of optical basicity (Λ), fraction of B four-coordinated with O (N_4), and $[BO_4]$mol% for each glass composition

4.3.2 Results and discussion

Figures 4.5a), b) and c) show the excitation and emission spectra of samples G1, G5 and G8, respectively. A blue emission was observed around 420 nm in sample G1 when excited at 312 nm. It can be attributed to the transition of Bi^{3+} [5-8]. The blue emission at 420 nm was also observed in sample G5 together with an emission centered at 618 nm due to transition of Bi^{2+} when excited at 468 nm [9, 10]. In contrast, only emission at 618 was detected in sample G8 while no blue emission at 420 nm was observed.

The visible luminescence spectra of Bi doped glasses with different x value are shown in Fig. 4.6 (a) and (b). With 312 nm excitation, the samples shows intense blue luminescence centered at 420 nm. By comparing the luminescence spectra of glasses with different Na_2O concentration, we clearly observed that the emission intensity at 420 nm decreases with decreasing Na_2O concentration (or increasing with B_2O_3 concentration). This maybe due to the change in optical basicity of glasses since the lower optical basicity favors the formation of lower valence state for the multivalencent metal ions [2, 3]. The theoretical optical basicity (Λ_{th}) for the glass system under study was calculated using the Eq. 4.1:

$$\Lambda_{th} = X_1\Lambda_1 + X_2\Lambda_2 + X_3\Lambda_3 + ... + X_n\Lambda_n \qquad (4.1)$$

where Λ_n is the optical basicity quantity of one composition of glass, and X_n is the molar percent of the components studied. The optical basicity values Λ_n are from Ref. [11]. The values of Λ_{th} with different Na_2O concentration are shown in Table 1. Fig. 4.7 shows the relationship between the emission intensity at 420 nm and the optical basicity of the glasses. The decrease in Λ_{th} value agrees well with decraese in emission intensity at 420 nm from sample G1 to G8. This result indicates that much more Bi^{3+}

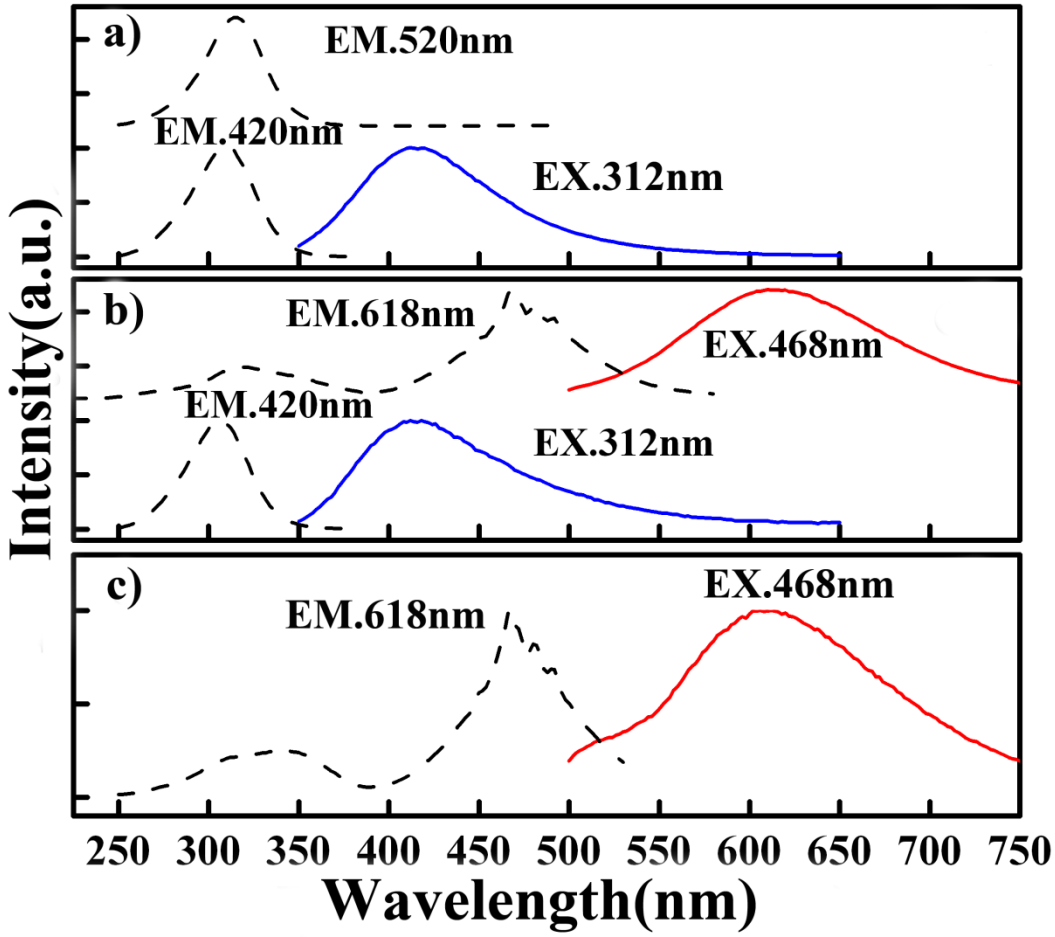

Fig. 4.5 Excitation and emission spectra of a) G1, b) G5, and c) G8 in the visible region. The solid lines in (a–c) are the emission and the dashed lines are the excitation spectra

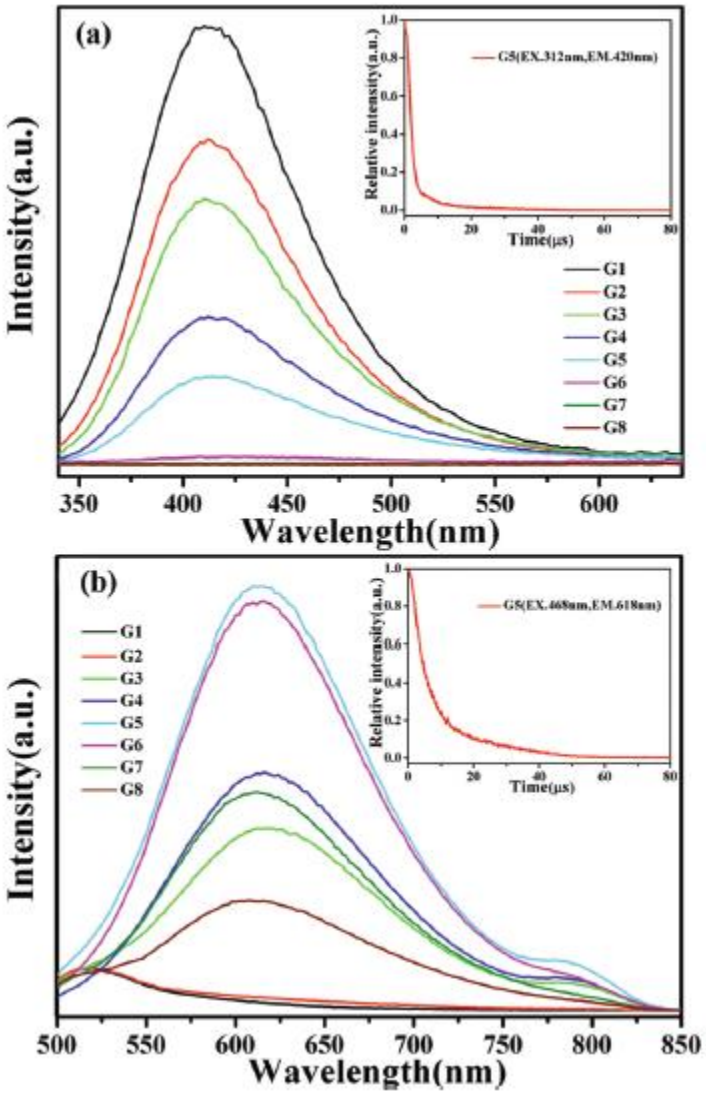

Fig. 4.6 Emission spectra of the samples a) 312 nm excited , the inset shows the fluorescence decay curves of sample G5 (monitoring wavelength is 420 nm). b) 468 nm excited, the inset shows the fluorescence decay curves of sample G5 (monitoring wavelength is 618 nm)

ions transfer to lower valence bismuth ions (such as Bi^{2+}, Bi^{+}) in the glasses with decreasing Na_2O concentration.

Fig. 4.6 (b) presents the luminescence spectra of xB_2O_3-(30-x)Na_2O-69SiO_2-Bi_2O_3 (x =5, 10, 13, 15, 16.5, 20, 23, 25 in mol%) when excited at 468nm. In sample G1 and G2, we only observed a weak band at 520 nm, which is from $^3P_1 \rightarrow {}^1S_0$ transition of Bi^{3+}. With the decrease of Na_2O concentration, a new emission band at 618nm emerged in the emission spectra of the samples G3 to G8. Different from the blue emission band at 420 nm which come from Bi^{3+}, the red emission intensity increases with decrease of the Na_2O concentration at first when x<16.5, and then decreases with further decrease of Na_2O concentration. There is a maximum of the luminescence intensity for the sample G5. In Fig. 2(b), we also observed a weak emission band at 780 nm, which has been reported in many silicate glasses [12]. The dependence of the 618 nm emission intensity on optical basicity of the glass samples are also shown in Fig. 4.7. We also performed fluorescence decay measurements for samples G5, and the results are shown in the insets of Fig. 4.6. The monitoring wavelengths were 420 and 618 nm, and the corresponding excitation wavelengths were 312 and 468 nm, respectively. The estimated lifetimes are about 2.8 μs (at 420 nm) and 3.6 μs (at 618 nm). These values are similar to the lifetimes of the Bi^{3+} and Bi^{2+} centers in crystal hosts [6, 9].

Figure 4.8 (a) shows the near-infrared emission spectra of the glass samples when excited by 808 nm LD. The decay curve of the 1340 nm emission for glass sample G5 at room temperature is presented in Fig. 4.8a), and the estimated lifetime is 365 μs. It is interesting that the emission intensity increases from sample G1 to G5, and then decreases from sample G5 to G8. Sample G5 shows the strongest emission intensity.

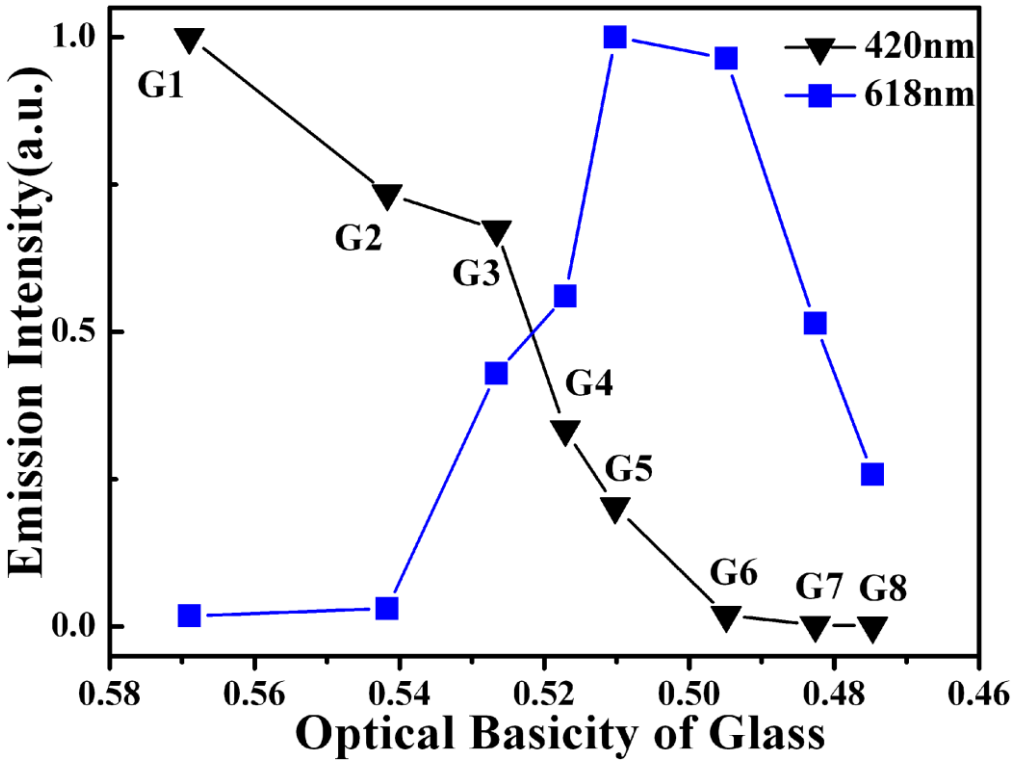

Fig. 4.7 Dependence of the 420 nm and 618 nm emission intensities on optical basicity of the glass samples.

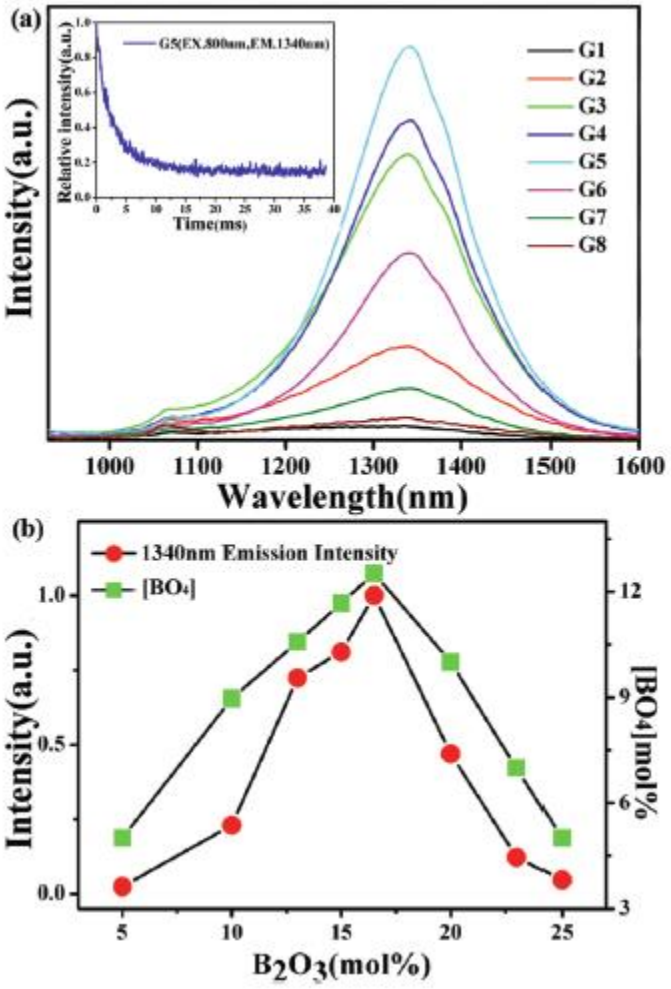

Fig. 4.8 (a) NIR emission spectra of the samples excited at 808 LD. The inset shows NIR fluorescence decay curves of sample G5 (monitoring wavelength is 1340 nm and the corresponding excitation wavelength is 800 nm). (b) Dependence of NIR 1340 nm emission band intensity and $[BO_4]$% content of the related glasses.

It is similar to the red emission from Bi^{2+}. Many reports showed that decrease of the optical basicity of glass would result in the increase of the near-infrared emission intensity for Bi-doped glasses. As aforementioned, Bi^{3+} ions transfer to lower valence bismuth ions with the decrease of the optical basicity of glass. That means that the red emission or near-infrared emission intensity may increase with increasing B_2O_3 concentration. But as shown in Fig. 4.7 and Fig. 4.8, both the intensities of visible emission at 618 nm and near-infrared emission at 1340 nm show a maximum for G5 glass when x=16.5. These phenomena are unusual in Bi doped glasses since usually both the intensities of visible emission at 618 nm and near-infrared emission at 1340 nm increase with decreasing optical basicity of glass.

Boron anomaly features have been reported in various borate glasses [13,14]. Relationship between boron anomaly feature and glass micro-structure in sodium borosilicate glasses have been investigated deeply up to now. The structure of the sodium borosilicate glass is sensitive to the glass composition. The change of boron atom between three- and four-fold coordination states with glass composition causes relevant change in some physical properties which is called boron anomaly. Here by using a comprehensive model presented by Bray et al. [15], which has been successfully applied to describe a number of ^{11}B NMR data, to calculate N_4 (N_4 is the fraction of borons four-coordinated with oxygen) value in our glass samples. The N_4 value obtained from Bray model is given in Table 1. The related concentration of $[BO_4]$ ($[BO_4]\ \% = B_2O_3\ \% \times N_4$) was also given in Table 1. As shown in Fig. 4.8 b, the intensity of NIR emission at 1340 nm shows the same dependence of B_2O_3 concentration with mole percentage of $[BO_4]$. Therefore, we inferred that $[BO_4]$ play an important role for the NIR luminescence center (here we labeled at Bi^{x+}). Because

each [BO_4] unit possesses one minus charge, it cannot connect with each other, and alkali cation or other metal cation is needed to compensate the charge of [BO_4] unit. In the sodium borosilicate glasses, Na^+ and Bi^{x+} may locate near the [BO_4] unit for charge compensation. The valent electrons of Bi are lack of shielding from surrounding crystal fields. Electrostatic interactions could happen between Bi cation and neighboring [BO_4] unit. [BO_4] unit is considered to play an electrontransferring role in the reduction process of $Eu^{3+} \rightarrow Eu^{2+}$ in the nonreducing atmosphere [16]. The three-dimensional network of [BO_4] tetrahedral acts as a shield; it can isolate Eu^{2+} ions from each other and completely or partly surround Eu^{2+} ions and resist the attack of oxygen, therefore Eu^{2+} ions can retain the divalent state in air. Here the existence of [BO_4] unit may have the same effect on Bi. More bismuth with lower valence state will be created with the increase of the number of [BO_4] tetrahedral in the glass samples. Bi^{2+} and Bi^{x+} are more stable existing when these are more [BO_4] tetrahedral in the in the sample.

Although the origination of the NIR luminescence is still controversial and unclear, there have been many conflict evidences as to whether the lower valence Bi or the higher valence Bi contributes to the NIR luminescence [1, 17]. Since both the red emission and the near-infrared emission show the boron anomaly feature so they maybe come from the same active-center, the NIR emission may come from Bi^{2+}. But the fluorescence decay time of the NIR emission is two orders of magnitude longer than that of Bi^{2+}. Therefore, it should be ascribed to another type of active center. According to analysis above, the decrease of optical basicity and increase of the number of [BO_4] unit favor the formation of lower bismuth with lower valence state, therefore the NIR emission may be attributed to low valence state Bi, most probably

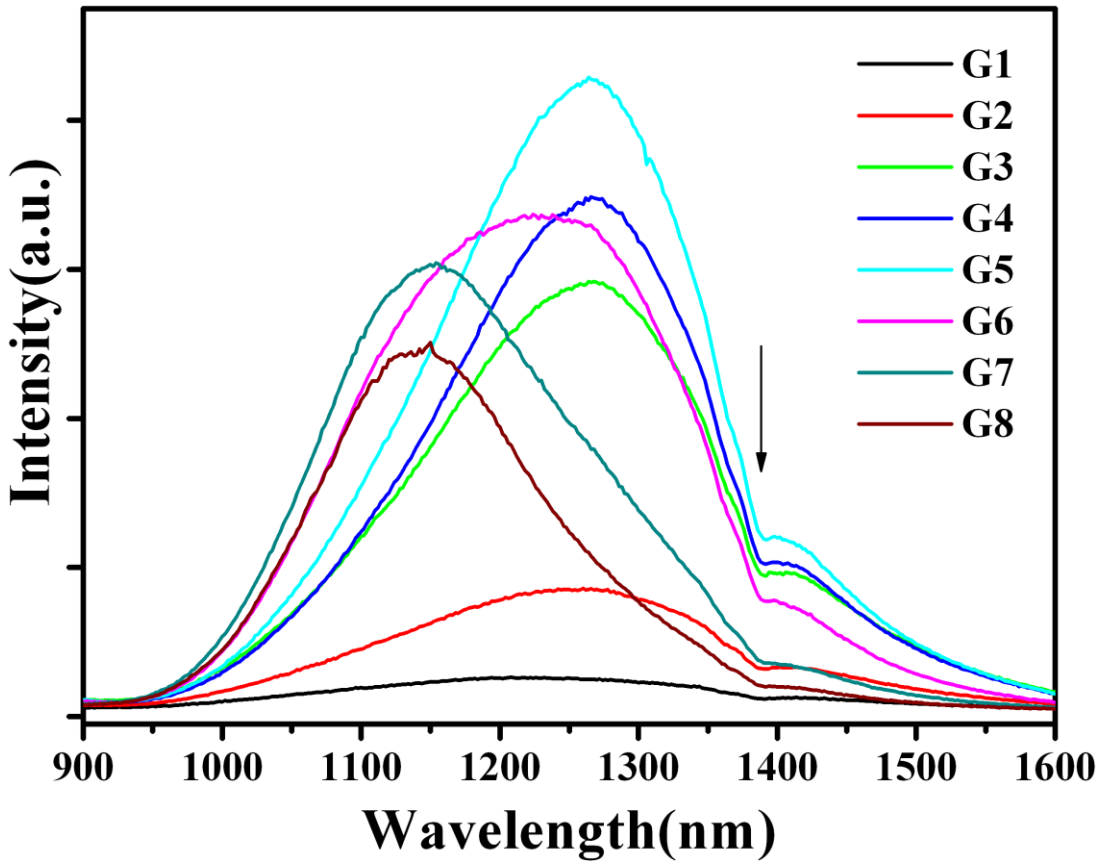

Fig. 4.9 NIR luminescence spectra of the samples excited at 468 nm

Bi^{+} considering the effect of glass matrix and charge compensation, rather than a higher valence state.

Fig. 4.9 shows the NIR emission spectra of the glass samples excited at 468nm. There are two main emission bands at 1154 nm and 1266 nm. The gap in the emission band at wavelengths between 1350 to 1400 nm should be ascribed to absorption of OH^{-} related to spectroscopic measurement system. The results show that the peak position of the broadband NIR emission shifts from 1266 nm to 1154 nm and emission intensity shows the same boron anomaly feather with increasing B_2O_3 concentration from 5 mol% to 25 mol%. The NIR emission band can be deconvoluted into two bands, one is at 1266 nm, and another at 1154 nm, which may be related to Bi^{+} located near $[BO_4]$-Si ($[BO_4]$ unit connected with $[SiO_4]$ units) and $[BO_4]$-B ($[BO_4]$ unit connected with $[BO_3]$ units) glass network, respectively. This phenomenon can also attribute to the structural change of the sodium borosilicate glasses. Furthermore, it suggests that we can obtain broadly tunable NIR emission by adjusting B_2O_3 concentration.

4.4 Demonstration of Optical Amplification in Bi-doped Borosilicate Glass

In this section we measured the single-pass optical amplification in the sample to investigate its potential application in broadband fiber amplifiers. Glass sample of G5 mentioned in the above section is used for the optical amplification experiment.

The measurement of change in optical signals is preceded by mixing seed beam and pump beam from 808 nm LD (inset of Fig. 4.10). Fig. 4.10 shows change in optical signals and its power dependence. An oscilloscope image of the optical signal change at 1340 nm is shown at the top left corner of Fig. 4.10 when the sample is excited with 808 nm LD , the power is 1.35 W. It can be seen that both signals between 3 and 5 ms are zero, so neither spontaneous emission nor leakage of the excitation beam was detected. The phenomena might be ascribed to the optical amplification. The relationship between the change in optical signal and the launched pump power is shown in Fig. 4.10. It can be seen that the change in signal increases with excitation power up to 1.35 W. The power dependence can be fitted to a single linear relation when the pump power is above 0.8 W.

To confirm the observed optical signal change is due to optical amplification, we also investigate the amplified spontaneous emission (ASE) of the sample. Fig. 4.11 shows the ASE spectra of Bi-doped sodium borate silicate glass, the wave length of the signal is 1343 nm. It can be seen that the wave shape of seed beam is not distorted after the pump beam is exerted on the sample, so the Bi-doped glass sample actually realize the optical amplification.

The broad luminescence peaked around 1340 nm pumped by 808 nm LD for

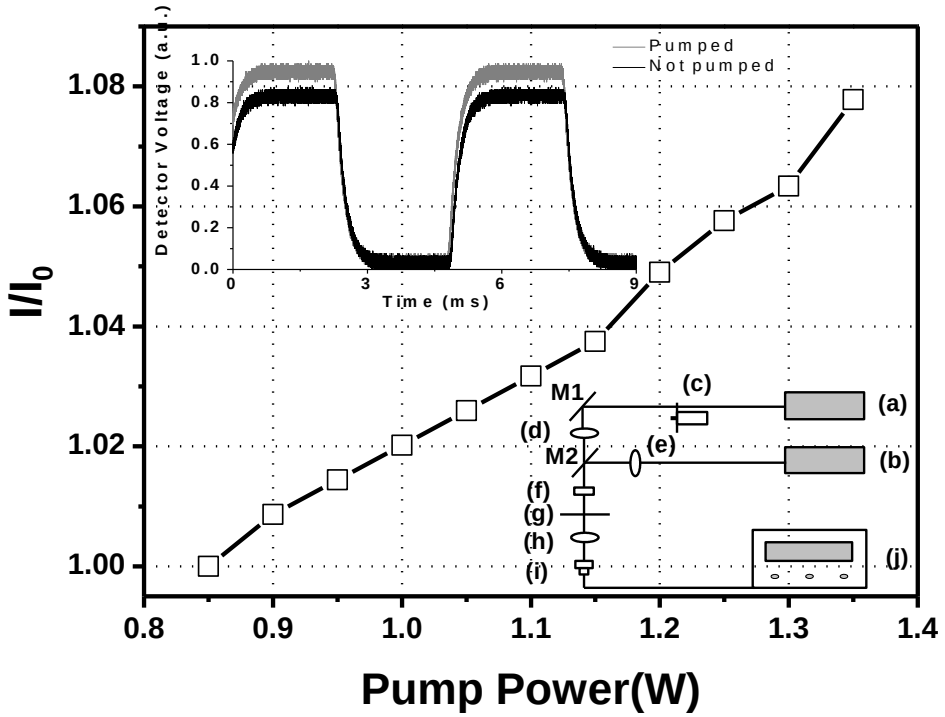

Fig. 4.10 The change in optical signal I / I_0 and the launched pump power. I and I_0 are the signal intensities with and its power dependence with 808 nm excitation displayed by the digital oscilloscope. The bottom right of the inset shows the schematic diagram. (a) 1340 nm tunable laser diode as seed beam, (b) 808 nm laser diode as excitation resource, (c) chopper, (d) lens with 100 mm focal length, (e) lens with 50 mm focal length, (f)sample, (g) filter, (h) lens with 25 mm focal length, (i) InGaAs p-i-n detector, and (j) digital oscilloscope. M1 and M2 are mirrors. The top left corner of the inset shows an oscilloscope image of the optical signal change at 1340 nm under excitation with 808 nm (the power is 1.35 W).

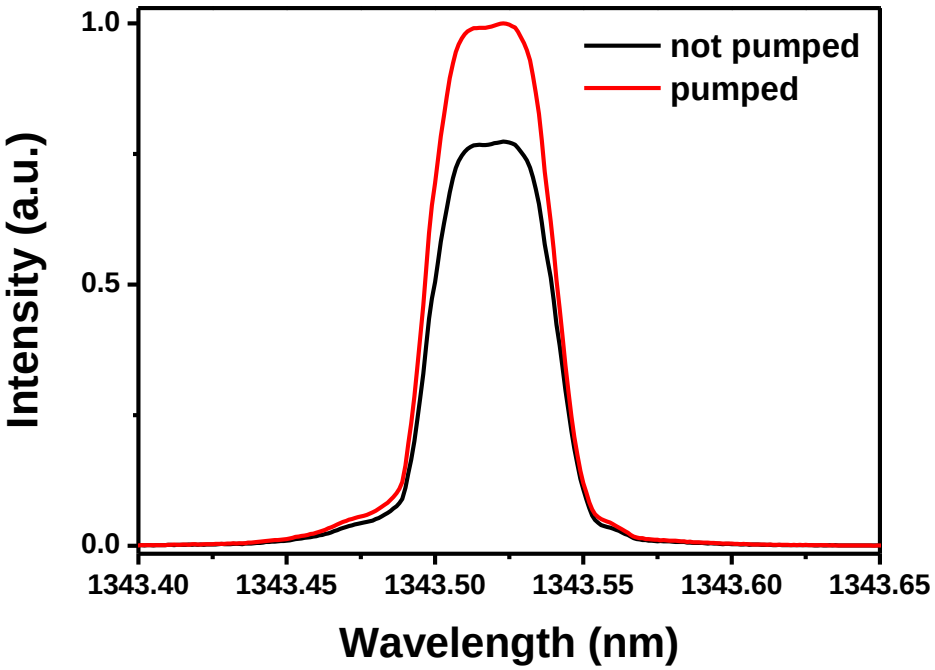

Fig. 4.11 Amplified spontaneous emission spectra of Bi-doped borosilicate glass.

common commercial Bi-doped sodium borate silicate glass has great significance since it lies at the O (1260-1360 nm) and E (1360-1460 nm) band of telecommunication window. It is known that Pr-doped fluoride fiber is used as amplifier in O band at present. However, the production of fluoride fiber is complex and it is difficult to connect to silica fiber and the gain width of Pr-doped fluoride fiber is small. Furthermore, Bi-doped glass is promising to realize the broadband emission covering almost the whole telecommunication window [18]. As the infrared luminescence property of Bi-doped glass is sensitive to host, we can further search a new Bi-doped material with high gain over all telecommunication window, and additionally, more commercial property for industry production.

4.5 Conclusion

In conclusion, we synthesized Bi-doped alkali earth borate glasses in air and weak reduction atmosphere. Calcium borate glasses, strontium and barium borate glasses melted in carbon crucibles exhibit the broadband infrared emission upon the 0.8μm excitation at room temperature. These emissions are likely originates from low valence bismuth in the glasses. Selections of the glass compositions and control of appropriate synthesized atmosphere is necessary to fabricate Bi-doped glasses for realization of fiber broadband optical amplification. We also prepared bismuth-doped borosilicate glasses and their spectral properties were investigated. Boron anomaly features is found for both visible and NIR emissions. The number of [BO_4] plays an important role for the luminescence of bismuth with low valence state. The infrared emission is quite sensitive to glass composition and excitation wavelength. The NIR luminescence originates from the low-valence-state Bi, especially for Bi^+. Finally we demonstrated the optical amplification of Bi-doped borosilicate glass, ASE spectra verifies that the Bi-doped glass realize the optical amplification, which indicates that the Bi-doped borosilicate glass has potential applications in broadband optical fiber amplifiers and tunable lasers.

4.6 References

[1] Y. Fujimoto, and M. Nakatsuka, Jpn. J. App. Phys. **40** (2001) L279.

[2] J. A. Duffy, M. D. Ingram, and S. Fong, PCCP, **2** (2000) 1829.

[3] J. Duffy, J. Non-Cryst. Solids **196** (1996) 45.

[4] V. V. Dvoyrin, V. M. Mashinsky, L. I. Bulatov, I. A. Bufetov, A. V. Shubin, M. A. Melkumov, E. F. Kustov, E. M. Dianov, A. A. Umnikov, V. F. Khopin, M. V. Yashkov, and A. N. Guryanovb, Opt. Lett. **31** (2006) 2966.

[5]S. Zhou, N. Jiang, B. Zhu, H. Yang, S. Ye, G. Lakshminarayana, J. Hao, and J. Qiu, Adv. Funct. Mater. **18** (2008) 1407.

[6] G. Blasse, and A. Bril, J. Chem. Phys. **48** (1968) 217.

[7] M. J. Weber, and R. R. Monchamp, J. Appl. Phys. **44** (1973) 5495.

[8] M. Peng, B. Wu, N. Da, C. Wang, D. Chen, C. Zhu, and J. Qiu, J. Non-Cryst. Solids. **354** (2008) 1221.

[9] M. A. Hamstra, H. F. Folkerts, and G. Blasse, J. Mater. Chem. **4** (1994) 1349.

[10] M. Peng, and L. Wondraczek, Opt. Lett. **34** (2009) 2885.

[11] A.Lebouteiller, and P.Courtine, J. Solid State Chem. **137** (1998) 94.

[12] S.Khonthon, S.Morimoto, Y.Arai, and Y.Ohishi, J. Ceram. Soc. Jpn. **115** (2007) 259.

[13] L. Huang, and J. Kieffer, Physical Review B **74** (2006) 224107.

[14] M. Smedskjaer, J. Mauro, S Sen, J. Deubener, and Y. Yue, J. Chem. Phys. **133** (2010) 154509.

[15]Y. H. Yun, and P.J. Bray, J. Non-Cryst. Solids **27** (1978) 363.

[16] Z. Pei, Q. Zeng, Q. Su, J. Phys. Chem. Solids **61** (2000) 9.

[17] X. Meng, J. Qiu, M. Peng, D. Chen, Q. Zhao, X. Jiang, and C. Zhu, Opt. Express

13 (2005) 1628.

[18] S. Zhou, H. Dong, H. Zeng, G. Feng, H. Yang, B. Zhu, and J. Qiu, App. Phys. Lett. **91** (2007) 061919.

Summary

Inorganic glass has been used as optical material for a longtime due to its isotropy, making large size and high optical homogeneity easier and enabling both high transparency over a wide spectral range from ultraviolet to infrared as well as linear functional properties. The development of modern science and technology requires new applications called “Photonics.” Photonics deals with photon generation and detection as well as stimulated emission, photon frequency conversion, and polarization change. Therefore, inorganic glass still plays an essential role in photonics used as the transmitting and linear functional media for photonics.

The properties of inorganic glass are not only dependent on glass composition but also highly dependent on glass structure. With a femtosecond laser, we can achieve three-dimensional processing inside glass with high accuracy and excellent reproducibility. In this thesis, we researched mainly the modification of the glass structure and observed the resultant variation in optical property. The results are summarized in the following.

In Chapter 1, we reviewed the concept and the mechanism of femtosecond laser processing and introduced the development of a new type of structuring inside glass. In particular, from the evidence of Raman spectra, we observed the compression and densification of sodium germanate glass with femtosecond laser irradiation.

In Chapter 2, we observed an abnormal Raman mapping of an area modified with a femtosecond laser. The intensity of the Raman scattering was highly dependent on the polarization direction of a probe beam, which was never reported in glass materials. We excluded the other possible reasons and deducted that long-range order

could be induced inside transparent glass material without crystallization by using femtosecond laser irradiation. We believed a new state of condensed matter was found, called “ordered glass”. This long-range-ordered glass phase shares some similarities with liquid crystals and polymers. This new phase was never expected from existing glass theory, leading to further consideration about the glass forming process, supercooled liquid behavior, and the exploitation of the micro-structuring method with femtosecond laser irradiation.

In Chapter 3, we used a high-repetition-rate near-infrared femtoseond laser to reduce Eu^{3+} into Eu^{2+} inside silicate glass. Although there were already reports on using a femtosecond laser to reduce Eu ions, the photo-reduction process of Eu depends highly on the glass host, so we could only achieve a reduction in fluoride or borate glass. To break through this limitation, we found that we could possibly use a different photo-reduction mechanism that involved laser-induced-crystallization for the reduction. In this work, we showed that this kind of idea is potentially valuable for the application of Eu-doped glass.

In Chapter 4, we synthesized Bi-doped borate and borosilicate glasses and investigated how the glass composition and structure affected the luminescence property of bismuth ions in a glass host. The infrared emission was quite sensitive to glass composition, structure, and excitation wavelength. The NIR luminescence should originate from the Bi^{+}. Finally, we demonstrated the optical amplification of Bi-doped borosilicate glass, indicating that Bi-doped borosilicate glass has potential applications in broadband optical fiber amplifiers and tunable lasers.

List of Publications

Chapter 1

"Confocal Raman imaging of femtosecond laser induced microstructures in germinate glasses"

Yin Liu, Masahiro Shimizu, Xi Wang, Bin Zhu, Masaaki Sakakura, Yasuhiko Shimotsuma, Jianrong Qiu, Kiyotaka Miura, Kazuyuki Hirao.

Chemical Physics Letters, 477, 122-125 (2009)

"Fabrication and characterization of silicon anti-reflection structures for infrared rays using a femto-second laser"

Hiroshi Imamoto, Shigo Kanehira, Xi Wang, Keisuke Kametani, Masaaki Sakakura, Yasuhiko Shimotsuma, Kiyotaka Miura, Kazuyuki Hirao

Optics Letters, 36, 1176-1178 (2011)

"Selective metallization of Ag_2O-doped silicate glass by femtosecond laser direct writing"

Nan Wu, Xi Wang, Masatoshi Ohnishi, Kazuyuki Hirao, Kiyotaka Miura, Masayuki Nishi, Yasuhiko Shimotsuma.

Journal of the Ceramic Society of Japan (in submission)

"Femtosecond laser induced nano periodic structure formation on titanium thin film"

Nan Wu, Xi Wang, Kazuyuki Hirao, Kiyotaka Miura, Masayuki Nishi, Yasuhiko Shimotsuma

Journal of Non-Crystalline Solids (in submission)

Chapter 2

"Molecular radial orientation arrangement by femtosecond laser irradiation inside sodium germanate glass"

Xi Wang, Masaaki Sakakura, Kiyotaka Miura, Kazuyuki Hirao

Proceedings of the 3rd International Congress on Ceramics (accepted)

"Modification of long range order in germanate glass by ultra fast laser"

Xi Wang, Masaaki Sakakura, Yin Liu, Jianrong Qiu, Yasuhiko Shimotsuma, Kazuyuki Hirao, and Kiyotaka Miura

Chemical Physics Letters (accepted)

Chapter 3

"Space selective reduction of europium ions via SrF_2 crystals induced by high repetition rate femtosecond laser"

Xi Wang, Nan Wu, Masahiro Shimizu, Masaaki Sakakura, Yasuhiko Shimotsuma, Kiyotaka Miura, Shifeng Zhou, Jianrong Qiu, and Kazuyuki Hirao

Journal of the Ceramic Society of Japan (in submisssion)

Chapter 4

"Infrared broadbandemission of bismuth-doped RO-B2O3 (R = Ca, Sr, Ba) glass"

Xi Wang, Shifeng Zhou, Jiaxing Bao, Jianrong Qiu

Journal of Wuhan University of Technology Materials Science, 79, 841-843 (2007)

"Abnormal luminescence behavior in Bi-doped borosilicate glasses"

Miaojia Guan, Xi Wang, Yixi Zhuang, Geng Lin, Junhua Xie, Morten Mattrup Smedskjr, Jianrong Qiu

Journal of the Electrochemical Society, 158, G151-G154 (2011)

"Luminescence properties of nickel and bismuth co-doped barium aluminosilicate glasses"

Jiaxing Bao, Shifeng Zhou, Gaofeng Feng, Xi Wang, Xvsheng Qiao, Jianrong Qiu

Journal of Alloys and Conpounds, 456, 239-242 (2008)

"Transparent Ni^{2+}-doped lithium aluminosilicate glass-ceramics with broadband infrared luminescence"

Gaofeng Feng, Shifeng Zhou, Jiaxing Bao, Xi Wang, Shiqing Xu, Jianrong Qiu

Journal of Alloys and Conpounds, 457, 506-509 (2008)

Acknowledgements

The present thesis has been carried out at Graduate School of Engineering, Kyoto University under the supervision of Professor Kazuyuki Hirao and Professor Kiyotaka Miura.

The author wishes to express his sincere gratitude to Prof. Hirao and Prof. Miura, who granted me the chance to study in Kyoto University with financial support. Their wise guide and valuable suggestions enlightened me constantly throughout the whole period of doctor course study.

I am also deeply indebted to Dr. Masaaki Sakakura, Dr. Yasuhiko Shimotsuma and Mr. Masahiro Shimizu. Their great help and instructive discussion made me thoroughly understand the function of the equipments during the experiments as well as the mechanism of femtosecond laser processing.

Heartily thanks to Prof. Jianrong Qiu, Dr. Shifeng Zhou at Zhejiang University, for their helpful support and profitable suggestions.

Grateful acknowledgment is made to Dr. Masayuki Nishi and Mr. Nan Wu, who given me a lot of advice about the experiments and life in Japan.

Finally, the author is deeply grateful to his parents for their understanding, supports, and encouragements.

Kyoto, 2011

Xi Wang